	Name(s)	**Date**
Prepared by:	E. Del Monte R. Campana S. Diebold M. Orlandini E. Perinati A. Rachevski G. Zampa N. Zampa	2013-09-26
Agreed by:	S. Brandt S. Zane	
Authorized by:	M. Feroci	

ESA-DRL/SE-12

DISTRIBUTION

Issue	Distribution
1.0	To ESA (PRR submission)

DOCUMENT CHANGE RECORD

Issue	Date	Changed Section	Description of Change
1.0	2013-09-25	All	Finalized for PRR submission

APPLICABLE DOCUMENTS

Applicable Documents [ADs] are applicable in their entirety or to the extent called up in individual sections of this document and are listed below as dated or undated references.

AD#	Document ID	Title
[AD-1]	SRE-SA/LOFT/2011-001	LOFT Science Requirements Document (Issue 2, Revision 2, dated 2013-09-11)
[AD-2]	LOFT-IAPS-PLC-MD-0002	LOFT Preliminary Radiation Model
[AD-3]	LOFT/SRE-F/2012.095	LOFT Experiment Interface Document – Part A, EID-A (Issue 1, Revision 1, dated 2013-08-30)
[AD-4]	LOFT-IAPS-PLC-RS-002	LOFT ASIC requirements specifications
[AD-5]	SRE-F/2012-076/RQ/MA	LOFT Mission Requirements Document (Issue 3, Revision 7, dated 2013-09-11)

REFERENCE DOCUMENTS

Reference documents [RDs] contain supplementary information about the mission and related issues. They do not contain directly applicable requirements. However, clauses of reference documents may have been copied directly, or modified, into Applicable Documents, through which these clauses are then applicable.

RD#	Document ID	Title
[RD-1]	LOFT-IAPS-PLC-TN-0005	LOFT System Notes Silicon Drift Detectors Performances
[RD-2]	SRE-PA/2011.088	LOFT Payload Definition Document
[RD-3]	LOFT-IAPS-LAD-TN-0002	LAD Energy Resolution Breakdown
[RD-4]	LOFT-IAPS-PLC-TN-0004	LOFT System Notes Silicon Drift Detectors: current status and development plan
[RD-5]	LOFT-IAPS-PLC-TN-0003	Radiation damage of the LOFT SDDs and its effects on the energy resolution
[RD-6]	Segneri et al. 2009, IEEE Trans. Nucl. Sci., 56, 3734	Measurement of the Current Related Damage Rate at -50 °C and Consequences on Macropixel Detector Operation in Space Experiments

[RD-7]	Vasilescu & Lindstroem, **http://hepweb03.phys.sinica.edu.tw/opto/Irradiation/Documents/NIEL_scaling/gunnar.htm**	Displacement damage in silicon, on-line compilation
[RD-8]	ECSS-E-ST-10-04C	Space engineering, Space environment (Issue 2, dated 2008-11-15)
[RD-9]	Kruglanski et al. 2010, 38th COSPAR Scientific Assembly, Symposium PSW, PSW1-0024-10	Space Environment Information System (SPENVIS)
[RD-10]	Ginet et al. 2013, Space Sci. Rev., in press (available on ADS)	AE9, AP9 and SPM: New Models for Specifying the Trapped Energetic Particle and Space Plasma Environment
[RD-11]	Frontera et al. 1997, ApJ, A&ASS, 122, 357-369	The high energy instrument PDS on-board the BeppoSAX X-ray astronomy satellite
[RD-12]	ESA-LOFT-TN-0007	Application of AP8 and AP9 radiation-belt models to LOFT (Issue 1, dated 2013-08-26)
[RD-13]	INFN/TC-02/09	Irradiation tests of the ALICE Silicon Drift Detector at the LINAC of the "Elettra" Synchrotron in Trieste (dated 2002-04-10)
[RD-14]	Petrov et al. 2009, Adv. Sp. Res., 43, 654	Creation of model of quasi-trapped proton fluxes below Earth's radiation belt
[RD-15]	LOFT-INFN-PLC-TN-0002	Evaluation of the LOFT LAD and WFM Silicon Drift Detector damage by soft protons
[RD-16]	Armstrong & Colborn 200, NASA / CR--2000-210072	Evaluation of Trapped Radiation Model Uncertainties for Spacecraft Design
[RD-17]	Armstrong & Colborn 2000, Report N. SAIC-TN-99030	Trapped Radiation Model Uncertainties: Model - Data and Model- Model Comparisons
[RD-18]	LOFT-IAPS-PLC-TN-0002	LOFT Effective exposure for soft protons
[RD-19]	Moll et al. 2002, NIM B, 186, 100	"Relation between microscopic defects and macroscopic changes in silicon detector properties after hadron irradiation"
[RD-20]	Bechevet et al. 2002, NIM A, 479, 487	"Results of irradiation tests on standard planar silicon detectors with 7-10 MeV protons"
[RD-21]	LOFT-IAPS-PLC-TN-0001	Radiation Damage measurements of the ALICE-type SDD
[RD-22]	LOFT-IAPS-PLC-TN-0007	Measurement of the Radiation Damage from soft protons on the Silicon Drift Detectors
[RD-23]	Diebold et al. 2013, NIM A, 721, 65	A setup for soft proton irradiation of X-ray detectors for future astronomical space missions
[RD-24]	Zampa et al. 2001, NIM A, 633, 15	Room-temperature spectroscopic performance of a very-large area silicon drift detector
[RD-25]	Ohsugi et al. 1988, NIM A, 265, 105	Radiation damage in silicon microstrip detectors
[RD-26]	Meidinger 2000, NIM A, 439, 319	Particle and X-ray damage in pn-CCDs

[RD-27]	Campana et al. 2011, NIM A, 633, 22	Imaging performance of a large-area Silicon Drift Detector for X-ray astronomy
[RD-28]	H. Spieler, Oxford University Press (2005)	Semiconductor Detector Systems
[RD-29]	C. Jacoboni et al. 1977, Solid-State Electronics, 20, 77	A review of some charge transport properties of silicon
[RD-30]	Kramberger et al. 2002, NIM A, 481, 297	Effective trapping time of electrons and holes in different silicon materials irradiated with neutrons, protons and pions
[RD-31]	Kramberger et al. 2007, NIM A, 571, 608	Annealing studies of effective trapping times in silicon detectors
[RD-32]	LOFT-IAPS-PLC-TN-0008	Measurement of the variation of the Charge Collection Efficiency for the LOFT Silicon Drift Detectors
[RD-33]	JS-20-12	LOFT Environmental Specification (Issue 1.0, dated 2012-09-04)
[RD-34]	MASTER 2005 model	MASTER 2005 model (http://www.master-model.de/)
[RD-35]	Grün et al. 1985, Icarus, 62, 244	Collisional balance of the meteoritic complex.
[RD-36]	E.A. Taylor et al. 1999, Int. Jour. Imp. Eng., 23, 895	Hydrocode Modelling of Hypervelocity Impact on Brittle Materials: Depth of Penetration and Conchoidal Diameter
[RD-37]	NASA/TM–2009–214785	Handbook for Designing MMOD Protection
[RD-38]	Carey et al., Lunar and Planetary Science 1985, XVI, 111	Capture Cells: Decoding the Impacting Projectile Parameters
[RD-39]	Carpenter et al. 2005, JGR, 110, E05013	Dust detection in the ISS environment using filmed microchannel plates
[RD-40]	LOFT-IAPS-PLC-TN-0006	Measurement of the effects of debris impacts on the LOFT Silicon Drift Detectors
[RD-41]	M. Levinshtein (ed.), J. Kostamovaara(ed.), S. Vainshtein (ed.), World Scientific Publishing Company (2005)	Breakdown Phenomena In Semiconductors And Semiconductor Devices
[RD-42]	Campana et al. 2013, Exp. Ast., in press	Background simulations for the Large Area Detector onboard LOFT (http://link.springer.com/10.1007/s10686-013-9341-6)
[RD-43]	Sawyer & Vette 1976, NSSDC/WDC-A-R&S 76-06 Natl. Space Sci. Data Center	AP8 Trapped Proton Environment For Solar Maximum and Solar Minimum
[RD-44]	Fürst et al. 2009, Earth and Planetary Science Letters, 281, 125	Temporal variations of strength and location of the South Atlantic Anomaly as measured by *RXTE*
[RD-45]	A. Mohammadzadeh et al.	The ESA Standard Radiation Environment

	2003, IEEE Trans. Nucl. Scie. 50, 2272	Monitor program first results from PROBA-I and INTEGRAL
[RD-46]	J. F. Ziegler, J. P. Biersack, M. D. Ziegler 2012, Lulu Press Co.	SRIM - The Stopping and Range of Ions in Matter (www.srim.org/)
[RD-47]	S.R. Messenger, et al. 1999, IEEE Trans. Nucl. Sci., 46, 1595	Nonionizing Energy Loss (NIEL) for Heavy Ions
[RD-48]	C. Claeys and E. Simoen 2002, Springer	Radiation Effects in Advanced Semiconductor Materials and Devices
[RD-49]	T. R. Oldham 1999, World Scientific	Ionizing Radiation Effects in MOS Oxides

ABBREVIATIONS AND ACRONYSMS

AD	Applicable Document
AIT	Assembly, Integration and Test
AIV	Assembly, Integration and Verification
ASIC	Application Specific Integrated Circuit
BB	Bread-Board
CP	Capillary Plate
CCE	Charge Collection Efficiency
DHU	Data Handling Unit
DP	Detector Panel
EM	Engineering Model
EMC	Electro-Magnetic Compatibility
ENC	Equivalent Noise Charge
EoL	End of Life
EQM	Engineering Qualification Model
ESA	European Space Agency
FEE	Front End Electronics
FoV	Field of View
FS	Flight Spare
FWHM	Full Width at Half Maximum
GSE	Ground Support Equipment
ICDR	Instrument Critical Design Review
LAD	Large Area Detector
LEO	Low Earth Orbit
LLI	Long Lead Item
LOFT	Large Observatory For x-ray Timing
MAIT	Manufacture, Assembly, Integration and Test
MBEE	Module Back End Electronics
MLI	Multi Layer Insulator
MPO	Micro-Pore Optics
MSSL-UCL	Mullard Space Science Laboratory – University College London
NCR	Non-Conformance Report
PBEE	Panel Back-End Electronics
PDR	Preliminary Design Review
PFM	Proto-Flight Model
PSU	Power Supply Unit
RFD	Request For Deviation
RMS	Root Mean Square
SAA	South Atlantic Anomaly
SDD	Silicon Drift Detector
STM	Structural Thermal Model
TID	Total Ionising Dose
TRB	Test Review Board
TRL	Technology Readiness Level

TRR	Test Readiness Review
WFM	Wide Field Monitor

TABLE OF CONTENTS

1 INTRODUCTION

1.1 Scope

This document contains the modelling of the radiation environment of LOFT and its effects on the scientific requirements of the instrumentation. The structure of the document is as follows: Sec. 2 contains the list of scientific requirements for the LAD and WFM. In Sec. 3 we show how these requirements are translated into corresponding requirements on the electronic noise and leakage current of the SDDs, for the LAD and WFM. In Sec. 4 we describe the models and approximations that are used for the radiative environment of LOFT. In particular, we discuss the verification of the AP8 and AP9 models with satellite data in representative orbits. In Sec. 5 we list the shielding materials for the SDDs of the LAD and WFM and in Sec. 6 we discuss the formulas that we used to estimate the radiation damage. The expected radiation damage for LOFT and its impact on the leakage current is shown in Sec. 7. In Sec. 8 we report about the experimental measurements of the radiation damage, performed through several irradiations in different conditions. We show in Sec. 9 how the increment in leakage current produced by the radiation damage is reduced by decreasing the operative temperature of the SDDs, and we provide the operative temperature of the LAD and WFM in orbit. In Sec. 10 we discuss the effect of the damage annealing. In addition to the increase of the leakage current, we studied the variation of the charge collection efficiency produced by the radiation damage, and we measured it in a dedicated campaign, as reported in Sec. 11. Sec. 12 is devoted to the estimation of the effects produced by the impact of micrometeoroids and orbital debris, and the measurement of the effect of the impacts on the SDDs in a dedicated campaign. Finally, in Sec. 13 we draw our conclusions.

The LOFT particle environment relevant for the estimation of the instrument background of the LAD is not included in the present document and is discussed in [RD-42].

2 REQUIREMENTS ON THE NOISE OF THE LAD AND WFM

The requirements on the noise of the LAD and WFM are listed and justified in [AD-1]. In the following, we separately recall for the two instruments the values of the requirements and their justification. The requirements are given for the instrumentation at End of Life (EoL), considered as 4.25 years, i. e. 0.25 years of commissioning for the payload and 4 years of nominal science operation phase [AD-3].

2.1 Requirements on the spectral resolution of the LAD

The requirements on the spectral resolution of the LAD are listed in Table 1 as reported in [AD-1] and are given at an energy of 6 keV and at EoL.

Table 1: Summary of the requirements on the LAD spectral resolution.

Nominal spectral resolution	**Value (ΔE FWHM)**	**ID**	**Condition**	**Level**
Definition	Full Width at Half Maximum (FWHM) of a Gaussian distribution			

	response to a monoenergetic stimulus of the detector, under nominal operating conditions			
Requirement	< 260 eV @ 6 keV	SCI-LAD-R-08	for 60% of the events which are read-out by more than a single anode. See SCI-LAD-R-09 for the specification of the single anode	2a
	Justification: End-of-mission spectral resolution integrated over the full detector but after channel to channel corrections (e.g. gain); Together with the single anode events this resolution allows for gravitationally broadened Fe Kα line-width studies, removal of narrow lines and edges, line/edge studies in PRE type I X-ray bursts. [GOAL SFG2, SFG4, SFG5]. This number includes all not-correctable contributions to the spectral resolution. The available margin on top of the Fano limit of Si will be distributed over different components (calibration, sensor uniformity, gain knowledge etc).			
Requirement	< 200 eV @ 6 keV (40 % of selected events)	SCI-LAD-R-09	2 – 10 keV	2b
	Justification: For bright AGN (> 1 mCrab) and black hole X-ray binaries selection of the single events will improve all science objectives given in SFG4 and SFG5. Selected events are only those that correspond to the read-out of a single anode (explaining the 40% of the selected events).			
Degraded spectral resolution	**Value (ΔE FWHM)**	**ID**	**Condition**	**Level**
Definition	FWHM of a Gaussian distribution response to a monoenergetic stimulus of the detector, under degraded thermal operating conditions.			
Requirement	< 400 eV @ 6 keV	SCI-LAD-R-22	When nominal Solar Aspect Angle (SAA) cannot be maintained, and an increased SAA is adopted to meet sky visibility constraints. Field of regard to be achieved 50%	2b

			(required) 75% (goal).	
	Justification: Not all science goals require optimal energy resolution. In order to avoid unnecessary limitations to the accessible sky at any time, a 50% worse than optimal resolution is acceptable over an extended sky region and this allows the Solar Aspect Angle and thermal constraints to be relaxed.			

2.2 Requirements on the channel noise of the WFM

The requirement on the channel noise of the WFM is derived from the imaging capabilities of the instrument in [AD-4] (W-ASIC-PERF-R-027). From [AD-4], the requirement is an ENC < 13 e- RMS at End of Life per anode with a pitch of 145 μm, as shown in Table 2.

Table 2: Summary of the requirements on the WFM ENC noise from [AD-4].

Identifier	Requirement	Notes
W-ASIC-PERF-R-027	When connected to a SDD detector with C_{det} < 90 fF, C_{stray} < 150 fF and I_{leak} < 3 pA each ASIC channel shall provide an Equivalent Noise Charge (ENC) ≤ 13 e^- r.m.s.	**Note:** As described in the LOFT WFM Preliminary Performance Document, the WFM imaging performance requirements will be met with a single channel ENC ≤ 13 e^- r.m.s. Such a channel noise will also guarantee that the energy resolution will be ≤ 300 eV FWHM, meeting the goal requirement on the WFM energy resolution.

3 REQUIREMENTS ON THE LEAKAGE CURRENT OF THE LAD AND WFM

The energy resolution of the LAD (in Table 1) and the channel noise of the WFM (in Table 2) defined above are affected by various sources of noise and systematics, from the detector and the read-out ASIC.
A discussion of the different contributions affecting the energy resolution of the LAD is reported in [RD-1] and [RD-3. The breakdown of the contributions which affect the energy resolution of the SDDs is reported in [RD-3].
Here we briefly recall that, as listed in [RD-3], the reconstruction of the energy of an incoming photon depends on the following parameters:

1. Fano noise of the detector (~118 eV at 6 keV);
2. Electronic noise of the detector (the requirements are 13 e- RMS for the WFM and 17 e- RMS for the LAD;
3. Charge reconstruction (number of anodes, common mode noise subtraction);
4. ADC quantization noise.

Moreover, for both the LAD and WFM, the integration of signals from a large number of channels gives rise to other sources of uncertainty:

5. Gain spread,
6. Offset spread.

In the following we will concentrate on the electronic noise of the detector and, in particular, we will study the contribution from the leakage current to this noise component. In fact, since the anode capacitance of the SDDs is very small, ~80 fF for the WFM and ~350 fF for the LAD, the main source of noise for these detectors is represented by the bulk leakage current measured in the volume corresponding to the drift channel (as discussed in [RD-1] and [RD-3]).

3.1 Calculation of the electronic noise of the SDDs

The electronic noise of the SDD is composed of three terms: parallel noise (depending on the leakage current), series noise (depending on the anode capacitance/transistor) and flicker noise (1/f component), as explained in [RD-3].
In general, the electronic noise for a single channel is given by the following formula (see [RD-3] for more information):

$$\sigma_{ENC}^2 = i_n^2 T_{sh} F_i + \frac{C^2 e_n^2 F_V}{T_{sh}} + C^2 A_f F_{fv} \quad (1)$$

where:

- F_i (parallel), F_V (series) and F_{fv} (flicker, 1/f) are numerical coefficients that depend only on the particular type of shaper used (CR-RC^n, semi-gaussian, etc);

- i_n^2 is the power spectral density of the parallel (current) noise, in particular of the leakage current (and therefore is temperature-dependent);

- e_n^2 is the power spectral density of series (voltage) noise, mainly due to the first transistor;

- A_f is the power spectral density for the 1/f noise;

- C is the total input capacitance;

- T_{sh} is the shaper time constant.

In the above formula the noise components are given as RMS values equivalent to a charge, ENC, usually quoted in electrons (e-). In the following calculations we assume a CR-RC^2 shaper, which has a lower noise than a CR-RC shaper.

3.2 Requirements on the (maximum total) leakage current for the LAD

We list in Table 3 the maximum acceptable values of the electronic noise σ_{ENC} in Eq. (1) in order to fulfil the requirements on the energy resolution of the LAD (specified in Table 1).

Table 3: Maximum values of σ_{ENC} in Eq. (1) for the LAD, dictated by the requirements on the spectral resolution summarised in Table 1.

Requirement	**Value (ΔE FWHM)**	**ID**	**σ_{ENC} [e-]**
Nominal spectral resolution	< 260 eV @ 6 keV (60 % of the events)	SCI-LAD-R-08	17.0
Nominal spectral resolution	< 200 eV @ 6 keV (40 % of selected events)	SCI-LAD-R-09	17.0
Degraded spectral resolution	< 400 eV @ 6 keV	SCI-LAD-R-22	30.4

Applying Eq. (1) with the values of σ_{ENC} given in Table 3, we can derive the maximum acceptable values of the leakage current in order to fulfil the requirements, as listed in Table 4. We stress here that not only the leakage current, but also other parameters in Eq. (1) impacting on the energy resolution (e. g. the hole mobility and the noise in series) have a thermal variation, thus in Table 4 we specify the temperature at which the values of the maximum leakage current are estimated. These temperature values ($T_{fluence*20}$) are estimated applying the margin of a factor of 20 on the proton fluence (see Table 18). We also show in Table 4 the value of the shaping time which, at that temperature, gives the minimum of the electronic noise for the specified value of the leakage current. All the other parameters affecting the electronic noise have a weak dependence on the temperature, in fact on a total span of 42 °C the values of the maximum leakage current show a variation of only 29 %.

Table 4: Requirement on the maximum total leakage current for the LAD in order to fulfil the requirement on the nominal energy resolution (SCI-LAD-R-09). The current values are computed at a specific temperature with a specified shaping time. The temperatures $T_{fluence*20}$ are estimated applying the factor of 20 on the proton fluence.

Altitude	Inclination	Maximum leakage current		$T_{fluence*20}$	Shaping time
[km]	[°]	[pA/cm^3]	[pA/anode]	[°C]	[μs]
550	0	305.0	4.7	-10*	4.2
550	2.5	305.0	4.7	-10	4.2
550	5	360.9	5.5	-35	3.5
600	0	337.2	5.2	-34	3.7
600	2.5	375.5	5.7	-43	3.4
600	5	394.7	6.0	-52	3.2

* the orbit at 550 km, 0.0° is below the validity range for SPENVIS. Conservatively, we adopt for this orbit the same temperature values as in 550 km, 2.5°.

3.3 Requirements on the (maximum total) leakage current for the WFM

The maximum value of the single channel ENC to fulfil the imaging performance requirements of the WFM (W-ASIC-PERF-R-027) is listed in Table 2: $\sigma_{ENC} \leq 13.0$ e-RMS. The same approach used above for the LAD applies to the WFM and the maximum value of the leakage current acceptable for the SDDs in order to fulfil the requirement on the energy resolution is listed in

Table 5. Similarly to the LAD, the maximum value of the leakage current is calculated for a specific temperature and for the constant of the shaper time that minimises the electronic noise. In the case of the WFM, over a total span of 39 °C the variation of the maximum current values is 25 %. Similarly to the LAD, the temperature values $T_{fluence*20}$ are estimated applying the margin of a factor of 20 on the proton fluence (see Table 20).

Table 5: Requirement on the maximum leakage current for the WFM in order to fulfil the requirement on the electronic noise . The current values are computed at a specific temperature with a given peaking time. The temperatures $T_{fluence*20}$ are estimated applying the margin of a factor of 20 on the proton fluence.

Altitude	Inclination	Maximum leakage current		$T_{fluence*20}$	Peaking time
[km]	[°]	[pA/cm^3]	[pA/anode]	[°C]	[μs]
550	0	927.2	2.1	-3*	3.5
550	2.5	927.2	2.1	-3	3.5
550	5	1025.0	2.3	-23	3.0
600	0	1080.6	2.5	-22	3.5
600	2.5	1080.0	2.5	-31	3.0
600	5	1158.4	2.6	-42	2.5

* the orbit at 550 km, 0.0° is below the validity range for SPENVIS. Conservatively, we adopt for this orbit the same temperature values as in 550 km, 2.5°.

3.4 Requirements on the intrinsic leakage current of the SDDs

The requirements on the maximum bulk leakage current listed in Table 4 (LAD) and

Table 5 (WFM) are the sum of two contributions: the intrinsic leakage current (before launch) and the current increase produced by the radiation damage (at End of Life).
We assume as requirement on the intrinsic leakage current a value corresponding to 3.5 times the current of the SDDs with the substrate employed by Canberra for the ALICE-D4 detectors (see [RD-2] and [RD-4]). This value is 3048.5 pA/cm^3 at 20 °C, and corresponds at the same temperature to 46.6 pA/anode for the LAD and 7.0 pA/anode for the WFM.

4 ASSUMED RADIATION ENVIRONMENT FOR LOFT

4.1 The LOFT orbit

From [AD-1] the baseline orbit for LOFT is an Equatorial Low Earth Orbit (LEO) and the requirements are an altitude < 600 km (SCI-SYS-R-11) and an inclination < 5° (SCI-SYS-R-12). The goal on the parameters of the orbit is an altitude < 550 km (SCI-SYS-G-11) and an inclination < 2° (SCI-SYS-G-12).
The orbit selected for LOFT by both industrial studies has an altitude of 550 km and an inclination of 0° (see also [RD-12]).

4.2 The AP8 model for trapped protons

At the Equatorial LEOs for LOFT the Earth magnetic field efficiently shields the satellite from protons of energy below ~10 GeV and ions below ~1 GeV/nucleon, as shown for example in Figure 1, produced with the CREME96 web-based software (https://creme.isde.vanderbilt.edu/). This shielding effect protects LOFT from Cosmic Rays and charged particles such as protons and ions emitted during Solar flares. Cosmic rays and Solar protons are thus negligible at the LOFT orbit and the radiation environment is represented by protons trapped in the Earth radiation belts, mainly concentrated inside the South Atlantic Anomaly (SAA). This component is commonly referred to as the "trapped" proton component.

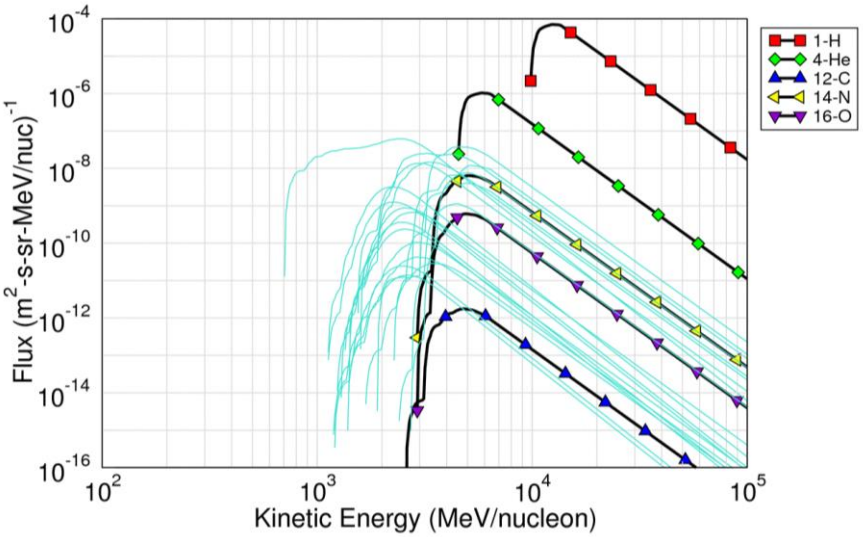

Figure 1: Flux of protons and ions estimated with CREME96 for an orbit at 550 km altitude and 2.5° inclination during the large solar flare of 20 October 1989.

Following the ESA recommendation in [RD-8], in order to estimate the flux of trapped protons for the LOFT environment we used the AP8 model for Solar Minimum conditions (AP8MIN), which represents a worst case for the environment since the proton flux is higher than in Solar Maximum conditions (AP8MAX). For example, for an orbit at 600 km altitude and 5° inclination, the integral flux of AP8MIN at 1 MeV is ~7 times higher than AP8MAX, and ~6 times higher at 10 MeV.
The estimation of the flux of trapped protons is performed using the web-based Space Environment Information System (SPENVIS) software, developed in collaboration with ESA (see [RD-9] and http://www.spenvis.oma.be/intro.php for more information).

SPENVIS includes both AP8MIN and AP8MAX models and provides the omnidirectional flux of protons, i. e. on a solid angle of 4π sr. The list of the software packages run inside SPENVIS to simulate the radiation environment of LOFT is in [AD-2].
Since the LAD and WFM will not have a fixed orientation but will be pointed in various directions following the LOFT pointing plan, the different spacecraft orientations are expected to wash out the anisotropy in the proton incoming directions. For this reason we neglect the directionality in the trapped proton flux and assume the omnidirectional flux of AP8 for radiation-effect calculations. In our estimations we select AP8MIN as a worst case and we assume for LOFT a duration of 4.25 years (starting on 1 Jan 2022) and orbits with altitude between 550 km and 600 km and inclination between 0° and 5°, as specified in [AD-1] and [AD-5]. The next Solar minimum will occur roughly in 2019. Should LOFT be launched on 2022, it will be operative during the rise of the Solar cycle from the next minimum (~2019) to the next maximum (~2026). For this reason, assuming AP8MIN represents a worst case in the estimation of the trapped proton flux.
The omnidirectional integral and differential flux of protons from the AP8MIN model estimated at the LOFT orbit with 550 km altitude and 2.5° inclination for 4.25 years starting on 1 Jan 2022 is shown in Figure 2. This flux is about three orders of magnitude higher than the maximum value of the proton flux during a solar flare (red squares in Figure 1). For this reason we can neglect the contribution of Cosmic Rays and Solar flares.

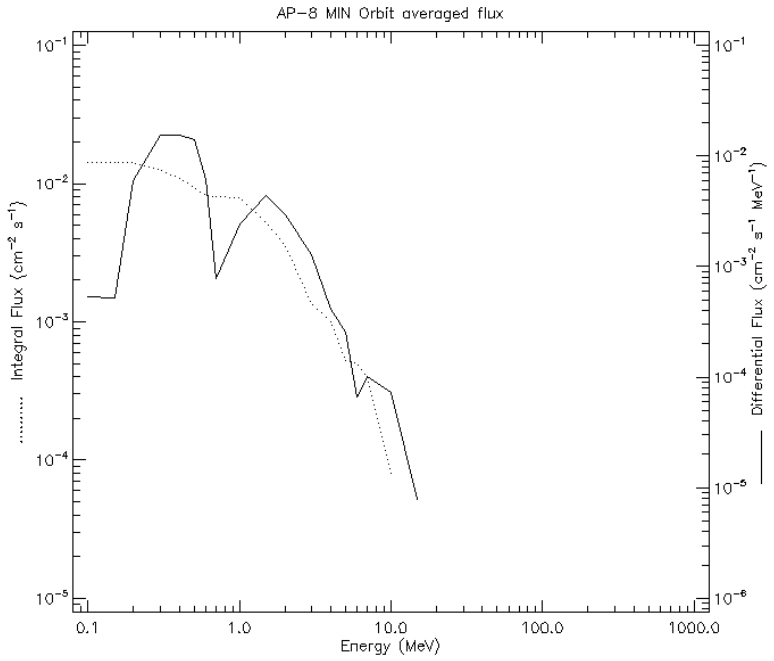

Figure 2: Omnidirectional integral and differential flux of protons estimated with the AP8MIN model in SPENVIS at the orbit with 550 km altitude and 2.5° inclination for 4.25 years of mission starting on 1 Jan 2022.

4.3 Accuracy of the AP8 model

The AP8 model has been adopted in the 70s and has been verified for more than 30 years [RD-43]. The accuracy of AP8 at LEOs is discussed in literature for the data of the Shuttle (in orbit at 28.5° inclination) and proton fluxes of energy >30 MeV. As

reported in [RD-16], the accuracy of AP8 for orbits with altitude of 500 – 600 km is between a factor of ~1.5 and ~2, as shown in Figure 3 (from [RD-16]).

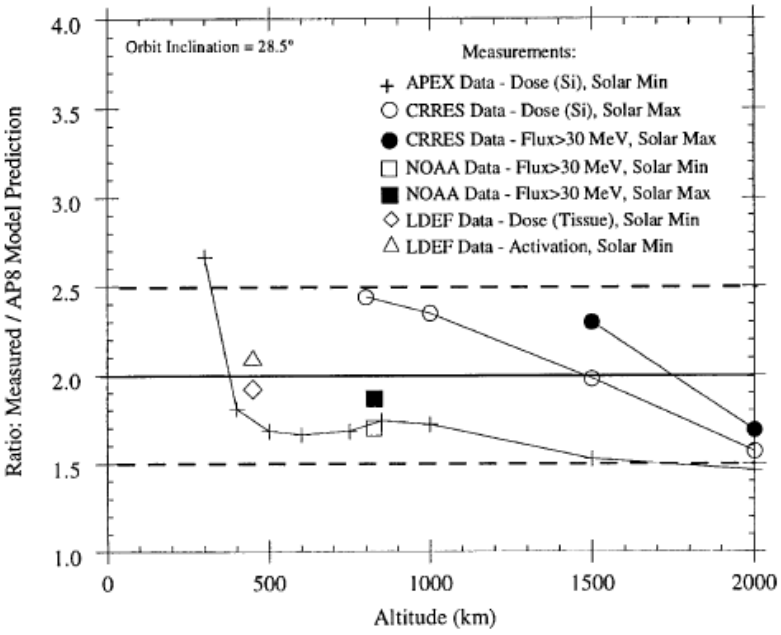

Figure 3: Comparison of flight data with predictions using AP8 trapped proton model for circular orbits with 28.5° inclination [RD-16].

In a different reference, at the same inclination and for altitudes ranging from 500 to 600 km, the agreement between the measured dose and expected from AP8 is within a factor of ~3 (see [RD-17]).

4.4 The new AP9 model and the comparison with the data

During the LOFT Assessment Phase, a new model for trapped protons, named AE9 AP9 SPM, has been proposed by Ginet et al. [RD-10] and was considered as a possible candidate to replace AP8 and AE8 in the future.
In order to verify the predictions of this new model, we compared the flux of protons from AP8 and AP9 with the data collected between 1996 and 2002 by the Particle Monitor aboard the BeppoSAX satellite. The Particle Monitor has an energy threshold of ~20 MeV for protons. The orbit of BeppoSAX has an altitude between 500 km and 600 km and an inclination of ~3.9° (see [RD-11] for details).

4.4.1 The data of the BeppoSAX Particle Monitor

BeppoSAX was launched on April 1996 in an Equatorial LEO with ~600 km altitude and ~3.9° inclination. The satellite re-entered the atmosphere on April 2002, when its orbit decayed beyond ~450 km. As described in [RD-11], the Particle Monitor (PM) is composed of a 2 cm diameter and 5 mm thick plastic scintillator, encapsulated in a 2 mm thick aluminum frame and read-out by a PMT. The nominal threshold for protons is 20 MeV [RD-11].
The inclination of the BeppoSAX orbit is similar to the values indicated for LOFT in [AD-1] and [AD-5]. For our analysis we select six representative observation periods (OP), spanning about 1 – 3 days each and at about one year distance between them, in

order to sample the proton environment at different altitudes following the decay of the satellite orbit and at different phases of the solar cycle. We show in Figure 4 the values of the BeppoSAX altitude during each of these OPs. In the selected periods, the satellite altitude ranges between 596 km and 547 km, similar to the baseline values for the altitude of the LOFT orbit ([AD-1] and [AD-5]).

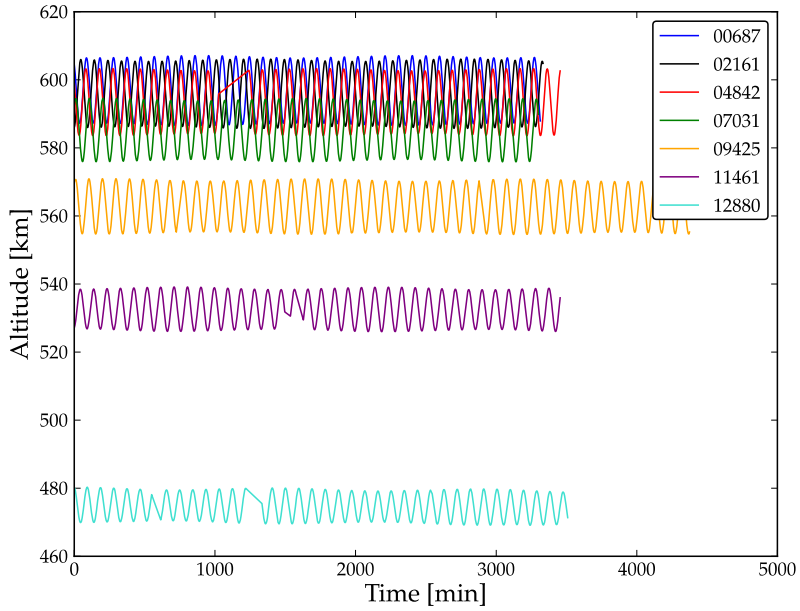

Figure 4: Altitude of the BeppoSAX satellite during the six observation periods selected in our analysis.

4.4.2 Comparison of the BeppoSAX PM data with AP8MIN and AP9

We simulated the predicted integral proton fluxes for energy > 20 MeV with the AP8MIN and AP9 models using the satellite ephemeris for each BeppoSAX observation. We run both AP9 and AP8MIN using the software Ae9Ap9_version_1.04.001. In the periods selected for the analysis, the altitude of the BeppoSAX satellite ranges between 596 km and 547 km, the range of the altitude studied for LOFT, and the inclination of the orbit is ~3.9°. The selected energy value of 20 MeV for the integral fluxes corresponds to the threshold of the BeppoSAX PM [RD-11].
We compared the predictions of AP8MIN and AP9 with the PM data, both as a 1-D time series and a 2-D geographical flux map. The maps of the SAA are shown only for the interval of latitude values spanned by BeppoSAX, i. e. between -3.9° and +3.9°. An example plot of the measured count rate during an OP is shown in Figure 5. Moreover, we computed the duration of the passages through the SAA, defined as the time interval during which the predicted model flux or the measured count rate is above a threshold defined as 3σ above the average off-SAA background level. Since at the orbit selected for LOFT the flux of trapped protons is almost completely concentrated in the SAA, our analysis is representative of the trapped protons in orbit.

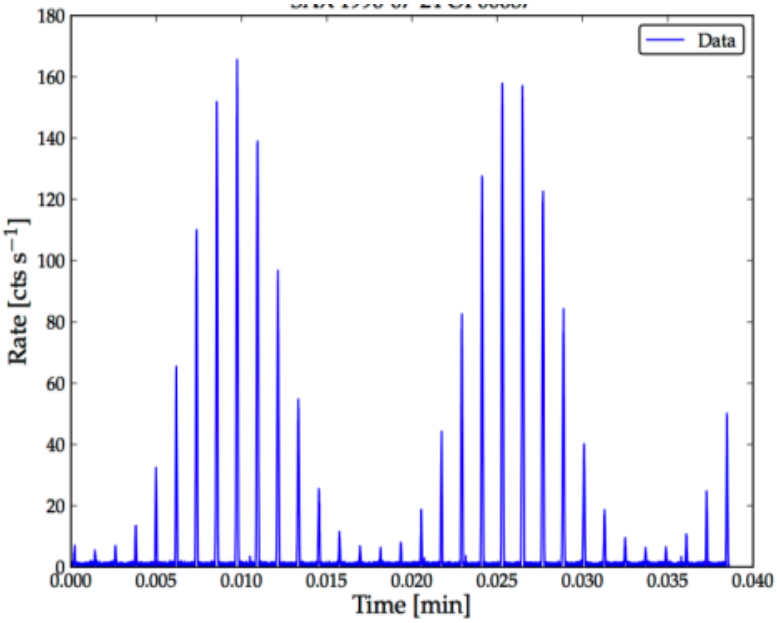

Figure 5: Measured counting rate of the BeppoSAX PM during the OP 687.

We summarise the reference to the figures produced in our analysis in Table 6.

Table 6: Summary of the plots of the comparison between AP8MIN, AP9 and the BeppoSAX PM data.

OP	Altitude	Map of the SAA with AP8MIN	Map of the SAA with AP9	Map of the SAA with the PM data	Passage duration
687	596 km	Figure 6	Figure 7	Figure 8	Figure 9
2161	595 km	Figure 10	Figure 11	Figure 12	Figure 13
4842	592 km	Figure 14	Figure 15	Figure 16	Figure 17
7031	584 km	Figure 18	Figure 19	Figure 20	Figure 21
9425	562 km	Figure 22	Figure 23	Figure 24	Figure 25
10469	547 km	Figure 26	Figure 27	Figure 28	Figure 29

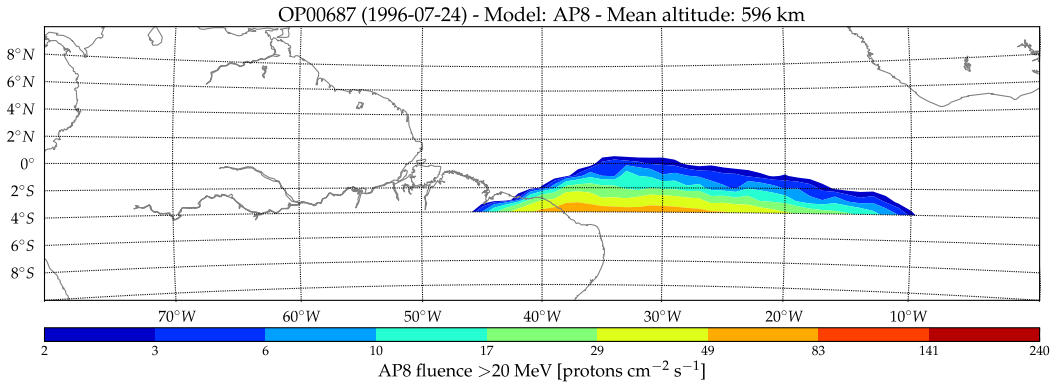

Figure 6: Map of the predicted proton flux in the SAA from the AP8MIN model for a mean altitude of 596 km (OP 687).

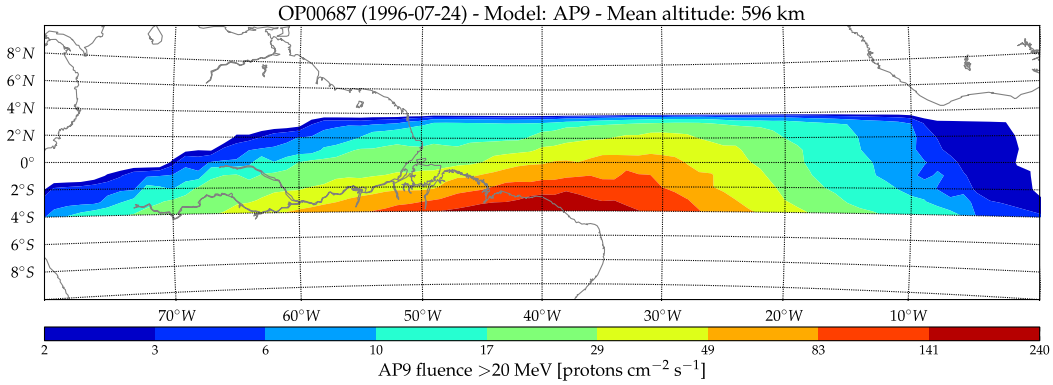

Figure 7: Map of the predicted proton flux in the SAA from the AP9 model for a mean altitude of 596 km (OP 687).

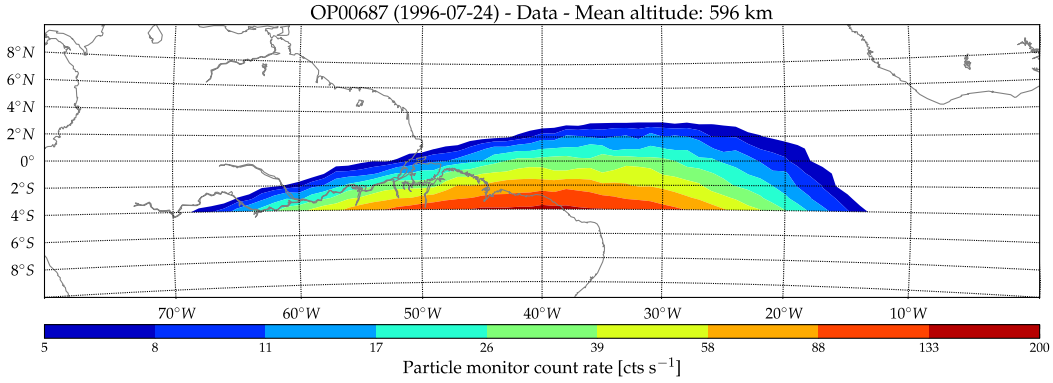

Figure 8: Map of the measured count rate in the SAA with the BeppoSAX PM for a mean altitude of 596 km (OP 687).

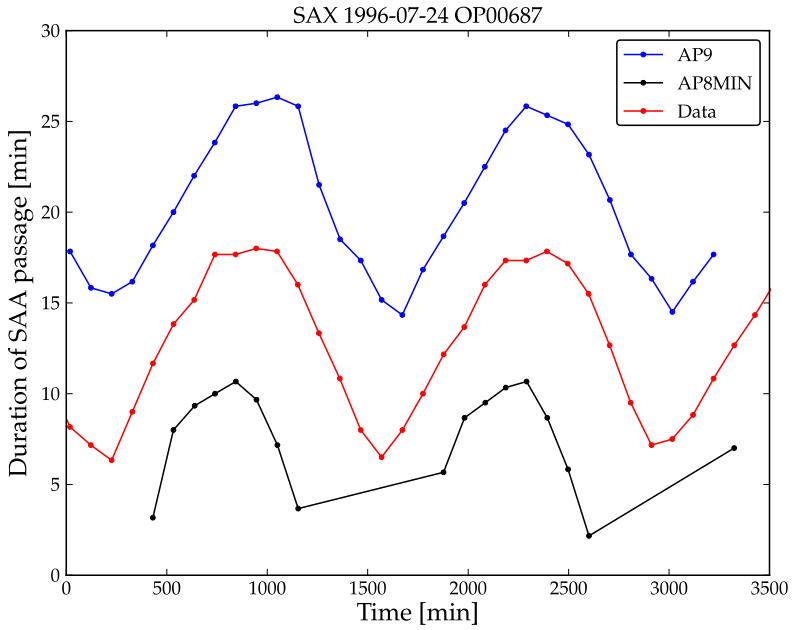

Figure 9: Duration of the passage through the SAA from AP8MIN (black line) AP9 (blue line) and PM data (red line) for a mean altitude of 596 km (OP 687).

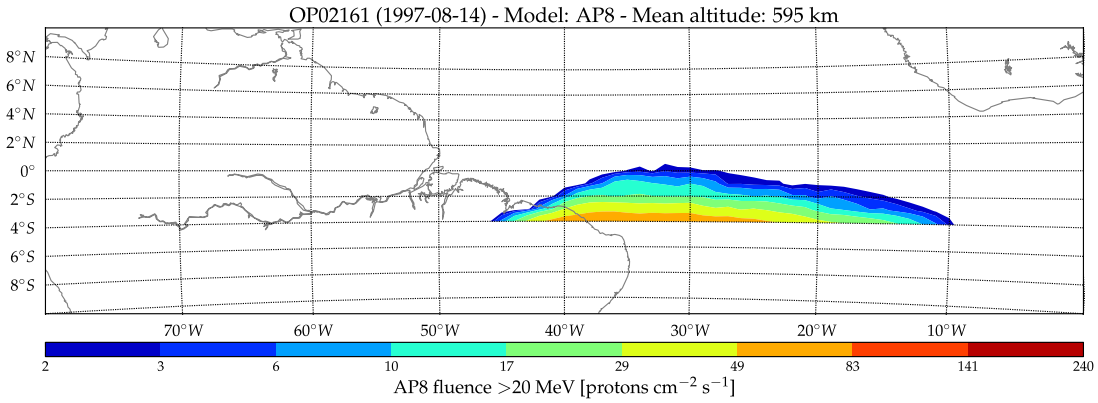

Figure 10: Map of the predicted proton flux in the SAA from the AP8MIN model for a mean altitude of 595 km (OP 2161).

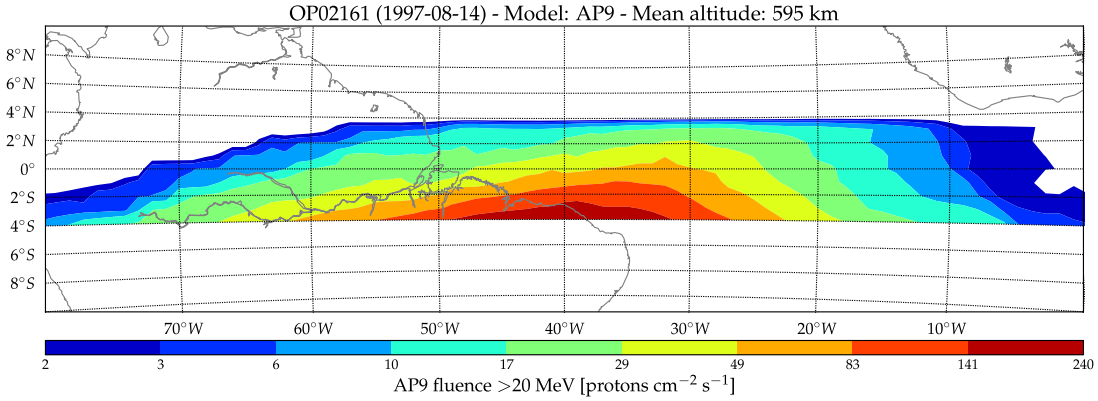

Figure 11: Map of the predicted proton flux in the SAA from the AP9 model for a mean altitude of 595 km (OP 2161).

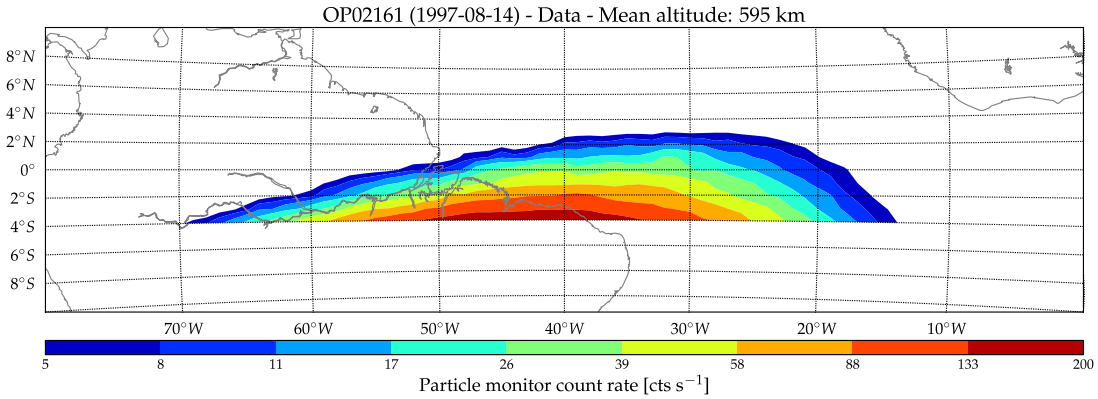

Figure 12: Map of the measured count rate in the SAA with the BeppoSAX PM for a mean altitude of 595 km (OP 2161).

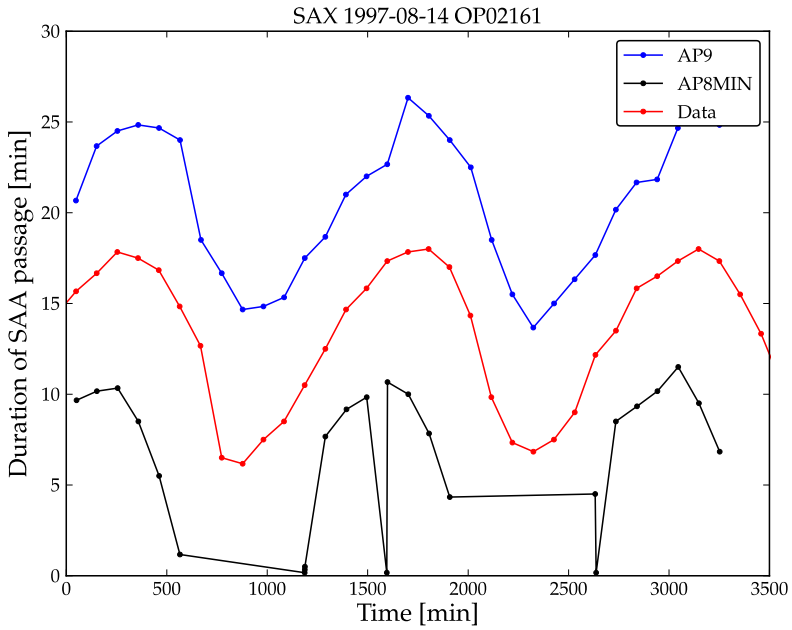

Figure 13: Duration of the passage through the SAA from AP8MIN (black line) AP9 (blue line) and PM data (red line) for a mean altitude of 595 km (OP 2161).

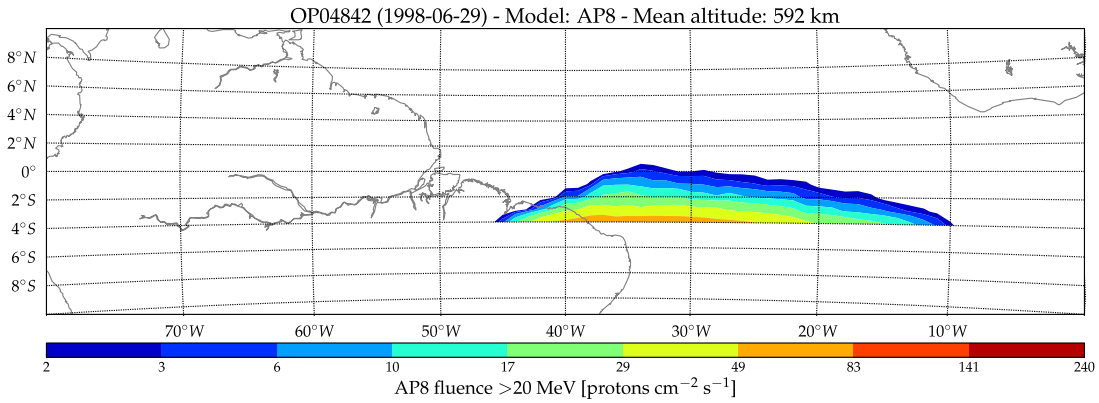

Figure 14: Map of the predicted proton flux in the SAA from the AP8MIN model for a mean altitude of 592 km (OP 4842).

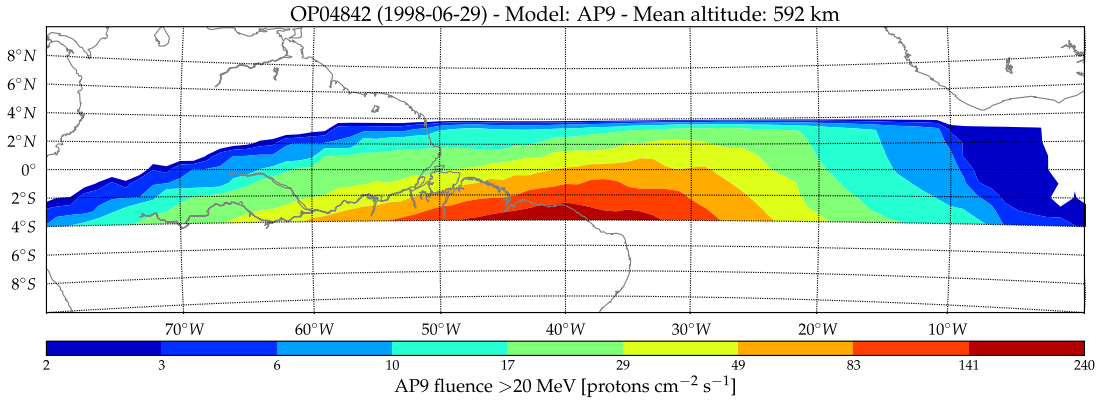

Figure 15: Map of the predicted proton flux in the SAA from the AP9 model for a mean altitude of 592 km (OP 4842).

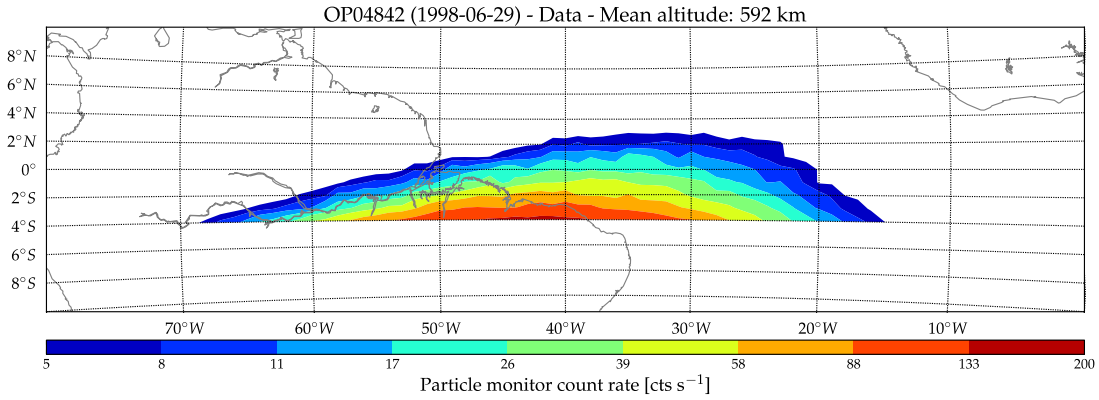

Figure 16: Map of the measured count rate in the SAA with the BeppoSAX PM for a mean altitude of 592 km (OP 4842).

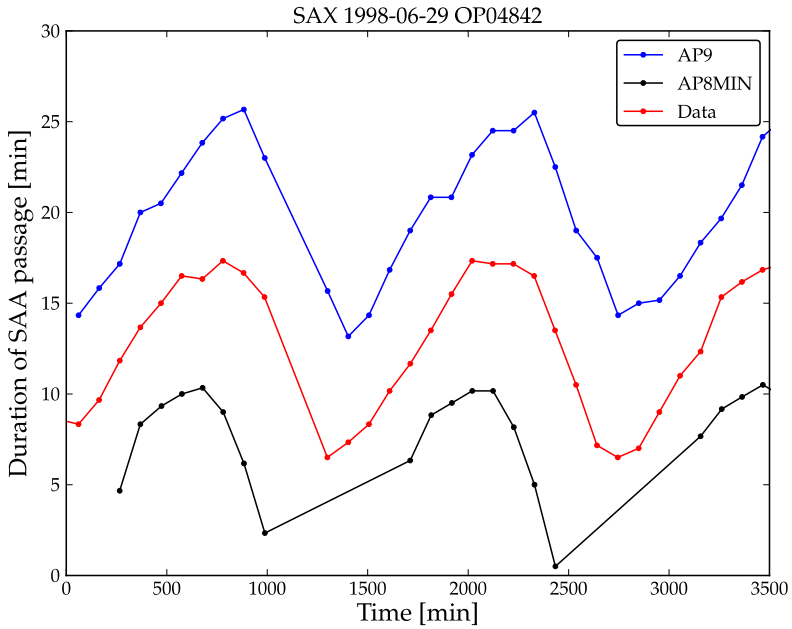

Figure 17: Duration of the passage through the SAA from AP8MIN (black line), AP9 (blue line) and PM data (red line) for a mean altitude of 592 km (OP 4842).

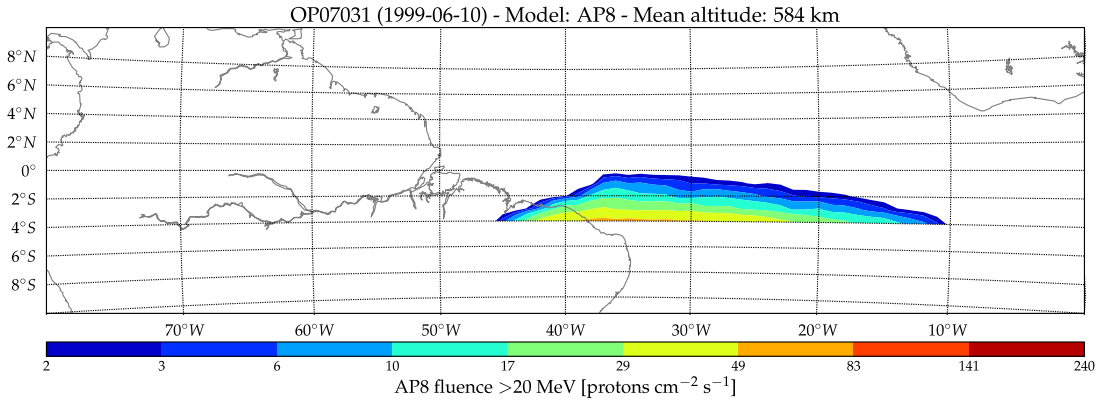

Figure 18: Map of the predicted proton flux in the SAA from the AP8MIN model for a mean altitude of 584 km (OP 7031).

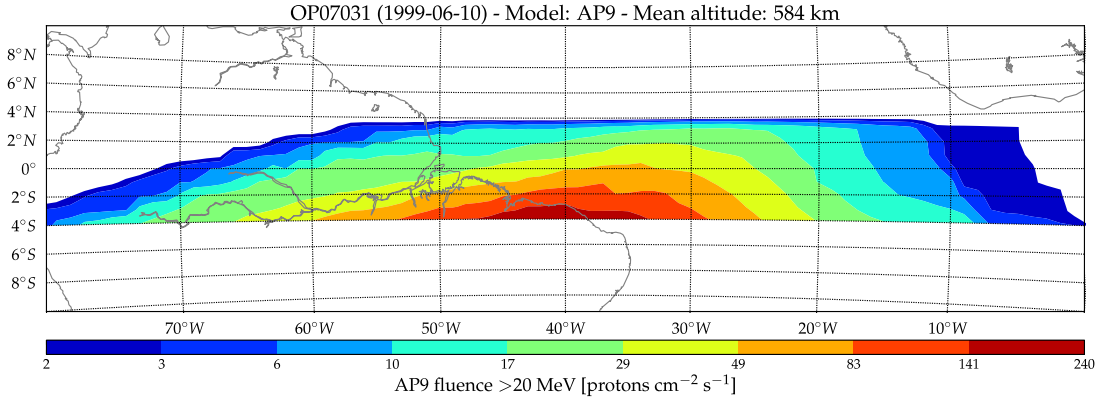

Figure 19: Map of the predicted proton flux in the SAA from the AP9 model for a mean altitude of 584 km (OP 7031).

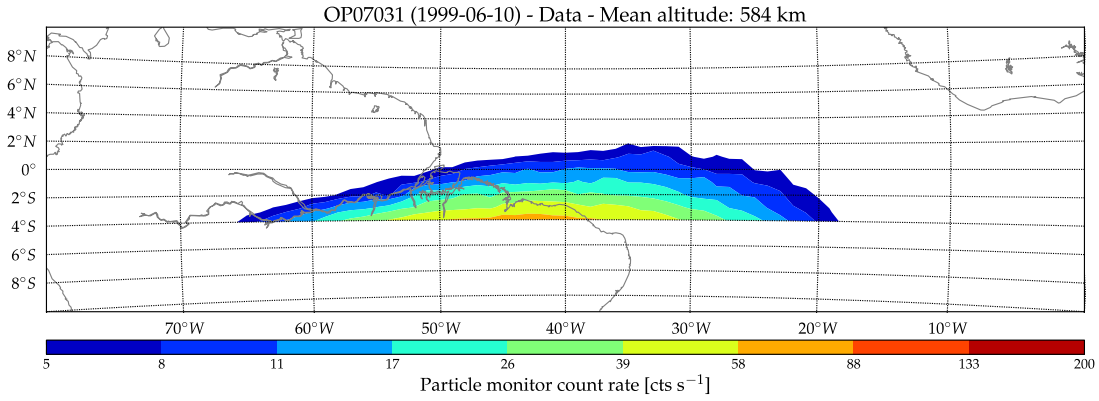

Figure 20: Map of the measured count rate in the SAA with the BeppoSAX PM for a mean altitude of 584 km (OP 7031).

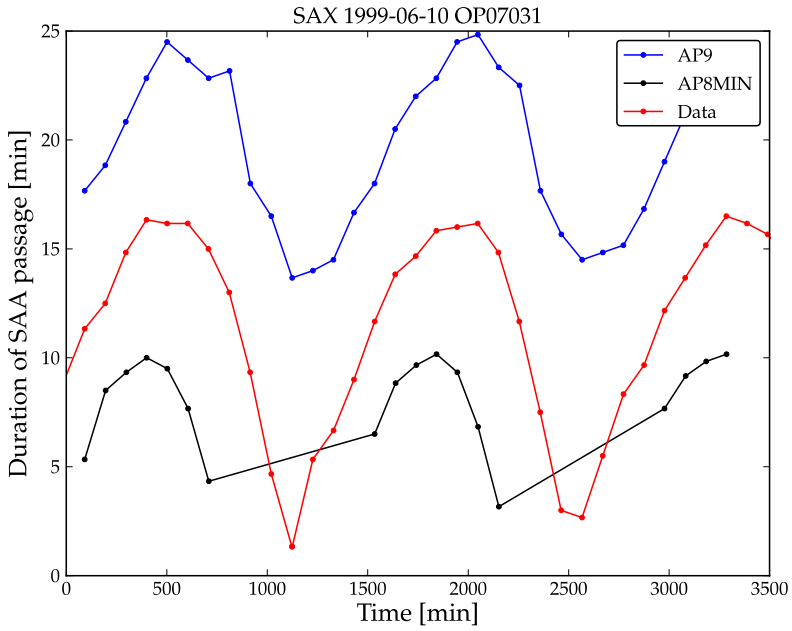

Figure 21: Duration of the passage through the SAA from AP8MIN (black line), AP9 (blue line) and PM data (red line) for a mean altitude of 584 km (OP 7031).

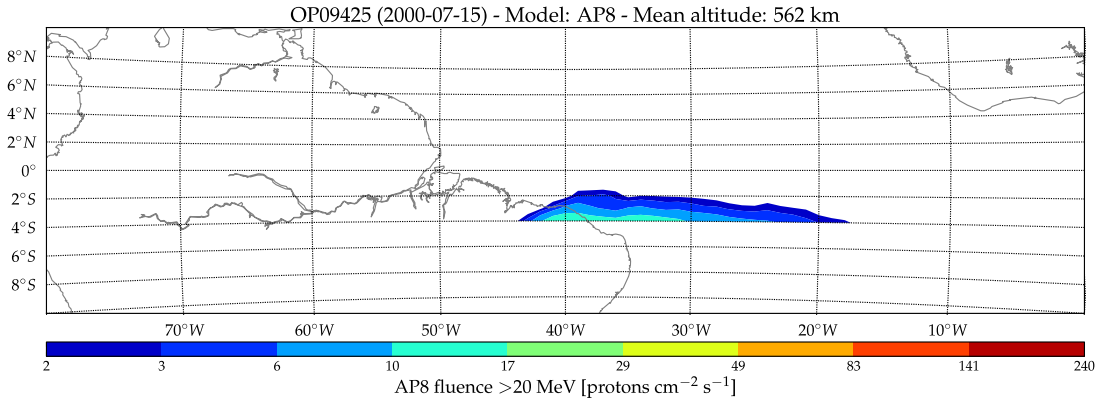

Figure 22: Map of the predicted proton flux in the SAA from the AP8MIN model for a mean altitude of 562 km (OP 9425).

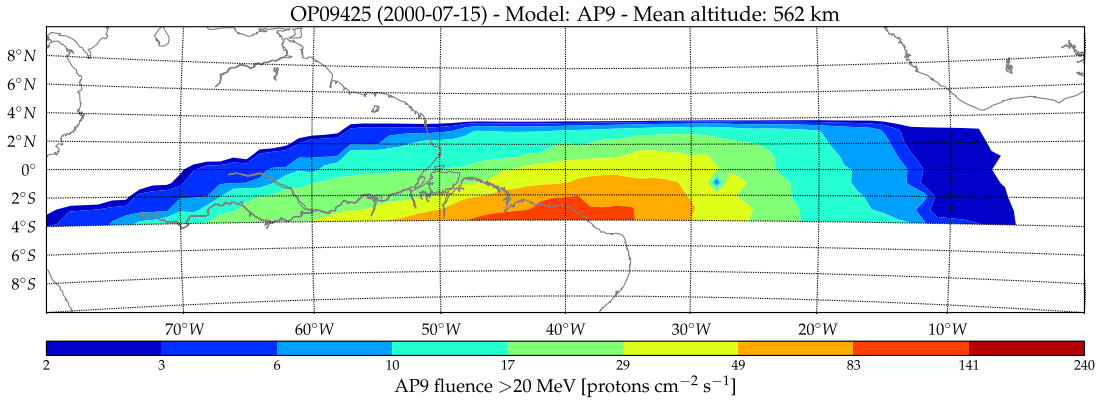

Figure 23: Map of the predicted proton flux in the SAA from the AP9 model for a mean altitude of 562 km (OP 9425).

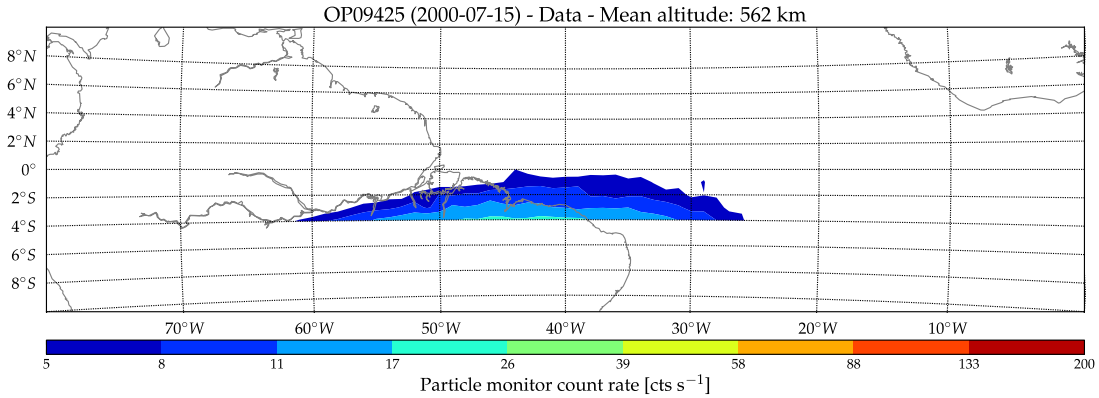

Figure 24: Map of the measured count rate in the SAA with the BeppoSAX PM for a mean altitude of 562 km (OP 9425).

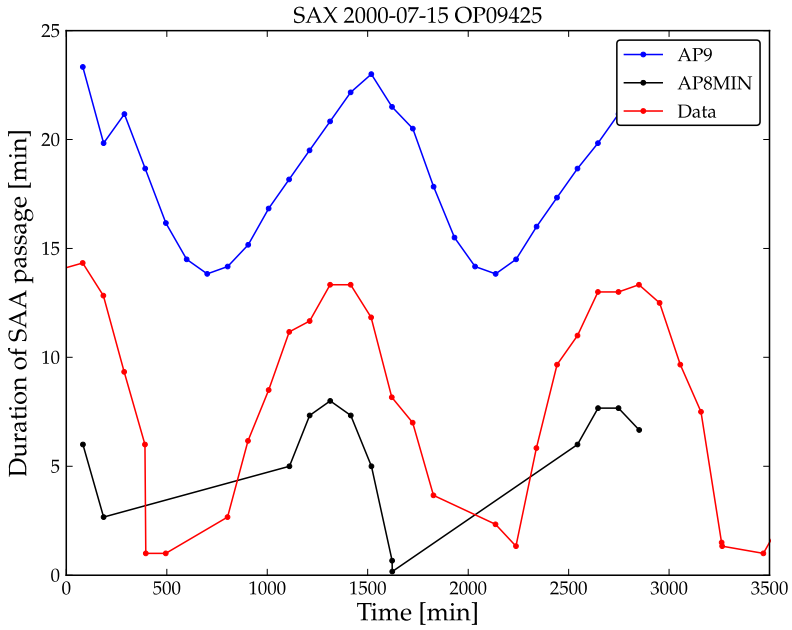

Figure 25: Duration of the passage through the SAA from AP8MIN (black line), AP9 (blue line) and PM data (red line) for a mean altitude of 562 km (OP 9425).

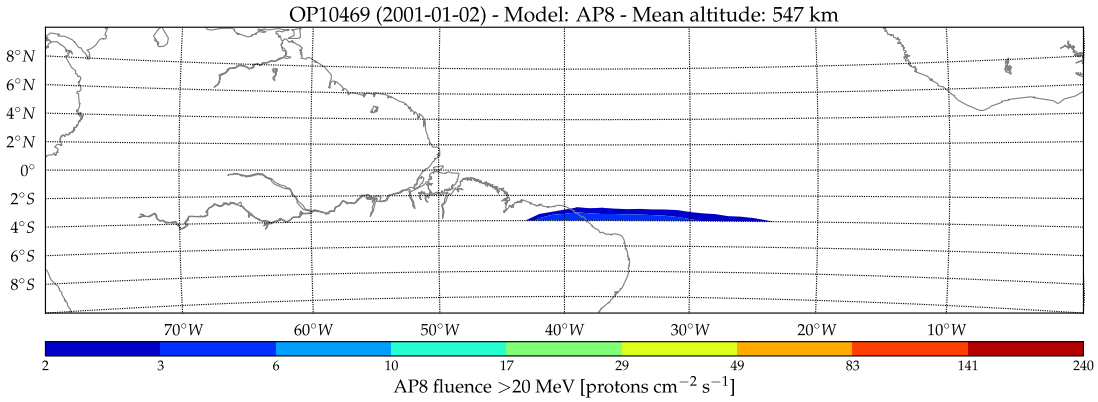

Figure 26: Map of the predicted proton flux in the SAA from the AP8MIN model for a mean altitude of 547 km (OP 10469).

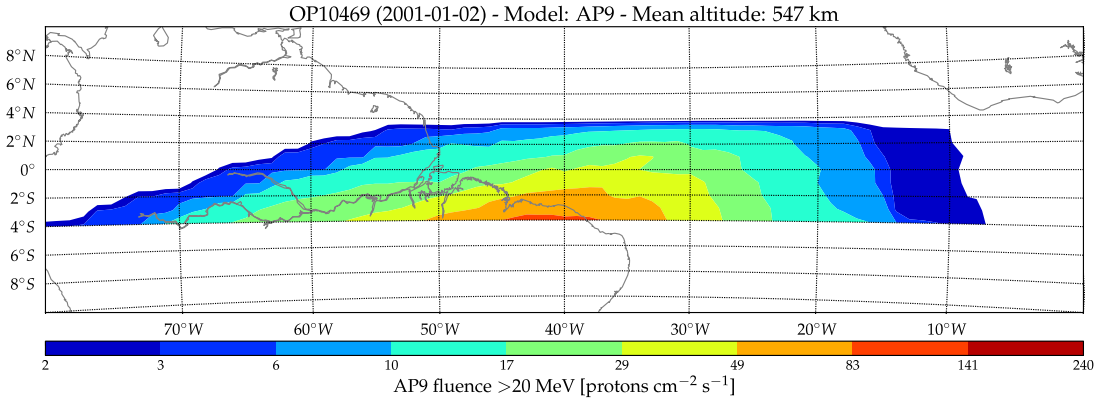

Figure 27: Map of the predicted proton flux in the SAA from the AP9 model for a mean altitude of 547 km (OP 10469).

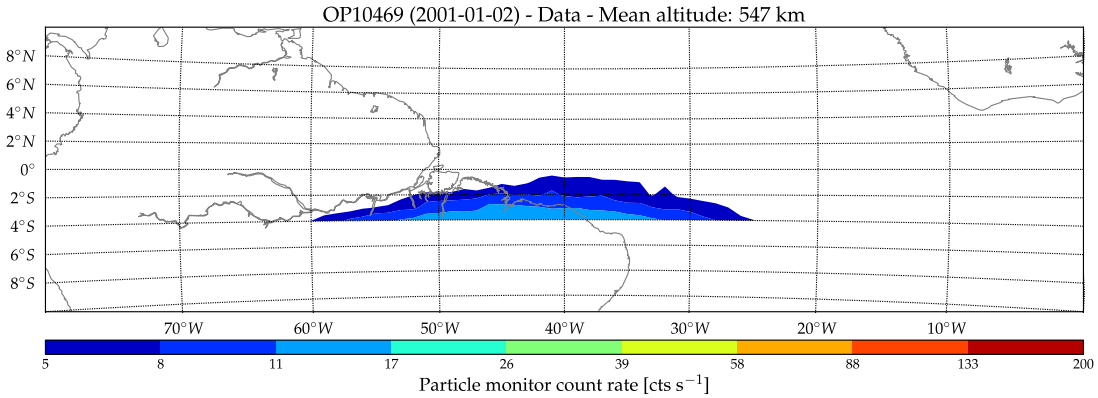

Figure 28: Map of the measured count rate in the SAA with the BeppoSAX PM for a mean altitude of 547 km (OP 10469).

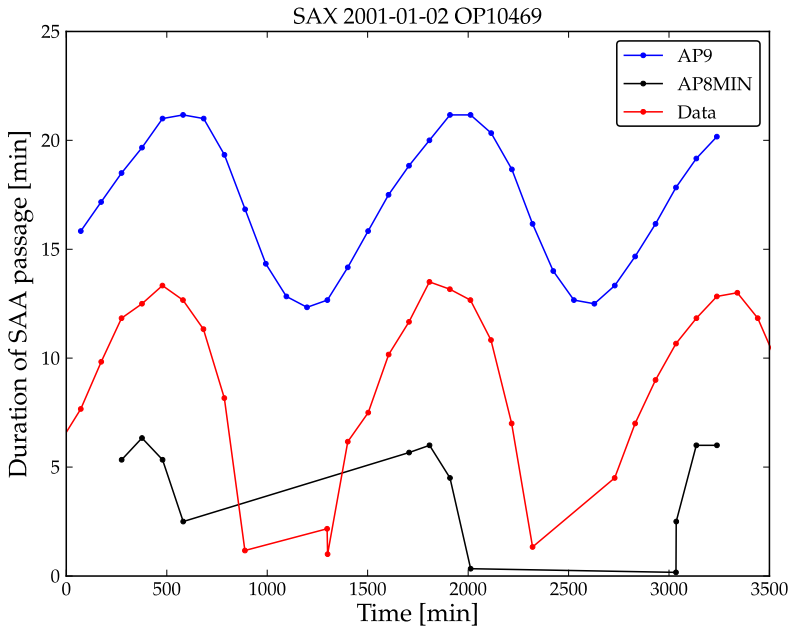

Figure 29: Duration of the passage through the SAA from AP8MIN (black line), AP9 (blue line) and PM data (red line) for a mean altitude of 547 km (OP 10469).

As shown in the previous plots, in our analysis we find that the AP9 model systematically overestimates the fluence and the geographical extension of the SAA, when compared to the data of the BeppoSAX PM. For example, around 600 km altitude the SAA in AP9 extends well above a latitude of +4° (although the map in Figure 7 is truncated because the inclination of the BeppoSAX orbit is ~3.9°) while the counting rate measured by the PM is consistent with the typical level outside the SAA for a latitude above ~3° (see Figure 8). Similarly, the extension in longitude of the SAA estimated with AP9 is much higher than that measured by the PM. The overestimation of the extension of the SAA from AP9 in both latitude and longitude is observed at all altitudes (see Figure 11, Figure 15, Figure 19, Figure 23 and Figure 27) when compared with the data of the BeppoSAX PM (in Figure 8, Figure 12, Figure 16, Figure 20, Figure 24, Figure 28).
AP8MIN does not take into account the westward drift of the SAA (that averages around 0.3 degrees per year, [RD-44]), thus the maximum fluence in the maps is found eastward than measured by the BeppoSAX PM. Moreover, the fluence and the latitude extension of the SAA in AP8MIN are smaller than measured by the PM.
We showed in Sec. 4.3 that in literature the accuracy of the AP8 model, for orbits with altitude similar to LOFT but at a higher inclination, is a factor of ~3. Correspondingly, the duration of the passages through the SAA derived from AP9 is about a factor of ~2 longer than measured by the PM, which is on average consistent with AP8MIN, as shown in Figure 30.
As a result of the comparison between AP9 and AP8, we will derive in Sec. 4.5 the margins to be applied to the models to estimate the radiation environment for LOFT.

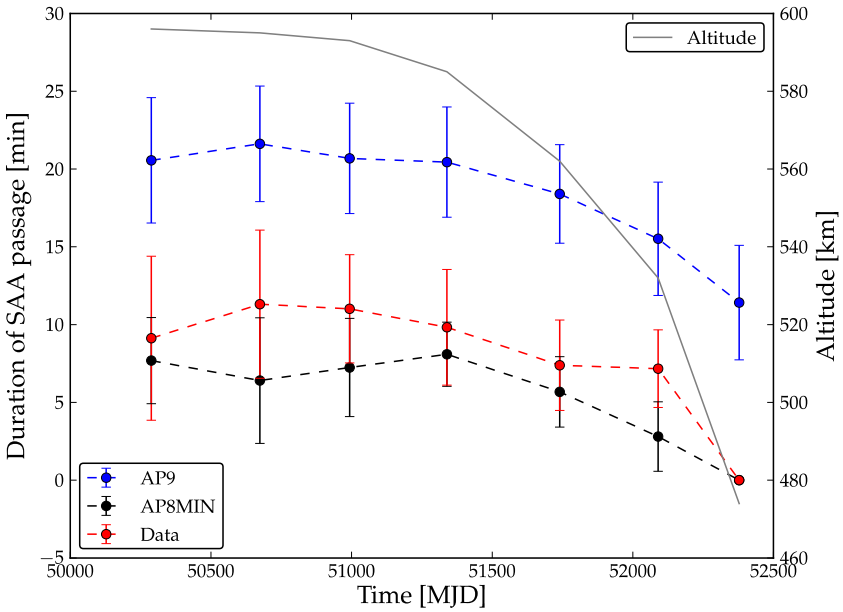

Figure 30: Duration of the passage through the SAA (left axis) at different altitudes (right axis) estimated with AP8MIN (black curve) and AP9 (blue curve) and measured with the BeppoSAX PM (red curve).

In Figure 31 we show the average ratio (for each SAA passage) between the predicted AP8 or AP9 model fluence versus the detected counts, as a function of the altitude. In a certain sense, the ratio between the model and the detected counts can be interpreted as a sort of "conversion efficiency", depending only on the detector details, and thus should be at least weakly dependent on the altitude. That is, if the model is correct, the dependence of the detected counts on the altitude should mimic the model one, since the detector response is the same. As clearly shown in Figure 31, the "proton conversion efficiency" from the AP9 model strongly depends on the satellite altitude, while it is almost constant for AP8MIN. This indicates that the AP8MIN model seems to reproduce more correctly the flux behaviour with respect to the altitude.
Finally, we show in Figure 32 the variation with the satellite altitude of the flux predicted by the models and the measured counts by the PM. All the data in Figure 32 are normalized to the value at 600 km. It is clearly seen in Figure 32 that AP8MIN and the measured counts from the BeppoSAX PM approximately follow the same trend, while AP9 is significantly flatter as a function of the altitude.

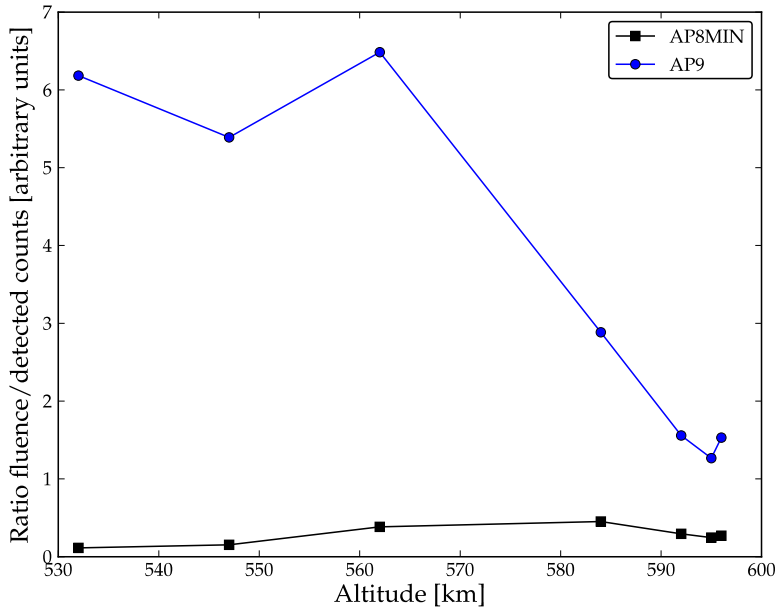

Figure 31: Average ratio (for each SAA passage) between the predicted AP8 or AP9 model fluence versus the detected counts, as a function of the altitude

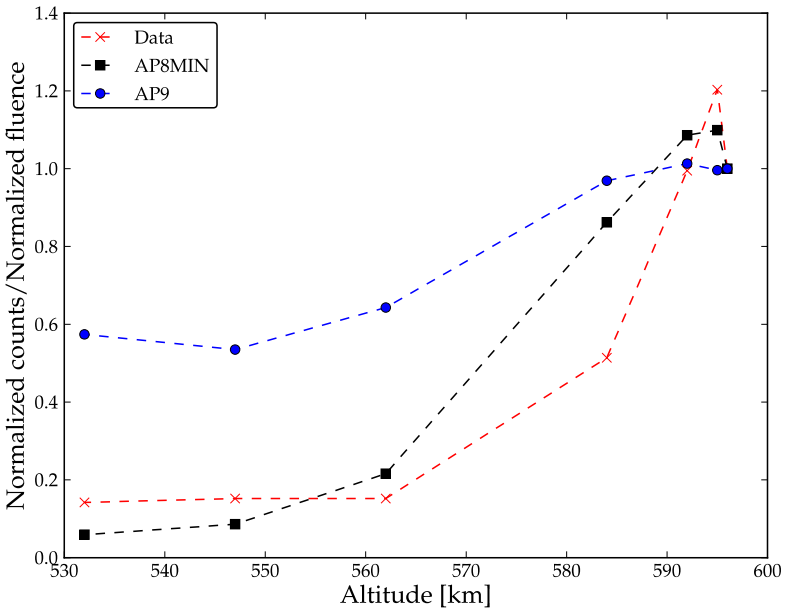

Figure 32: Variation of the normalized fluence of AP8MIN (black curve) and AP9 (blue curve) and normalized counts from the BeppoSAX PM (red curve) as a function of altitude.

4.4.3 Independent verification by an ESA team

An independent verification of the AP9 model has been performed by an ESA team and is reported in [RD-12]. Here we summarise the main results of the verification.

From the comparison of the maps of the proton flux from AP9 and AP8MIN at the representative altitudes of 500 km and 1000 km, the SAA clearly has a higher peak and a wider extension in AP9 than in AP8MIN.
The authors of AP9 compared the prediction of the model with the POES data, in a polar orbit at 850 km altitude. Especially at low fluxes, corresponding to the edge of the SAA encountered by LOFT in its equatorial LEO, the predictions of AP9 are about two orders of magnitude higher than the POES data. The comparison is performed for a proton energy of 16 MeV.
The predictions of AP9 and AP8MIN are also verified against the data of the SREM instrument aboard the PROBA-1 satellite, on a polar orbit with perigee at 550 km and apogee at 663 km, representative of the altitude for the LOFT orbit (see [RD-45] and http://www.esa.int/Our_Activities/Observing_the_Earth/Proba-1). In this verification, the integral proton flux above 12 MeV (S34 channel of Proba-1 SREM) and 24 MeV (S15 channel of Proba-1 SREM) are considered. The proton fluxes from the channels given above are extracted for satellite latitude values between -5° and +5° and are compared with AP9 and AP8MIN. From the comparison, the Proba-1 data are in the middle between AP8MIN, generally lower, and AP9, generally higher. The difference between the data and the models depends on the year in which the data are extracted, with respect to the solar cycle.

4.4.4 Conclusion of the comparison between AP9 and AP8

The comparison between the data of the BeppoSAX PM and the models for trapped protons AP9 and AP8MIN, run using the software Ae9Ap9_version_1.04.001 , shows that the AP9 model gets less and less accurate as the orbit altitude decreases. For example, the data in Figure 32 show that the extrapolation to low altitude (600 km to 500 km) in AP9 is far "too flat" as compared to measured data. The number of detected counts per unit fluence increases by a factor 6 going from 600 km to 530 km, hard to understand physically.
AP8MIN shows a more consistent behaviour, with a fluence scaling in the same way as the real data as a function of altitude. In fact, as shown in Figure 31, the number of detected counts per unit fluence remains stable for different values of the altitude. This effect is also confirmed in terms of SAA passage duration and SAA maps. However, "plain" AP8MIN clearly shows some underestimation of the total absolute fluence and a margin is recommended.
The conclusion of our analysis is that AP8MIN is a reliable model for the trapped protons in LEO, but it requires a margin of ~5.
As a conclusion, the author of [RD-12] suggests to adopt the AP8MIN model, as recommended in [RD-8], and to apply a margin of a factor of 3 to compensate the difference with respect to the data of Proba-1, with an additional factor of 2 as a design margin (see LOFT EID-A document [AD-4]), for a total margin of a factor of 6.

4.5 The adopted model for trapped protons and the margins for LOFT

In conclusion, we adopt the AP8MIN model increased by a factor of 5 to describe the radiation environment of LOFT. In the design of the LAD and WFM we adopted an additional 4x margin, for a total margin of 3.0 × 10^6 p/cm^2 for the 550km, 2.5° orbit, a factor 20 larger than the fluence provided by AP8MIN in SPENVIS. This is 3.3 times higher than the total margin required by ESA. The above fluence was used to set the operative temperature requirements of the LAD (Sec. 9.3) and WFM (Sec. 9.4), and to

estimate the expected Total Ionising Dose (TID, sec. 7.1) and the variation of the Charge Collection Efficiency (CCE, Sec. 11.2).

4.6 Soft protons

For satellites such as LOFT in LEO near the Equator, an additional component of charged particles is represented by a low-energy and highly directional population of protons near the Geomagnetic Equator and at an altitude between 500 km and 1000 km [RD-14].
The soft proton component is included neither in the AP8 model nor in the SPENVIS package. The flux of the soft protons is almost independent on the altitude between 500 km and 1000 km and the differential spectrum can be approximated as

$$f(E) = A\left[1 + \frac{E}{kE_0}\right]^{-k-1} \quad (2)$$

and is shown in Figure 33 from [RD-14]. We assume the proton spectrum f(E) described in [RD-14] for the worst case of the "disturbed geomagnetic conditions": A = 330, k = 3.2 and E_0 = 22 keV .
The flux of the soft proton component is characterised by a very narrow distribution around the pitch angle θ [RD-14]: ~$\sin(\theta)^n$, with n = 6 – 15. To be conservative we choose n = 6. The maximum of the distribution is in the direction of the zenith at the Geomagnetic Equator, the detectors are assumed to be oriented always towards the maximum of the flux (conservative approach).

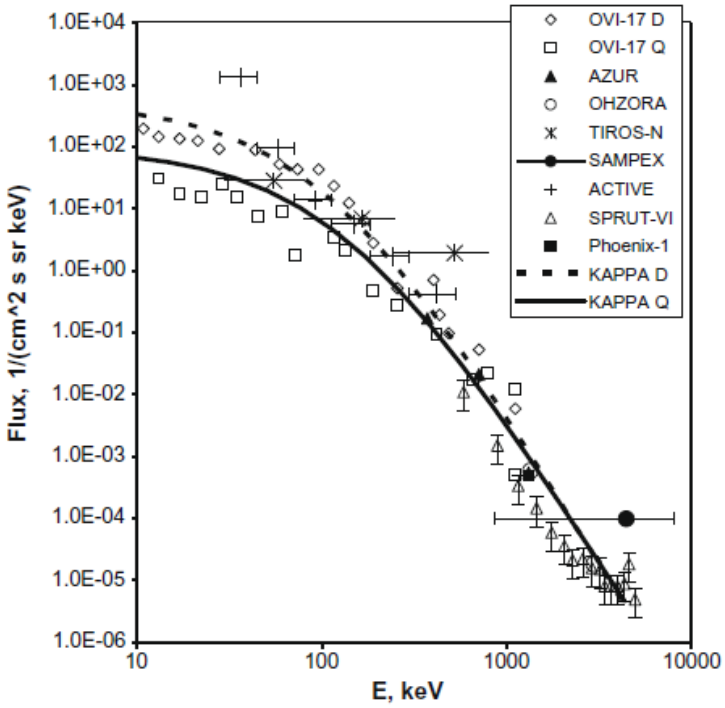

Figure 33: Differential spectrum of the soft proton component, from [RD-14].

We specifically estimated the displacement damage and the TID produced by the soft proton component for the geometries of the LAD and WFM. The method to calculate

the displacement damage is summarised in Sec. 6.1.3, to calculate the TID is in Sec. 6.2.2. More details are given in [RD-15]. The results of the displacement damage from soft protons on the LAD are summarised in Sec. 7.2.2, on the WFM in Sec. 7.2.5. The TID is summarised in Sec. 7.1 .

5 ASSUMED SHIELDING

In this section we summarize for the LAD and WFM the materials around the SDDs, which shield the detectors from the interaction of protons in orbit.
The equivalent thickness of aluminum of the shielding for the LAD and WFM, derived from the lists of materials, is provided as input to SPENVIS to estimate the displacement damage and the TID.

5.1 Description of the LAD shielding

We derived the properties of the materials which shield the SDDs of the LAD from the mass model defined in [RD-42] in order to simulate the instrument background with the GEANT4 Montecarlo code.
The list of the materials which shield the LAD SDDs from protons impinging from the illuminated side is reported in Table 7 (from [RD-5] and [RD-42]). The acceptance angle for protons in this condition is 2π sr.

Table 7: Shielding of the LAD above the SDD for trapped protons, from top to bottom. The covered solid angle is 2π sr.

Component	Material	Covering factor [%]	Density [g/cm^3]	Thickness [μm]	Surface density [g/cm^2]	Thickness Al equivalent [mm]
Thermal screen filter	Polymide	100	1.4	1	1.4×10^{-4}	5.2×10^{-4}
	Al	100	2.7	0.08	2.2×10^{-5}	8.1×10^{-5}
Collimator filming	Al	100	2.7	0.08	2.2×10^{-5}	8.1×10^{-5}
Collimator	Lead glass	30	3.3	6000	0.6	2.2
SDD passivation and field oxide	SiO_2	100	2.2	0.5	1.1×10^{-4}	4.1×10^{-4}
	SiO_2	83	2.2	0.18	3.3×10^{-5}	1.2×10^{-5}
	SiO_2	17	2.2	0.2	7.5×10^{-6}	2.8×10^{-5}
SDD metallization	Al	93	2.7	0.5	1.3×10^{-4}	4.8×10^{-4}
SDD undepleted layers	Si	83	2.3	0.4	7.6×10^{-5}	2.8×10^{-4}
Overall					0.6005	2.224

The list of materials below the SDDs, i. e. which shield the detectors from the non-illuminated side, is reported in Table 8 (from [RD-5] and [RD-42]). Also in this case the acceptance angle is 2π sr.

Table 8: Shielding of the LAD below the SDD for trapped protons, from top to bottom. The covered solid angle is 2π sr.

Component	Material	Covering factor [%]	Density [g/cm^3]	Thickness [mm]	Surface density [g/cm^2]	Thickness Al equivalent [mm]
FEE support	CFRP	100	1.7	2.0	0.34	1.3
Backshield	Pb	100	11.34	0.5	0.57	2.1
Radiator	Al	100	2.7	1.0	0.27	1.0
Overall					1.18	4.4

The equivalent thickness of aluminum of the shielding for the LAD and WFM, derived from the lists of materials, is provided as input to SPENVIS to estimate the displacement damage and the TID.
Finally, the shielding materials for soft protons, with a solid angle of 3×10^{-4} sr, are listed in Table 9 (from [RD-15]).

Table 9: Shielding of the LAD for soft protons (above the SDD and inside the FoV), from top to bottom. The solid angle is 3×10^{-4} sr.

Component	Material	Covering factor [%]	Density [g/cm^3]	Thickness [μm]
Thermal screen filter	Kapton ($C_{22}H_{10}O_5N_2$)	100	1.4	1
	Al	100	2.7	0.08
Collimator filming	Al	100	2.7	0.08
SDD passivation and field oxide	SiO_2	100	2.2	0.5
	SiO_2	83	2.2	0.18
	SiO_2	17	2.2	0.2
SDD metallization	Al	93	2.7	0.5
SDD undepleted layers	Si	83	2.3	0.4

5.2 Description of the WFM shielding

The list of materials which shield the SDDs in the WFM from the interaction of trapped protons is reported in Table 10 (from [RD-5]). The equivalent thickness of aluminum of the shielding for the LAD and WFM, derived from the lists of materials, is provided as input to SPENVIS to estimate the displacement damage and the TID. The list of materials in the WFM FoV, used in [RD-15] for the calculation of the displacement damage and TID from soft protons, is given in Table 11.

Table 10: Shielding of the WFM for trapped protons, from top to bottom.

Component	Material	Solid angle [sr]	Density [g/cm^3]	Thickness [mm]	Surface density [g/cm^2]	Thickness Al equivalent [mm]
Coded mask	W (75 % covering factor)	2.5	19.2	0.11	0.22	0.8
Be layer	Be	2.5	1.85	0.025	4.6×10^{-3}	0.017
Collimator	CFRP	2π - 2.5	1.7	2.0	0.34	1.3
	W	2π - 2.5	19.2	0.15	0.29	1.1
	Mo, Cu	2π - 2.5	10.3; 8.9	0.05; 0.05	5.4×10^{-2}	0.2
Average		2π				1.9

Table 11: Shielding of the WFM for soft protons, from top to bottom (see [RD-15]).

Component	Material	Density [g/cm^3]	Thickness [μm]
Optical filter	Kapton ($C_{22}H_{10}O_5N_2$)	1.4	7.6
	SiO_2	2.2	0.16
Be layer	Be	1.85	25
SDD passive layers	SiO2	2.2	0.5
	Al	2.7	0.5
	SiO2	2.2	0.18

6 MODELS OF THE RADIATION DAMAGE

6.1 Model of the Displacement Damage

6.1.1 General formula

The interaction of charged and neutral particles on the silicon lattice of the SDDs may produce displacement damage. The most important effect produced by the displacement damage to a semiconductor detector in the fluence range expected for LOFT is the increase ΔI of the bulk leakage current, given by [RD-6]

$$\Delta I = \alpha \, \Phi_{eq} \, V \qquad (3)$$

where Φ_{eq} is the particle fluence incident on the device rescaled to the equivalent effect of 1 MeV neutrons, V is the detector volume in which the leakage current is measured and α is a coefficient of proportionality measured in dedicated tests, also known as the "current related damage rate" [RD-6]. The increase in leakage current is proportional to the particle fluence and is independent of the type of silicon material that is used (high or low resistivity, n- or p-type, high or low concentration of the impurities carbon and oxygen) as reported in [RD-18].
For our estimation we use in Eq. (3) the value $\alpha = 11.1 \times 10^{-17}$ A/cm measured at a temperature of -50 °C in [RD-6], where the annealing effect can be neglected, a conservative assumption for LOFT.

6.1.2 NIEL approximation and hardness factors

Apart from the proportionality to the fluence described in Eq. (3), the calculation of the displacement damage is based on the hypothesis that the damage is linearly dependent on the Non-Ionizing Energy Loss (NIEL), regardless of the particle type ξ (NIEL scaling hypothesis), and usually it is related to a reference value (that of 1 MeV neutrons, $D_n(1MeV) = 95$ MeV mb) by introducing a hardness factor k_ξ

$$k_\xi(E) = \frac{D_{d,\xi}(E)}{D_n(1MeV)} \tag{4}$$

The values of k for various particles and energies are reported in literature (see e. g. [RD-7] for neutrons, protons and pions). A plot with the comparison of the k factor for protons, neutrons and electrons at energies between 10^{-2} MeV and 10^4 MeV is shown in Figure 34, with data from [RD-7].

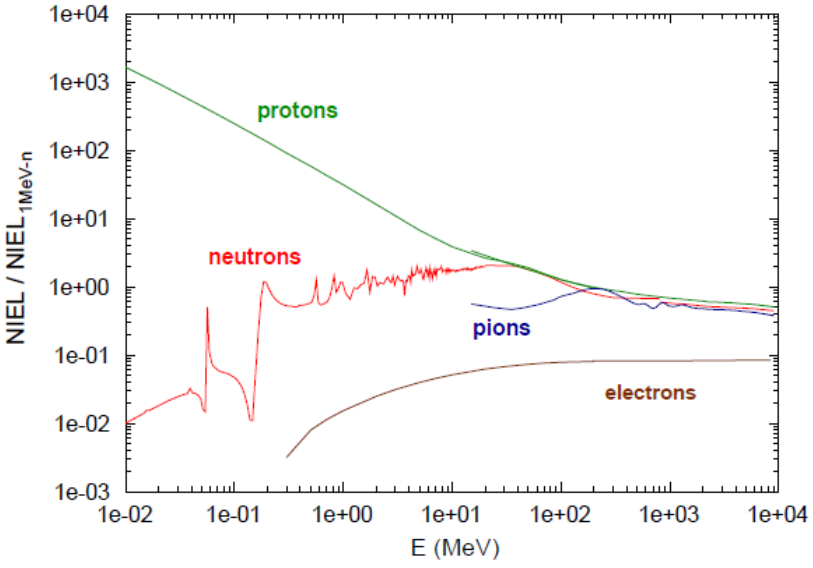

Figure 34: Comparison of the k factor for protons, neutrons and electrons at energies between 10^{-2} MeV and 10^4 MeV with data from [RD-7].

For LOFT we consider two cases. For the trapped protons (AP8 model) we calculate the equivalent fluence of 10 MeV protons that reproduce the damage. In this case, the

hardness factor k = 4.8 is calculated in [RD-6] specifically for a silicon detector with a thickness of 450 μm (the same as the LOFT SDDs) and protons of 10 MeV energy.
For the soft protons, instead, we have to take into account the energy lost by the particles in crossing the sensors by introducing an effective hardness factor

$$k_{eff}(E) = \frac{1}{L}\int_0^L \frac{D_d(E,x)}{D_n(1MeV)}dx \quad (5)$$

where L is the thickness of the SDD.

6.1.3 Approximations for trapped protons

We estimate the increase of the bulk leakage current produced by the displacement damage of trapped protons using Eq. (3). We assume the NIEL approximation in Eq. (4) and we propagate the proton fluence from the AP8MIN model through the shielding materials (see Sec. 5.1 for the LAD and Sec. 5.2 for the WFM) using a dedicated package in SPENVIS, which gives as output the fluence equivalent to protons of 10 MeV energy.

6.1.4 Approximations for soft protons

Since the soft proton component is not included in SPENVIS, in order to estimate the increase of the leakage current we integrated the displacement damage over the proton flux (see [RD-15] for the details of the calculation). We assume that the protons are orthogonally incident on the SDDs and we calculate Eq. (3) in the middle of the detector plane, where the fluence is maximal for the detectors. With these assumptions, the increase of leakage current is given by

$$\Delta I_{leak} = \alpha \cdot \eta \cdot V \cdot T \int_{\Delta\Omega} d\Omega \int_{E_{min}}^{E_{max}} k_{eff}(E,\theta) \cdot \Phi(E,\theta) dE \quad (6)$$

where α = 11.1 × 10^{-17} A/cm is the current related damage rate, η is the open area ratio of the collimator (for the LAD) or the coded mask (for the WFM), V is the anode volume, T is the mission duration, $\Delta\Omega$ is the solid angle, $k_{eff}(E,\theta)$ is the effective hardness factor and $\Phi(E,\theta)$ is the proton spectrum. Due to the small angular aperture of the LAD collimator the θ dependence could be neglected. In the WFM case, however, the angular dependence of the proton flux should not be neglected to avoid overestimating too much the damage (by a factor of ~2, see [RD-15]). In any case the effective hardness factor could be considered constant since the protons stop within the sensor volume and the energy lost in the passive materials of the SDD is generally small compared to the kinetic energy of the protons at the sensor surface (the exception being the energies at the lower end of the range).
We evaluated the proton fluxes $\Phi(E)$ at the SDD level by propagating the spectrum of the soft protons (Eq. (2) in Sec. 4.6) through the shielding materials with the SRIM software [RD-46]. The proton flux impinging on the SDDs is shown in Figure 35 for both the LAD (blue) and the WFM (red).

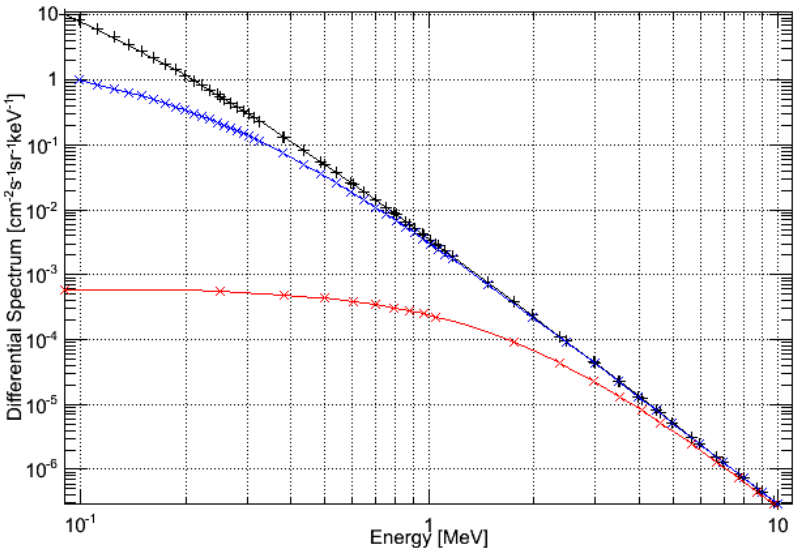

Figure 35: Incident soft proton spectrum (black) and filtered spectrum at the SDDs surfaces of the LAD (blue) and WFM (red) from [RD-15].

Then we estimated the effective hardness factor at these energies from the rate of vacancy data using SRIM and following the approach in [RD-6] and [RD-47]

$$k_{eff}(E) = \frac{A}{N_A \cdot \rho \cdot L \cdot D_n(1MeV)} \left(\frac{E_d}{0.4} + E_l \right) \int_0^L \frac{dN_d(E,x)}{dx} dx \quad (7)$$

In Eq. (7), ρ and L are the detector density and thickness, A is the molar weight of silicon, N_A is Avogadro's number, $D_n(1\ MeV)$ is the normalization value of the displacement damage for neutrons of 1 MeV energy (95 MeV mb), E_d is the displacement energy threshold of the silicon detector substrate (21 eV), E_l is the lattice binding energy loss (2 eV) and finally $dN_d(E,x)/dx$ is the distribution of dislocations as a function of depth x within the sensor. The effective hardness factor calculated with SRIM is shown in Figure 36.
In this estimation we assume that the protons are normally incident on the shielding materials and the SDDs. The angular distribution of the soft protons spectrum, $\Phi \sim \sin(\theta)^6$ [RD-14], is considered when integrating Eq. (6) on the angular component only in the WFM case.

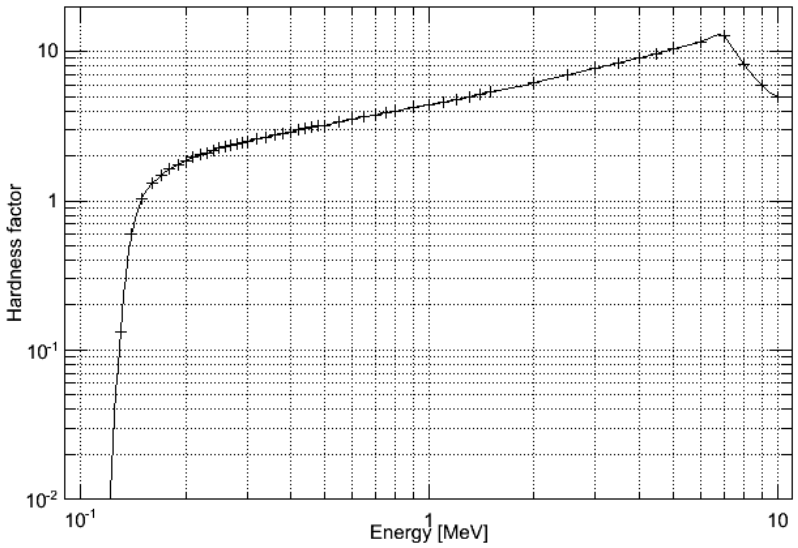

Figure 36: Effective hardness factor as calculated with SRIM for the LOFT SDD (from [RD-15]). At ~7 MeV the protons exit the detector and the damage decreases rapidly.

6.1.5 LOFT Mock Observing Plan and soft protons

Following [RD-14], the soft proton component has a very narrow distribution proportional to $\sim\sin(\theta)^6$ around the pitch angle θ. The maximum of this distribution is in the direction of the zenith at the Geomagnetic Equator. Consequently, the fraction of the soft proton fluence which can interact in the LOFT SDDs depends on the pointing direction of the satellite. The values of this fraction has been calculated for the LAD and WFM assuming the LOFT Mock Observing Plan. All the details of the calculation are given in [RD-15].
From the LOFT Mock Observing Plan, the average fraction of the soft proton fluence interacting in the SDDs is thus 6 % for the LAD and 19 % for the WFM.

6.2 Model of the Total Ionizing Dose

6.2.1 Total Ionizing Dose from trapped protons

The Total Ionizing Dose (TID) from the trapped proton component is calculated using the SHIELDOSE package of SPENVIS [RD-9] and the proton flux estimated with the AP8MIN model for orbits with altitude and inclination specified by the user.

6.2.2 Total Ionizing Dose from soft protons

Similarly to the displacement damage, the TID from the soft protons component has been estimated following the approach in Sec. 6.1.4. We use the same assumptions: we compute the TID at the center of the detection plane, where the fluence is maximal, and we assume that the protons are orthogonally incident on the SDDs. In the case of the TID, we compute using SRIM

$$TID = \frac{\eta \cdot T}{t_{ox} \cdot \rho_{SiO_2}} \int_{\Delta\Omega} d\Omega \int_{E_{min}}^{E_{max}} Ei_{SiO_2}(E,\theta) \cdot \Phi(E,\theta) dE \quad (8)$$

where again η is the open fraction of the collimator or the coded mask, T is the mission duration, t_{ox} and ρ_{SiO2} are the thickness (180 nm) and the density of the field oxide of SiO_2, and finally $Ei_{SiO_2}(E,\theta)$ is the average ionization dose due to a single proton of energy E and incidence angle θ, $\Phi(E,\theta)$ is the proton spectrum.

7 ESTIMATION OF THE RADIATION DAMAGE AND IMPACT ON THE LEAKAGE CURRENT

7.1 Total Ionising Dose

7.1.1 Total Ionising Dose from trapped protons

We estimated with SPENVIS the Total Ionising Dose (TID) for the LOFT radiation environment assuming as a worst case the orbit with 600 km altitude and 5° inclination, as shown in Figure 37. **The plot in Figure 37 contains the nominal value of the fluence, before applying the factor of 20 as a margin.**

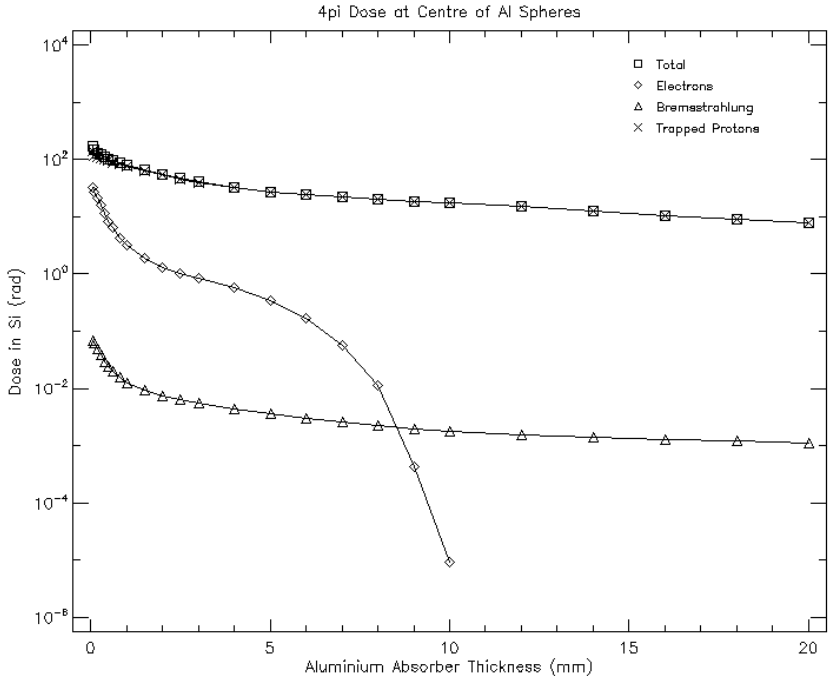

Figure 37: Total Ionizing Dose estimated for LOFT with the SHIELDOSE-2 software of the ESA SPENVIS package for the orbit at 600 km altitude and 5° inclination and the goal mission duration of five years (starting on 1 Jan 2022). The shielding effect of the materials around the SDDs is equivalent to an Al thickness of 3.3 mm for the LAD (with an acceptance angle of 4π sr) and 1.9 mm for the WFM (with an acceptance angle of 2π sr). **The plot contains the TID from the nominal fluence, before applying the factor of 20 as margin**.

Assuming the margin of a factor of 20 on the proton fluence from AP8MIN, the worst case for the TID on the SDDs is < ~2 krad(Si) for the LAD and < ~1 krad(Si) for the WFM. Considering the relevant conversion factor (1 rad(Si) = 0.58 rad(SiO_2)) from [RD-48]), this translates into < 1.16 krad(SiO_2) for the LAD and < 580 rad(SiO_2) for the WFM.
The effects produced by the TID on the SDDs are an increase of both the trapped charge in the silicon oxide layer and the interface traps (see e. g. [RD-49]). While the first effect is beneficial, since it entails an increase in the punch-through voltage between the drift cathodes, the second may determine an increase of leakage current due to surface generation.

7.1.2 Total Ionising Dose from soft protons

The TID is estimated for the soft proton component in [RD-15]. The expected values for the whole mission duration are 69 rad(SiO_2) for the LAD and 155 rad(SiO_2) for the WFM. The increase of the SDD expected leakage current due to the TID effects is negligible at this low dose values.

7.2 Expected increase of the leakage current from NIEL

7.2.1 Expected increase of the leakage current for the LAD from trapped protons

Table 12: Expected increase of the bulk leakage current of the LAD SDDs at 20° C estimated with SPENVIS with the APMIN model for a LOFT orbit of given altitude and inclination with the nominal mission duration of 4.25 years starting on 1 Jan 2022 from ([RD-2]). Φ_{AP8MIN} is the nominal fluence of 10 MeV protons from SPENVIS. **Φ_{AP8MIN} × 20, δI_{AP8MIN} and ΔI_{AP8MIN} include the margin of a factor of 20**. The overall shielding is equivalent to 3.3 mm aluminum. The anode volume is 1.53 × 10^{-2} cm^3 (970 μm pitch). These numbers do not include an average contribution from soft protons estimated in 109 pA/cm^3 (i. e. 1.7 pA/anode) at 20 °C in 4.25 years, independent of the orbit (see [RD-15]).

Altitude [km]	Inclination [°]	Φ_{AP8MIN} [cm^{-2}]	Φ_{AP8MIN} × 20 [cm^{-2}]	δI_{AP8MIN} [pA/cm^3]	ΔI_{AP8MIN} [pA/anode]
550*	0.0*	1.5 × 10^5	3.0 × 10^6	1581*	24.2*
550	2.5	1.5 × 10^5	3.0 × 10^6	1581	24.2
550	5.0	8.1 × 10^6	1.6 × 10^8	88315	1349.2
600	0.0	6.8 × 10^6	1.4 × 10^8	72454	1106.9
600	2.5	2.4 × 10^7	4.8 × 10^8	259947	3971.3
600	5.0	8.9 × 10^7	1.8 × 10^9	941987	14391.2

* the orbit at 550 km, 0.0° is below the validity range for SPENVIS. Conservatively, we adopt for this orbit the same temperature values as in 550 km, 2.5°.

7.2.2 Expected increase of the leakage current for the LAD from soft protons

For the LAD the displacement damage from soft protons produces in 4.25 years an increase of the bulk leakage of 109 pA/cm^3 at 20 °C, corresponding to 1.7 pA/anode (see [RD-15] for details). This value is obtained taking into account the narrow distribution of the soft protons and an effective exposure factor computed from the

LOFT mock observing plan, from which the fraction of time (effective exposure) in which the soft proton flux can interact with the SDDs is 6 % (see [RD-18]).

7.2.3 Total expected increase of the leakage current for the LAD

By summing the increase of the leakage current from trapped protons for the different orbits considered for LOFT, shown in Table 12, with the contribution of soft protons of 109 pA/cm^3 (i. e. 1.7 pA/anode) independent of the orbit, we obtain the numbers in

Table 13, estimated at 20° C for a mission duration of 4.25 years.

Table 13: Expected total increase of the bulk leakage current of the LAD SDDs at 20° C estimated considering the trapped protons in AP8MIN and the soft protons in [RD-15] with the nominal mission duration of 4.25 years starting on 1 Jan 2022 from ([RD-2]). Φ_{AP8MIN} is the nominal fluence from SPENVIS. **Φ_{AP8MIN} × 20, δI_{total} and ΔI_{total} include the margin of a factor of 20 on the fluence of trapped protons (AP8MIN).**

Altitude [km]	Inclination [°]	Φ_{AP8MIN} [cm^{-2}]	Φ_{AP8MIN} × 20 [cm^{-2}]	δI_{total} [pA/cm^3]	ΔI_{total} [pA/anode]
550*	0.0*	1.5×10^5	3.0×10^6	1690*	25.8*
550	2.5	1.5×10^5	3.0×10^6	1690	25.8
550	5.0	8.1×10^6	1.6×10^8	88424	1350.9
600	0.0	6.8×10^6	1.4×10^8	72563	1108.6
600	2.5	2.4×10^7	4.8×10^8	260056	3973.0
600	5.0	8.9×10^7	1.8×10^9	942096	14392.9

* the orbit at 550 km, 0.0° is below the validity range for SPENVIS. Conservatively, we adopt for this orbit the same temperature values as in 550 km, 2.5°.

7.2.4 Expected increase of the leakage current for the WFM from trapped protons

Table 14: Expected increase of the bulk leakage current of the WFM SDDs at 20° C estimated with SPENVIS with the AP8MIN model for a LOFT orbit of given altitude and inclination with the nominal mission duration of 4.25 years starting on 1 Jan 2022 ([RD-2]). Φ_{AP8MIN} is the nominal fluence of 10 MeV protons from SPENVIS. **Φ_{AP8MIN} × 20, δI_{total} and ΔI_{total} include the margin of a factor of 20 on the fluence of trapped protons (AP8MIN).** The acceptance angle for the WFM is 2π because half of the protons are blocked by the optical bench and the spacecraft. The overall shielding is equivalent to 1.7 mm Al. The anode volume is 2.28×10^{-3} cm^3 (145 μm pitch). These numbers do not include a contribution from soft protons estimated in 2578 pA/cm^3 (i. e. 5.9 pA/anode) in 4.25 years, independent of the orbit (see [RD-15]).

Altitude [km]	Inclination [°]	Φ_{AP8MIN} [cm^{-2}]	Φ_{AP8MIN} × 20 [cm^{-2}]	δI_{AP8MIN} [pA/cm^3]	ΔI_{AP8MIN} [pA/anode]
550*	0.0*	1.5×10^5	3.0×10^6	1581*	3.6*
550	2.5	1.5×10^5	3.0×10^6	1581	3.6
550	5.0	5.4×10^6	1.1×10^8	57970	132.4
600	0.0	5.1×10^6	1.0×10^8	54349	124.1
600	2.5	1.5×10^7	3.0×10^8	163030	372.3

600	5.0	6.6×10^7	1.3×10^9	706486	1613.4

* the orbit at 550 km, 0.0° is below the validity range for SPENVIS. Conservatively, we adopt for this orbit the same temperature values as in 550 km, 2.5°.

7.2.5 Expected increase of the leakage current for the WFM from soft protons

The dedicated analysis of the radiation damage from soft protons (see [RD-15] for details) gives an expected increase of the leakage current of 2578 pA/cm^3 (i. e. 5.9 pA/anode) at 20 °C in 4.25 years. Similarly to the LAD case, this value is obtained taking into account the narrow distribution of the soft protons described in [RD-18] and the LOFT pointing directions in the mock observing plan, from which the fraction of time (effective exposure) in which the soft proton flux can interact with the SDDs is 19 % (see [RD-18]) .

7.2.6 Total expected increase of the leakage current for the WFM

By summing the increase of the leakage current from trapped protons for the different orbits considered for LOFT, shown in Table 14, with the contribution of soft protons of 2578 pA/cm^3 (i. e. 5.9 pA/anode) independent of the orbit, we obtain the numbers in Table 15, estimated at 20° C for a mission duration of 4.25 years.

Table 15: Expected total increase of the bulk leakage current of the WFM SDDs at 20° C estimated considering the trapped protons in AP8MIN and the soft protons in [RD-15] with the nominal mission duration of 4.25 years starting on 1 Jan 2022 ([RD-2]). Φ_{AP8MIN} is the nominal fluence of 10 MeV protons from SPENVIS. **$\Phi_{AP8MIN} \times 20$, δI_{total} and ΔI_{total} include the margin of a factor of 20 on the fluence of trapped protons (AP8MIN).**

Altitude [km]	Inclination [°]	Φ_{AP8MIN} [cm^{-2}]	$\Phi_{AP8MIN} \times 20$ [cm^{-2}]	δI_{total} [pA/cm^3]	ΔI_{total} [pA/anode]
550*	0.0*	1.5×10^5	3.0×10^6	4159*	9.5*
550	2.5	1.5×10^5	3.0×10^6	4159	9.5
550	5.0	5.4×10^6	1.1×10^8	60548	138.3
600	0.0	5.1×10^6	1.0×10^8	56927	130.0
600	2.5	1.5×10^7	3.0×10^8	165508	378.2
600	5.0	6.6×10^7	1.3×10^9	709064	1619.3

* the orbit at 550 km, 0.0° is below the validity range for SPENVIS. Conservatively, we adopt for this orbit the same temperature values as in 550 km, 2.5°.

8 EXPERIMENTAL VERIFICATION OF THE CURRENT INCREASE

8.1 Trapped protons

We verified with two experimental measurements the increase of the SDD leakage current with the fluence, predicted in Eq (3). At the Proton Irradiation Facility (PIF) of the accelerator of the Paul Scherrer Institute (PSI) in Villigen (Switzerland) we performed two irradiations: in the first one (October 2011) we irradiated a SDD of the ALICE production with protons of 50 MeV energy, in the second one (July 2013) we

irradiated with protons of 11.2 MeV a SDD of the FBK-2 production and one of the FBK-3 production. The details of the irradiation of the ALICE SDD are also reported in [RD-21].
In all cases, we measured the leakage current of the anodes of the SDD under test using the probe station of the INFN Trieste before the irradiation. By replicating the same measurement after the irradiation, we measured the variation of the leakage current produced by the proton fluence and we compared it with the predictions from Eq. (3).
The irradiation of the FBK-2 SDD on July 2013 is devoted to the study of the variation of the Charge Collection Efficiency (CCE) with the displacement damage. The proton irradiation simultaneously increases the device leakage current, which is measured with a less sensitive method (see Sec. 8.1.2.4) than used for the FBK-3 detector. The irradiation of the FBK-3 SDD in the same day aims to measure the variation of the leakage current (see Sec. 8.1.2.5), measured with the probe station.

8.1.1 Irradiation of the ALICE SDD

The ALICE SDD has a thickness of 300 μm, a geometric area of 8.76 cm × 7.25 cm and an anode pitch of 294 μm. The drift length is 3.5 cm and is representative of the LOFT SDDs. The SDD is electrically subdivided into two independent halves: up half and down half, both with the same anode pitch. Both halves are simultaneously irradiated.

8.1.1.1 Irradiation set-up

We divided the irradiation into five steps, with increasing values of the proton fluence (see [RD-21] for more information). At the end, the delivered fluence was 2.5×10^9 p/cm^2, equivalent to ~28 times the value estimated for a mission duration of 4.25 years in orbit at 600 km altitude and 5° inclination. At the end of each step we measured the characteristic I – V curve of the SDD using a programmable electrometer Keithley 617, in order to verify the functionality of the detector and to have a rough estimation of the leakage current.

8.1.1.2 Measurement of the I – V curve

In order to assess the annealing of the damage created by the irradiation during the time period before the anode leakage currents could be measured at the INFN-Trieste laboratory, we decided to use the I – V measurements taken at PIF together with a similar measurement taken when the SDD arrived in Trieste, as shown in Figure 38.
Since all cathodes implants are connected together on the detector by means of the integrated voltage divider, the SDD can be considered as a very large diode: biasing the detector with only two probes (one on a cathode and one on the peripheral n^+ implant), it is possible to measure the total leakage current of the silicon device in the full depletion condition (60 V bias in this case). This measurement is not as precise as the measurement of the actual leakage current at the anodes because there is a larger contribution of surface generation coming from the SiO_2-Si interface, which is not possible to control when biasing the SDD in this way. Also, the leakage from the guard regions adds to the measurement, offsetting the actual anode current by about 20% (the ratio of the total geometric area of the detector to the sensitive one). Nevertheless, using this approach we can compare the leakage at various times after irradiation in a consistent way.

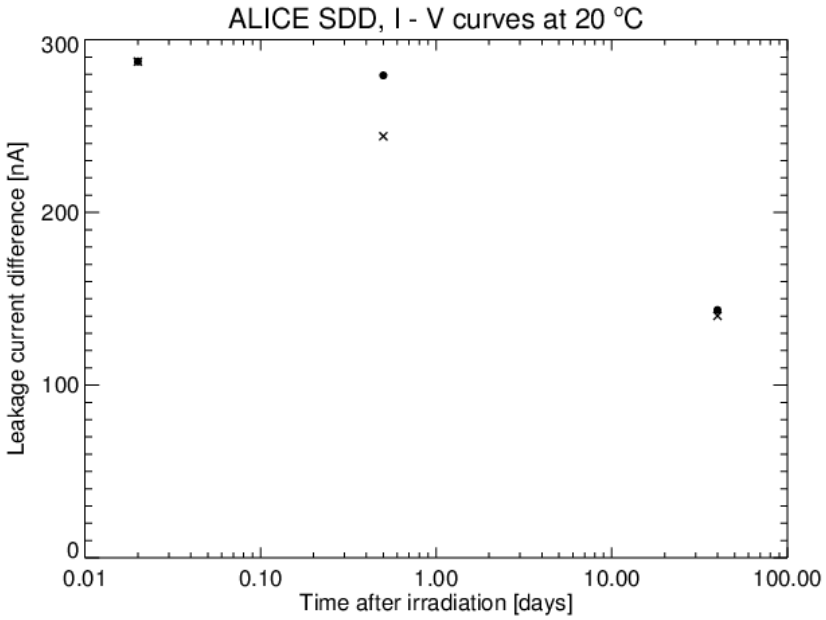

Figure 38: Difference of leakage current at a temperature of 20 °C (dots) derived from the I – V curves at different times after the end of the irradiation, compared to the values (crosses) estimating at the same time from the annealing model in [RD-19].

8.1.1.3 Measurement of the anode leakage current

We measured again ~66 days after the irradiation the leakage current of the anodes using the probe station of INFN Trieste. In Figure 39 we superimpose for the two halves of the SDD the anode leakage current before and after the irradiation. To derive the value of the anode leakage current at the end of the irradiation, we extrapolate back in time the values measured at the probe station using the results of the I(t) curve shown in Figure 38. With this method we obtain that, for a temperature of 20 °C, the measured increment is higher than the predicted value of ~32 % in the down half and ~37 % in the up half, respectively. The difference between the measured increase of the anode leakage current and the predicted one can be explained with the uncertainty related to the extrapolation based on the curve plotted in Figure 38.

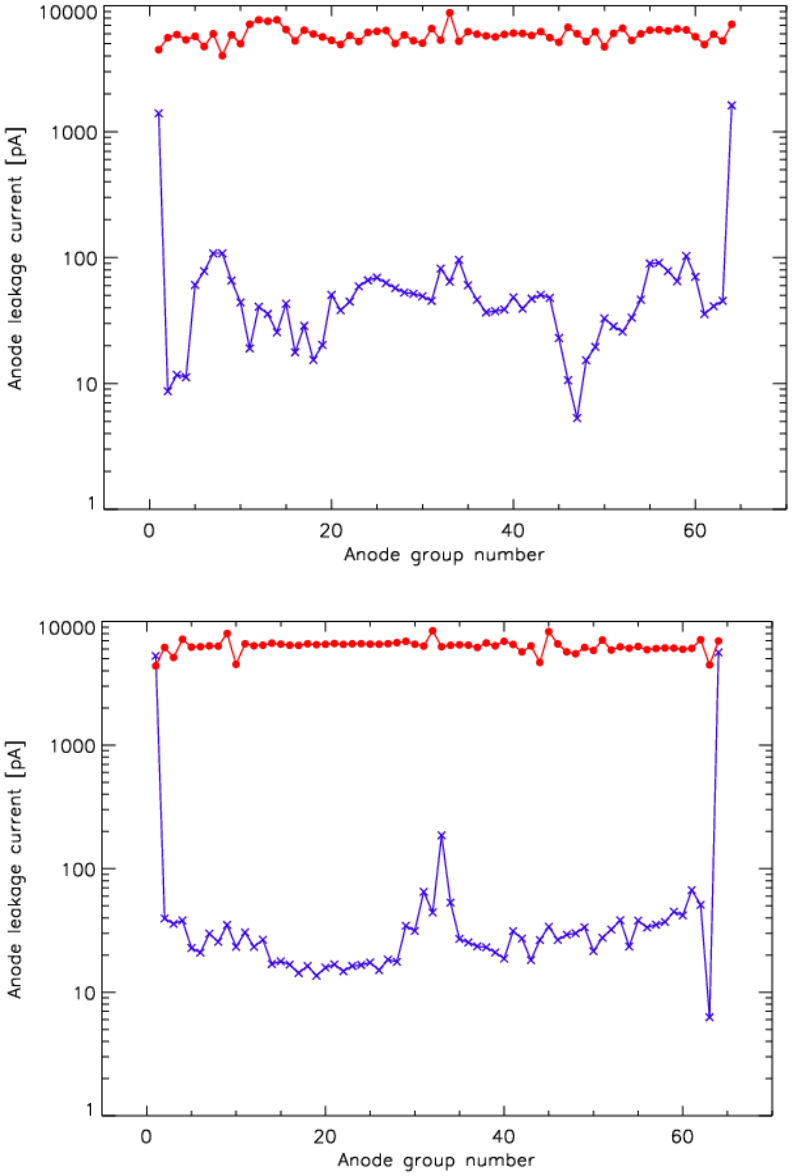

Figure 39: Anode leakage current before the irradiation (blue) and after (red) in the up (top panel) and down (bottom panel) halves of the SDD. Both measures are at the same temperature, 22 °C.

8.1.2 Irradiation of the FBK-2 and FBK-3 SDDs

Basing on the experience with the ALICE detector, we performed a second campaign at the same PSI PIF facility (July 2013). In this campaign we reduced the energy of the proton beam down to 11.2 MeV, the value nearest to the one used in SPENVIS (10 MeV). In this campaign we irradiated two SDDs: an FBK-2 with eight anodes connected to a discrete components FEE with JFETs, and a "naked" FBK-3 SDD without any FEE. In this section we discuss the increase of the leakage current measured on these two detectors.

8.1.2.1 Characteristics of the FBK-2 SDD

The FBK-2 SDD has the same thickness (450 μm) and drift length (3.5 cm) of the SDDs for LOFT. Only the geometric area is slightly smaller, 5.52 cm × 7.25 cm instead of 12.08 cm × 7.25 cm for the LAD and 7.74 cm × 7.25 cm for the WFM. The FBK-2 SDD has two different values of the anode pitch on the two halves: 833 μm for the LAD half and 294 μm for the WFM one.
The intrinsic leakage current of this SDD before the irradiation is ~0.2 nA/anode at 20 °C.
Since this SDD is irradiated to study the variation of the CCE (see Sec. 11.3), the measurement of the increase of the bulk leakage current is not the primary objective of the test and consequently it is performed with lower sensitivity than on the FBK-3 detector.

8.1.2.2 Characteristics of the FBK-3 SDD

The thickness (450 μm), drift length (3.5 cm) and geometric area (5.52 cm × 7.25 cm) of the FBK-3 SDD are the same as the FBK-2. The FBK-3 has different values of the anode pitch on the two halves: 967 μm for the LAD half and 147 μm for the WFM one.
This SDD is specifically irradiated to study the increase of the anode leakage current, consequently its current is measured before and after the irradiation with the probe station.

8.1.2.3 Irradiation set-up

For this irradiation we selected, among the values of the proton energy available at the facility, the value nearest to the equivalent energy of 10 MeV used for our estimations with SPENVIS (Sec. 7.2). With this criterion, the proton beam has a peak energy of 11.2 MeV. Since this value is obtained by degrading the proton energy with aluminum absorbers of 21 mm thickness, the Full Width at Half Maximum (FWHM) of the spectrum is ~6 MeV.
We selected for the irradiation of the FBK-3 SDD a fluence more than one order of magnitude higher than the value expected for the LAD in 4.25 years at 600 km altitude and 5° inclination (see Table 12). In order to simplify the experimental set-up, the whole fluence is provided in a single exposure, without the intermediate measurements performed during the irradiation of the ALICE SDD (see Sec. 8.1.1.2).
Since the anode leakage current of the FBK-3 could be measured with the probe station not earlier than one week after the irradiation, we increased the proton fluence to compensate the annealing of the displacement damage between the end of the irradiation and the measurement of the leakage current. Following [RD-19] and assuming a storage temperature of 21 °C and an interval of 8 days between the irradiation and the first measurement, the residual damage is 41 %. With this choice, the fluence provided to the FBK-3 SDD is 3.11×10^9 p/cm^2 and, at 8 days after the irradiation, this value corresponds to ~61 years in orbit at 600 km altitude and 5° inclination.
With this value of the fluence, the silicon oxide of the SDD receives a TID of ~1.85 krad, representative of the value for the SDD in orbit with the margin of a factor of 20 (see Sec. 7.1.1).

The fluence provided to the FBK-2 SDD is 8.9×10^8 p/cm^2 and is selected to measure the variation of the CCE, as discussed in Sec. 11.3.5.
The spatial distribution of the intensity of the proton beam is the same for FBK-2 and FBK-3. During the calibration of the beam we found that the maximum of the flux is in x ~ 2 cm and y ~ 0 cm, not in the geometric center of the beam (see Figure 40 and Figure 41). The region around the maximum is also the region with the highest flux uniformity, as shown in the map in Figure 42. For this reason, during the irradiation of both the SDDs we put the geometric center of the LAD half at x = 2 cm and y = 0 cm, where the maximum proton flux and the highest uniformity are measured.
The average fraction of the beam flux on the surface of the LAD half of the FBK-3 SDD (highlighted by the dashed black box in Figure 42) is 77.8 % of the maximum. The average fraction on the anodes of the FBK-2 connected to the FEE is 88.8 %, as shown in Figure 71 in Sec. 11.3.5.

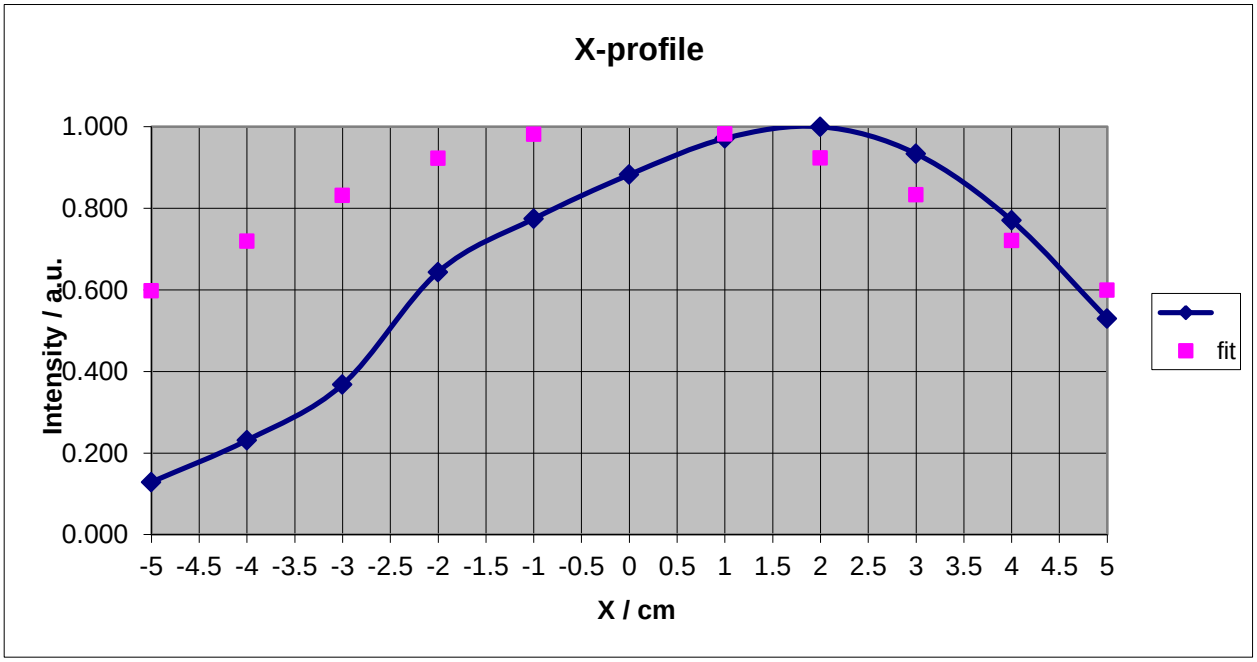

Figure 40: Intensity of the beam at different positions on the horizontal axis. Left and right are as seen from the beam direction.

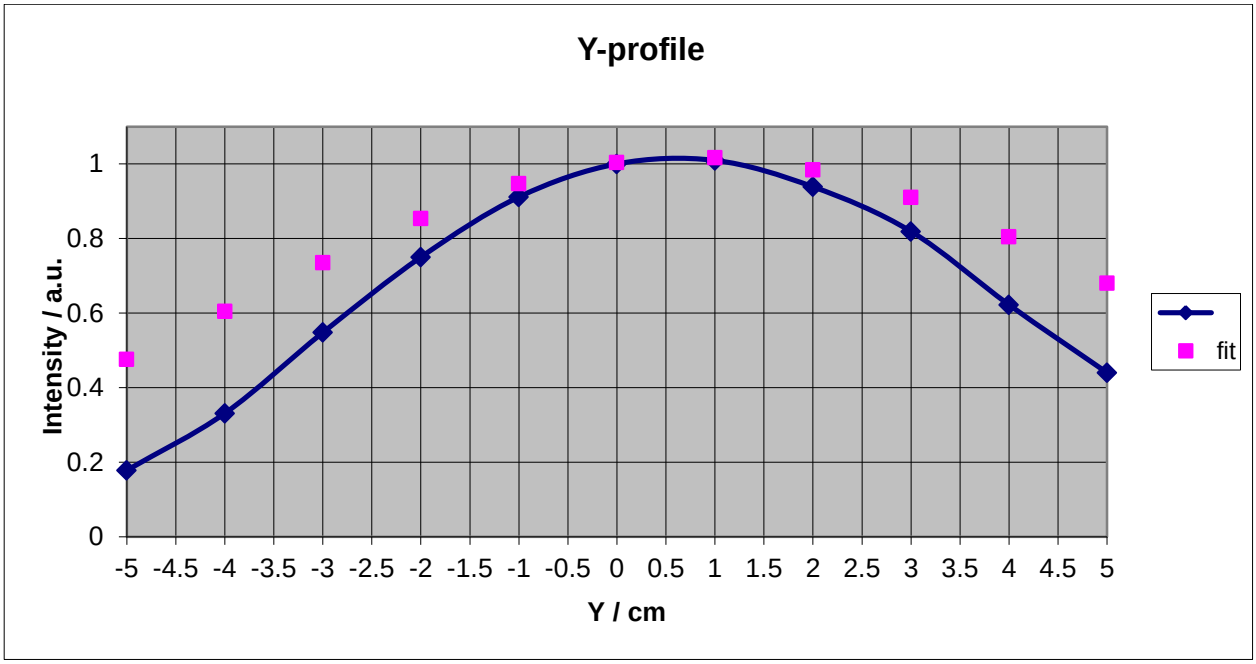

Figure 41: Intensity of the beam at different positions on the vertical axis. Up and down are reversed as seen from the beam direction.

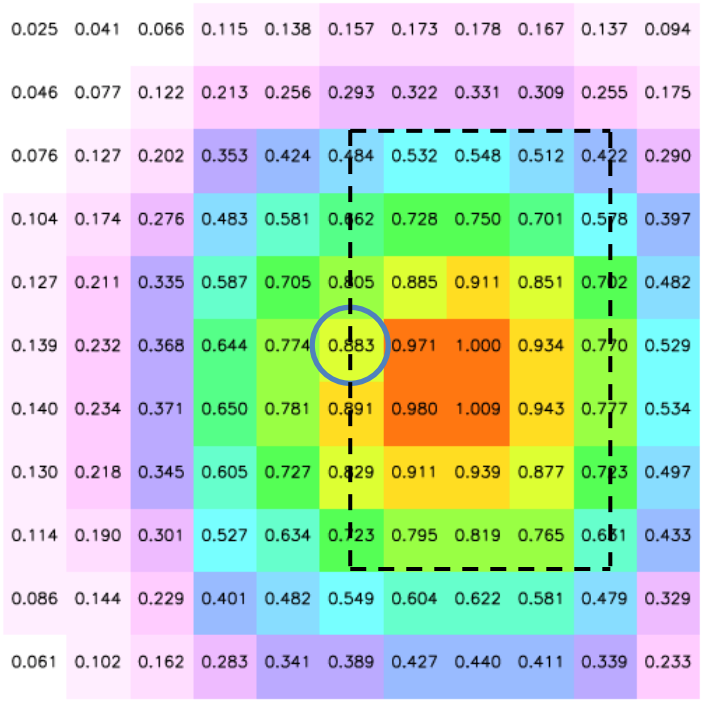

Figure 42: Map of the reconstructed beam intensity, at 1 cm step. The center of the beam is indicated by the blue circle. The x axis (left to right) is in the direction of the charge drift. The y axis (up to down) is in the direction of the readout anodes. The dashed black box defines approximately the surface of the LAD half of the FBK-3 SDD, where the average fraction of the beam intensity is 77.8 %. The average fraction of the intensity for the FBK-2 SDD is shown in Figure 71.

8.1.2.4 Measurement of the anode leakage current of the FBK-2 SDD

Independently on the variation of the CCE, the fluence of protons delivered during the irradiation increases the bulk leakage current of the SDD. As shown in the map in Figure 71, the average fraction of the beam on the surface covered by the anodes connected to the FEE is 88.8 % with respect to the maximum and the average fluence on these anodes is thus 7.9×10^8 p/cm^2.
We measured the bulk leakage current of the FBK-2 SDD on 19 July 2013, that is ~5 days after the end of the irradiation (14 July 2013 at 12:30). In 5 days between the irradiation and the measurement, the residual damage is ~44 % of the original one, consequently the residual fluence is 3.5×10^8 p/cm^2 (taking into account the fraction of the beam on the anodes). Applying the formulas in [RD-6], we find that the expected increment of the bulk leakage current after the irradiation is 2.4 nA/anode at 20 °C.
The plot of the measured leakage current as a function of temperature, compared with the value before the irradiation, is shown in Figure 58. We apply to the values of the leakage current per unit volume the same fit as in [RD-1]:

$$\frac{I}{V} = I_0 T^2 \exp(-qE_g/2\, k_B\, T) \quad (9)$$

where T is the absolute temperature, q = 1.602×10^{-19} C is the electron charge, E_g = 1.12 V is the silicon bandgap and k_B = 1.381×10^{-23} m^2 kg/s^2 is the Boltzmann constant.
We find that after the irradiation I_0 = (9.7 ± 0.1) × 10^9 pA/K^2/cm^3. This value is compared with I_0 = (6.0 ± 0.6) × 10^8 pA/K^2/cm^3 measured on the same FBK-2 SDD before the irradiation (see [RD-1]). Given the indirect method to derive the leakage current, we assume an uncertainty of 10 % on the values of I_0 from the fit.
From the fit in the Eq. (9) above, we derive that at 20 °C the leakage current after the irradiation is 2.6 nA/anode. By subtracting the value before the irradiation, 0.2 nA/anode, **we obtain a current increase of 2.4 nA/anode at 20 °C, in extremely good agreement with the expected value of 2.4 nA/anode.**
The difference between the measured and predicted values of the increase of leakage current are in the estimation of the average beam uniformity on the region of the anodes connected to the FEE and of the annealing from [RD-19].

8.1.2.5 Measurement of the anode leakage current of the FBK-3 SDD

The leakage current of the anodes on the LAD half of the FBK-3 SDD after the irradiation has been measured at the dedicated probe station of the INFN in Trieste (described in [RD-21]). The SDD has been stored at room temperature after the irradiation. The first measurement has been performed ~6.3 days after the irradiation. The variation of the leakage current rescaled to a temperature of 22 °C is shown in Figure 43. The average value of the increment in Figure 43 is 11.2 nA/anode at 22 °C, corresponding to 9.2 nA/anode at 20 °C.

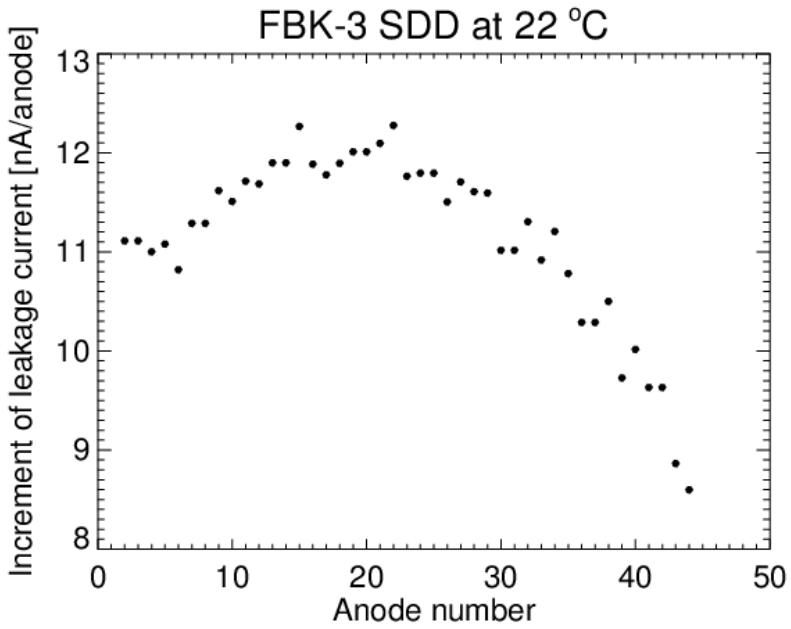

Figure 43: First measurement of the increment of the anode leakage current on the FBK-3 SDD, performed at the probe station ~6.3 days after the irradiation and rescaled to a temperature of 22 °C.

Assuming the annealing at a constant temperature of 21 °C, ~6.3 days after the irradiation the residual damage is 41.5 % of the nominal value. Consequently, the average fluence on the LAD half is 1.0×10^9 p/cm^2 considering also the average beam fraction of 77.8 %. Applying the Eq. (3) and Eq. (4) with this average fluence, the expected increase of the anode leakage current is 8.2 nA/anode at 20 °C.
The difference between the measured value and the estimated one at the same time and temperature is thus ~12 %. Similarly to the FBK-2 SDD, the difference between the measured and predicted values of the increase of leakage current are in the estimation of the annealing from [RD-19] and of the average beam uniformity on the LAD half.
The value of the leakage current measured at the anodes after the irradiation includes the contribution of both the displacement damage and TID. Since we showed above that the measured increment of leakage current is within ~12 % from the value estimated considering only the displacement damage, we derive that the increment due to the TID is negligible. Considering that the TID received by the oxide layer of the SDD during this irradiation is ~1.85 krad, representative of the value expected for the LAD in orbit with the margin of 20x on the fluence (see Sec. 7.1.1), this result confirms the insensitivity of the detectors to the radiation dose level expected in the LOFT orbit.

8.1.2.6 Annealing of the displacement damage on FBK-3

The annealing reduces the displacement damage and follows the trend in time described in literature in [RD-19] and shown in Figure 65 (in Sec. 10).
We repeated the measurement of the anode leakage current with the probe station for distances in time between ~6.3 days and ~70.9 days after the irradiation, in order to study the damage annealing. We plot in Figure 44 the variation in time of the measured increment of the leakage current and we compare it with the annealing from

[RD-19]. For this purpose, both variations are normalised to the values at ~6.3 days after the irradiation and at a temperature of 20 °C. As shown in Figure 44, the measured annealing closely follows the predictions in [RD-19].
From [RD-19], the annealing produces a variation in time of the current related damage rate α, and thus of the leakage current increase, as

$$\alpha(t) = \alpha_0 \exp(-t/\tau_1) + \alpha_1 - \alpha_2 \log(t/\tau_2) \quad (10)$$

Moreover, the time constant τ_1 is related to the temperature during the annealing,

$$\frac{1}{\tau_1} = k_0 \exp(-E/k_B T) \quad (11)$$

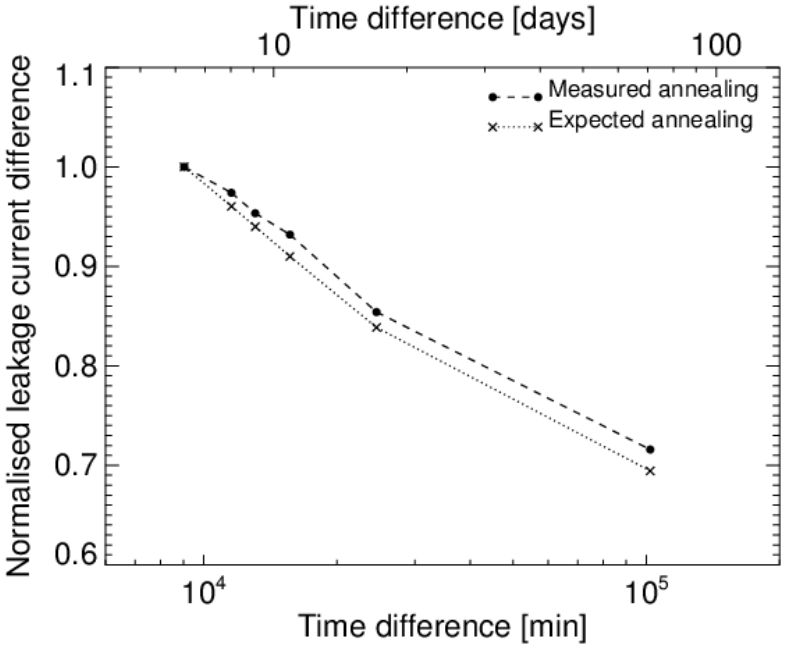

Figure 44: Annealing of the anode leakage current of the LAD half as a function of time after the irradiation.

8.2 Soft protons

8.2.1 Aim of the test

The radiative environment of LOFT in LEO contains a soft proton component of energy lower than ~1 MeV (see Sec. 4.6 and [RD-14] for details). Although some information is available in literature about the effect on silicon detectors of higher energy protons representative of the trapped component (see for example [RD-6] and [RD-19]), very little information is published about the effect of lower energy protons. Moreover, these protons are expected to release most of their energy in the superficial layers of the SDD and to be stopped inside the detector, while the energy lost by higher energy protons is distributed in the whole detector thickness.
For these reasons we irradiated two SDDs with soft protons and we measured the variation of the anode leakage current after the test. Two irradiations have been

performed for this purpose, at the Rosenau accelerator of the University of Tuebingen (in Germany). In the first one we irradiated a SDD of the FBK-2 production (on June 2012), in the second one we irradiated the same SDD used in the first campaign and one of the FBK-3 production (on December 2012).

8.2.2 The accelerator at Rosenau

Here we provide a short description of the accelerator facility used for the irradiation of the SDD with low-energy protons. More information is reported in [RD-23].
The irradiation set-up has been constructed at the accelerator facility of the Physikalisches Institut of the University of Tuebingen. The accelerator is a single ended 3 MV Van de Graaff (HVEC Model KN), that can provide light ion beams with energies ranging from ~700 keV to currently 2.3 MeV. The facility possesses six beam lines; number 3 is currently used for the irradiation setup. The beam line, including the position and opening of the slits and the position of the detector chamber, has been aligned with a theodolite. The beam can be bent and shifted in parallel with various dipole magnets and focused with two double quadrupoles. A picture of a SDD in the experimental chamber of the accelerator is shown in Figure 48.
Thin metal foils with some micrometer thickness degrade and broaden the beam energy and widen the beam spatially. The energetic and spatial broadening is due to straggling. Four different foils can be fixed on a holder. The holder itself is mounted on a linear manipulator to allow a quick change of the foil without breaking the vacuum, e. g. for an irradiation with different energies, or to compose a spectrum similar to the in-orbit spectrum. An example of the beam profile measured at the surface of the device under test, used for the LOFT SDD tests, is plotted in Figure 45 and shows a high degree of uniformity on the whole sensor surface. In this case the 2.3 MeV proton beam was degraded by a 18 μm copper foil, and the average output energy was found to be 838 ± 52 keV. Beam profile and energy were measured with calibrated silicon surface barrier (SSB) detectors, as shown [RD-23].

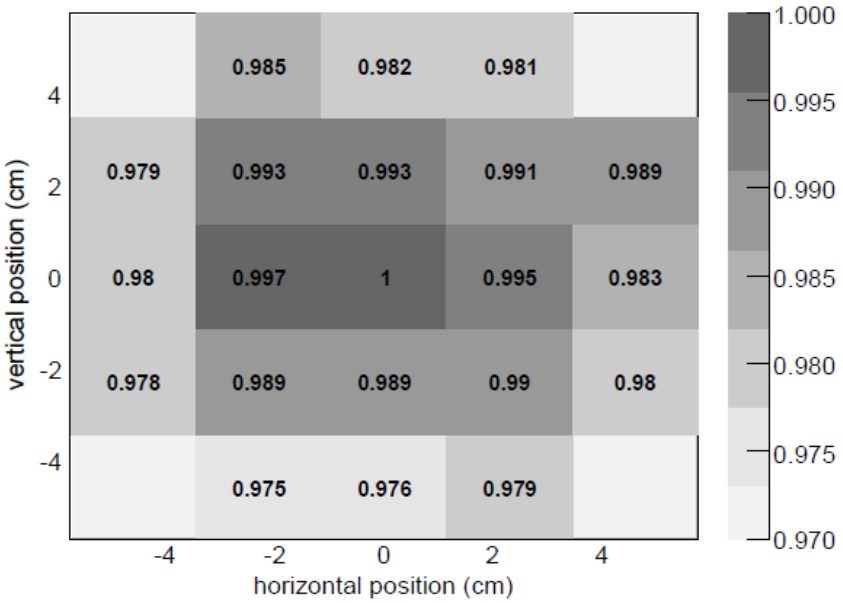

Figure 45: Map of the measured flux homogeneity during the irradiation for LOFT with ~840 keV protons (obtained with a 2.3 MeV beam and an 18 μm Cu foil).

Several combinations of rotary vane pumps and turbomolecular pumps are distributed along the beam line to reach a pressure in the 10^{-6} mbar regime. This low pressure is especially necessary to avoid coating of the degrader foils with carbon during long duration irradiations, as the residual gas contains a certain amount of hydrocarbons.

8.2.3 Irradiation set-up

The reproduction of the spectrum of the orbital soft proton flux [RD-14] at an accelerator facility is not practical because it would require too many irradiation steps with different configurations (beam energy, degrader foils of different thicknesses and/or materials). Also monitoring the test conditions and the data analysis would become too complicated. To overcome these difficulties, for the first irradiation test of June 2012 we chose a different strategy: using just two beam energies, as explained in [RD-15], we could reproduce both the mission TID and NIEL levels on the LOFT prototype SDD. This can be done because the ratio between TID and NIEL depends on the proton energy, thus any damage level can be obtained simply adjusting the proton fluence at the two chosen energies. Figure 46 and Figure 47 show that TID (in Figure 46) is highest at the low end of the energy range while for the WFM the displacement damage spectrum (see Figure 47) is almost flat up to about 1 MeV: from this we chose 200 keV and 800 keV as proton energies for the test.

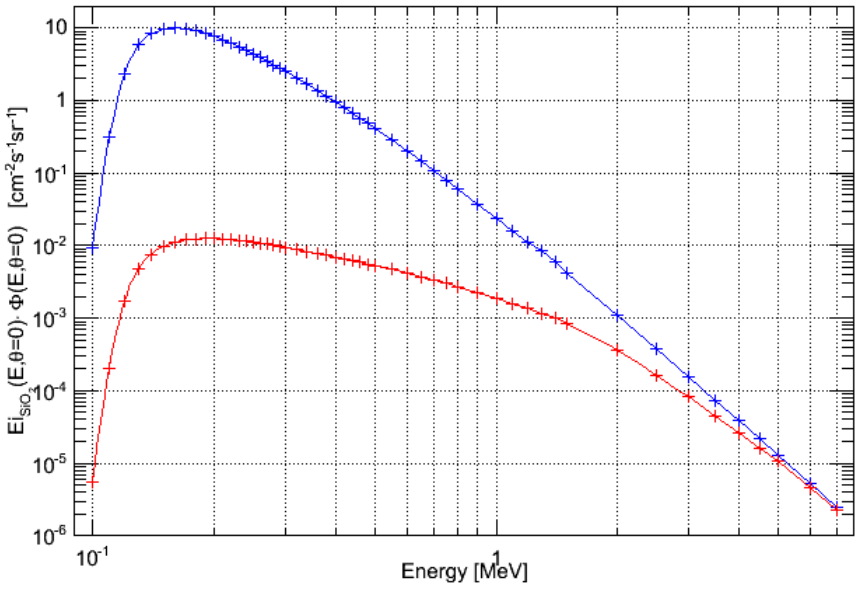

Figure 46: Differential spectrum of the soft proton ionization dose, $E_{SiO2}(E)\cdot\Phi(E)$, from [RD-15]. The blue line is for the LAD, the red line for the WFM.

Using the levels for TID and NIEL predicted for a 5 year mission in the worst case condition that the two detectors are always directed towards the flux maximum, and the tabulated values of the ionization energy and effective hardness factor (see [RD-15] for details), we calculated, for the first campaign, the steps in Table 16.

Table 16: Planned fluence steps for the first irradiation campaign.

Step	Φ_{200keV} [cm^{-2}]	Φ_{800keV} [cm^{-2}]
1	3.50×10^6	7.85×10^5
2	3.50×10^6	7.85×10^5
3	---	2.40×10^7
4	1.10×10^5	4.28×10^7
Total	7.11×10^6	6.84×10^7

In step 1 the SDD are irradiated up to half of the LAD levels, while in the following step the full LAD exposure is reached. Step 3 provided full WFM ionization dose and 80% of WFM displacement damage, while in the last step the SDD was irradiated to twice the TID and NIEL levels expected on the WFM.

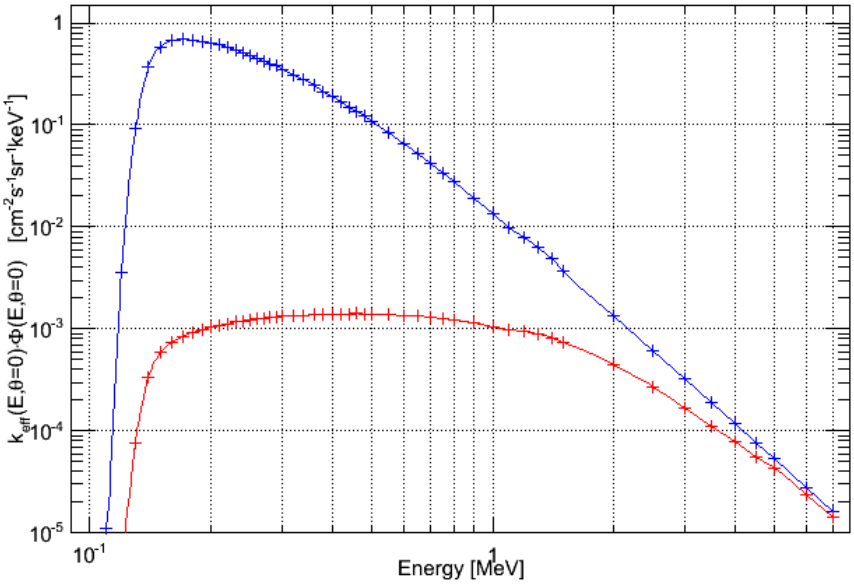

Figure 47: Differential spectrum of the soft proton displacement damage, $k_{eff}(E)\cdot\Phi(E)$, from [RD-15]. The blue line is for the LAD, the red line for the WFM.

Due to the ambiguous displacement damage results of the first test (in Sec. 8.2.4), we decided to make a second test session in December 2012. To simplify the subsequent analysis we irradiated two SDDs with single exposures with the 800 keV configuration for a total fluence of 3.59×10^8 cm^{-2}, corresponding to 10x the 5 year prediction for the WFM (5.2x the expected WFM TID). To reduce the damage annealing as much as possible, the SDDs were kept stored in a container at -18 °C as soon as the irradiation ended, and they were brought back at room temperature only about one hour before measurement in Trieste.

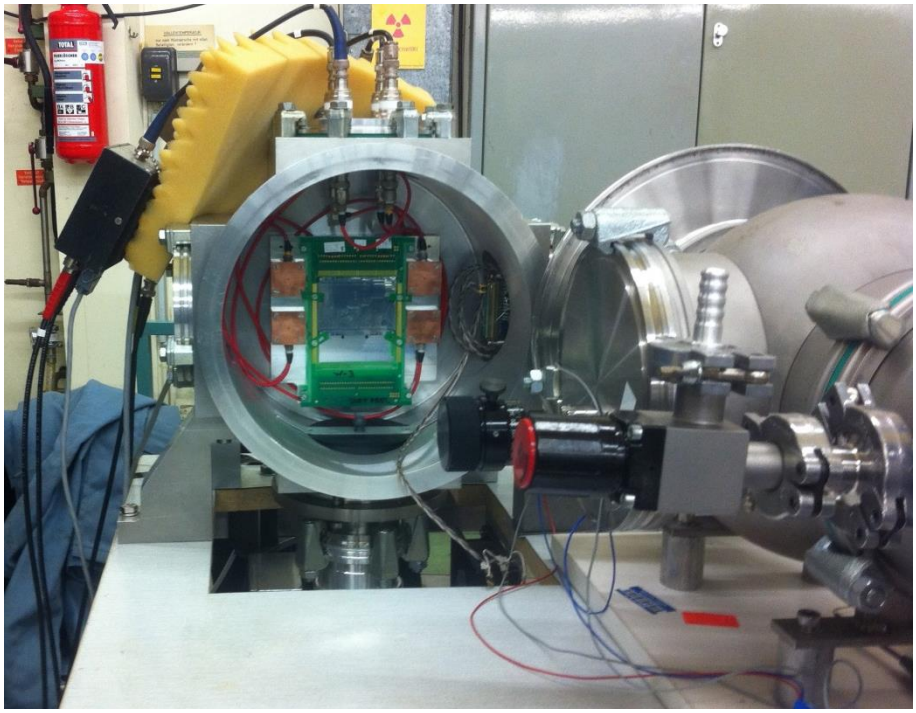

Figure 48: Picture of a SDD in the experimental chamber of the Rosenau accelerator.

8.2.4 Results

The holes created by ionization of the field oxide can displace hydrogen atoms at the SiO_2-Si interface producing dangling silicon bonds, which introduce energy states within the bandgap of the semiconductor. When the depletion region of the sensor includes these atoms with dangling bonds, the corresponding energy states become centers of thermal generation of the so called surface leakage current. The amount of depletion at the surface is governed by the electric field present in the region and is modulated by the oxide charge. TID contributes to the surface leakage current both increasing the density of the energy states in the bandgap, and changing the oxide charge.
To measure the total dose effects on the surface leakage current, we took advantage of some test structures built in the four non-sensitive triangles around the active volume of the SDDs. These structures consist of gated diodes with 1 mm^2 area and allow the determination of the surface current generation by measuring the current step that is produced when its gate bias changes the state of the underneath semiconductor region from strong inversion to depletion. Figure 49 presents a schematic description of half of a round gated diode (the actual diode implementation is rectangular). The diode junction, biased at a fixed potential, is located at the interface between the p^+ implant and the n^- bulk in the center of the structure, and it is surrounded by a gate biased at a sweeping voltage V_g.

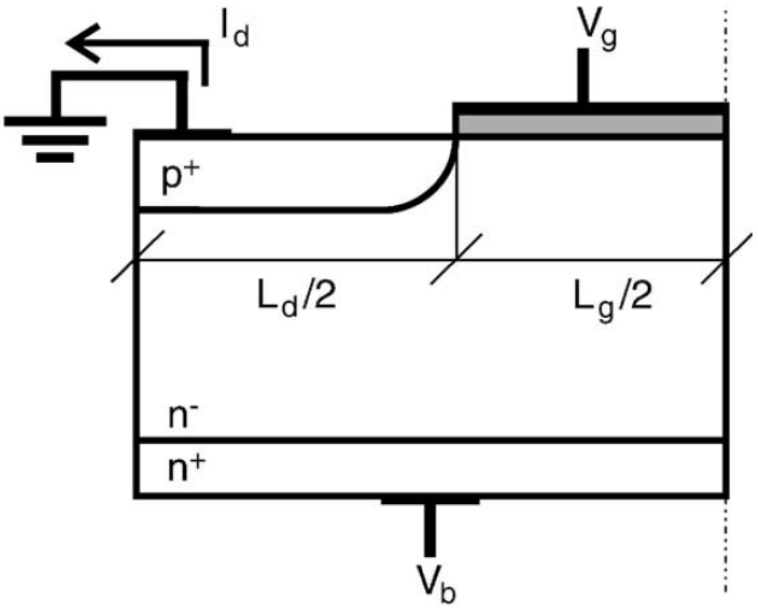

Figure 49: Example structure of a gated diode. The depletion region around the p^+ implant is modulated by the gate biasing voltage, V_g.

With respect to the planned values for the first campaign, shown in Table 16, the actual energies and fluences measured during the irradiation session are reported in Table 17.

Table 17: Measured fluences in the June 2012 irradiation campaign. The effective proton energies were measured to be 300 ± 33 keV and 838 ± 52 keV.

Step	Φ_{300keV} [cm^{-2}]	Φ_{838keV} [cm^{-2}]
1	3.38×10^6	9.53×10^5
2	3.44×10^6	6.51×10^5
3	---	2.24×10^7
4	1.36×10^5	4.34×10^7
Total	6.96×10^6	6.74×10^7

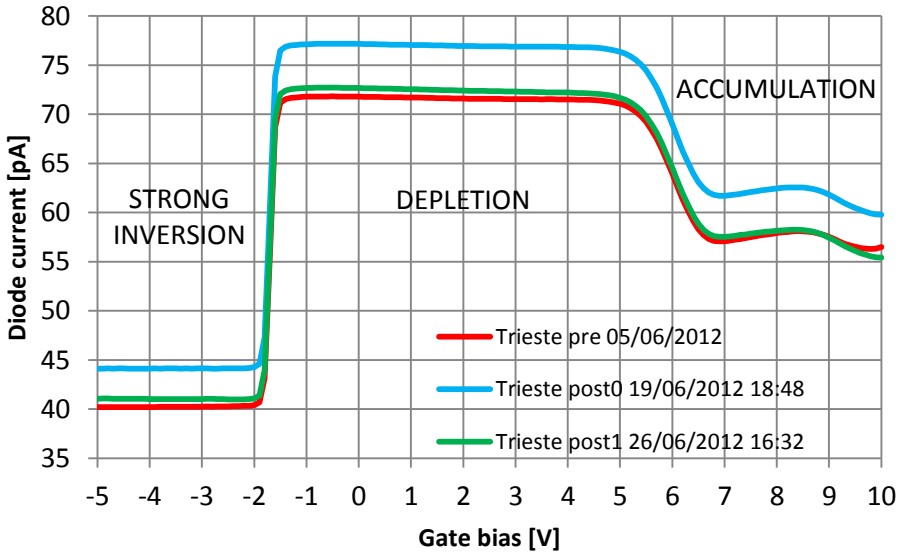

Figure 50: Gate diode current as a function of the gate voltage. The surface current is determined by the amplitude of the step at the left.

To make a meaningful test, the bias of the gate during irradiation was kept at a 5 V, a potential greater than the voltage difference between two drift cathodes in the SDD. In this way we slightly suppressed electron-hole recombination, with respect to that on the SDD field oxide, so to produce a larger effect than that expected in LOFT. Figure 50 reports the current measurements on one of the gated diodes present in the SDD irradiated in the June 2012 test session. The three data sets show the diode currents before irradiation (red curve), 5 days after irradiation (blue curve) and 12 days after irradiation (green curve). The surface current in the first measurement after irradiation was higher than before by only 1.3 pA (about 4%). In the last measurement, 12 days after irradiation, the diode curve annealed almost completely.
The curves plotted in Figure 51 show the (noisy) measurements made after each irradiation step at the accelerator facility. The maximum step in diode current is only 19 pA (~ 60%) larger than the pre-irradiation value, even after a TID equivalent to more than 10 times the expected dose for the WFM (considering the effective exposure, calculated from the LOFT mock up observing plan, see section 7.2.5). Compatible results were obtained in the December 2012 test, but this time the gated diodes were not measured just after irradiation.

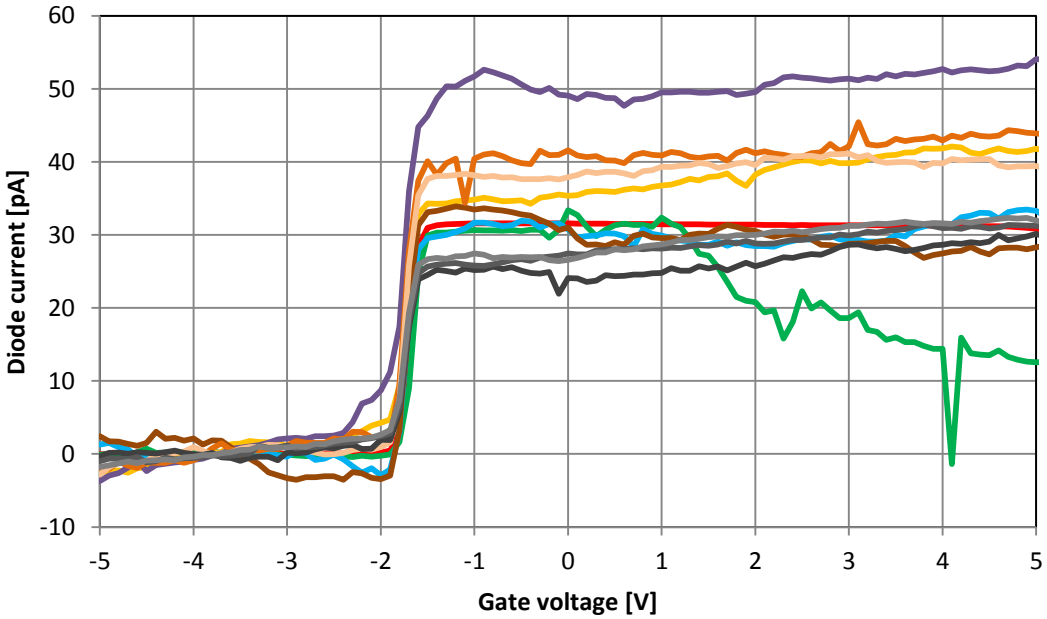

Figure 51: Diode measurements at the Rosenau accelerator after each irradiation step. The curves are normalized to show as clearly as possible the current step between strong inversion and depletion. The largest increase in surface leakage current is about 19 pA (~ 60%).

The surface current measured in the gated diode is collected from the whole gate area. This is not representative of the real SDD configuration in the gap between the drift electrodes, where the surface current comes only from the border of the cathode implants. The sensor surface current, thus, is only a small fraction of the value that can be computed considering the ratio between the area of the gate in the gated diode and the total area of the cathode gaps corresponding to each SDD anode.
The second aspect of TID effects, namely the change in oxide charge, which modulates the depletion around the implants, has been investigated with the irradiation session of December 2012. In this case we used other test structures built in the non-sensitive corners of each SDD: the MOS diodes. The capacitance measurements of these diodes, as a function of bias voltage, allow the determination of the oxide charge density. Also in this case the MOS bias was set to 5 V with respect to the grounded guard surrounding it. The results are shown in Figure 52 where the calculated charge densities (Nf) are also displayed. After irradiation the oxide charge increases: the maximum measured change in Nf is ~ 5%, small when compared to the oxide process variation within the SDD (~ 13%). This implies that there will not be large variations in depletion of the silicon surface within the gap between the drift cathodes. In any case the increase in Nf will somehow reduce depletion around the implants in such a way that the higher surface generation will be partially compensated.

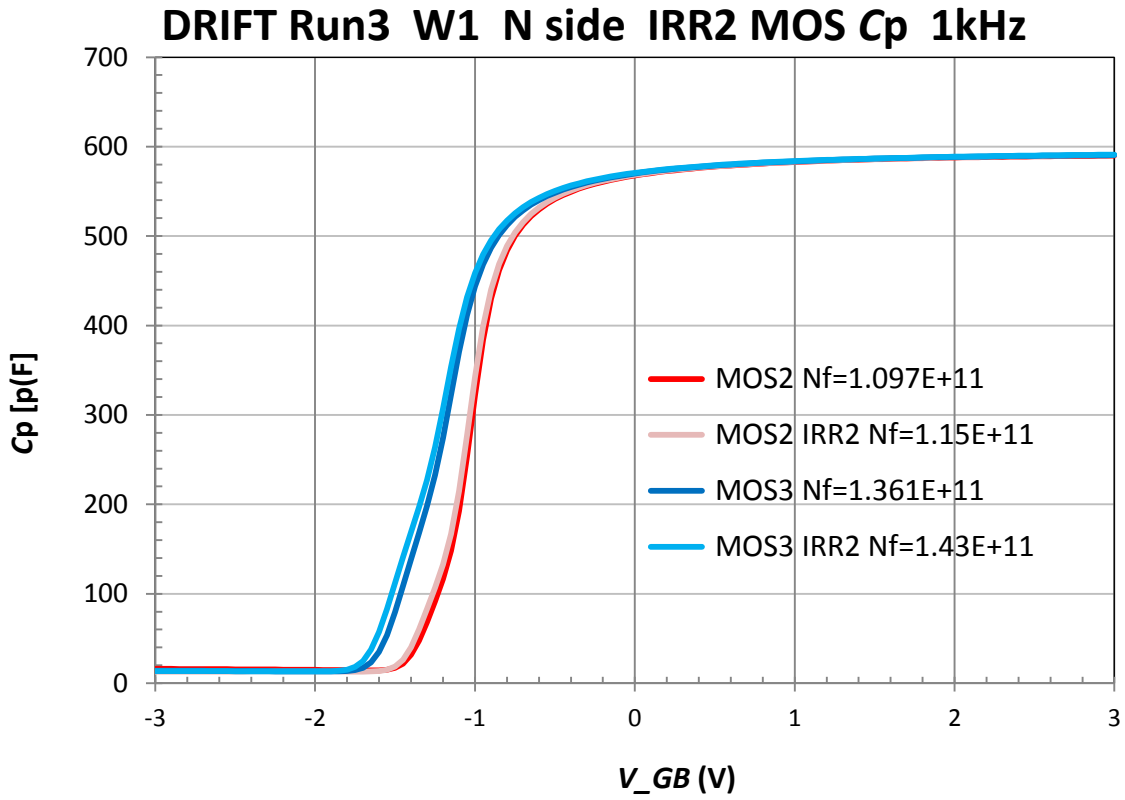

Figure 52: MOS diode capacitance measurement curves, before and after irradiation, allow the determination of the oxide charge density (Nf).

Since by design, confirmed by laboratory measurements, the surface component of the anode leakage current of a non-irradiated SDD is already negligible with respect to the bulk current, we conclude that TID effects will be of no concern for LOFT.

The main purpose of the two irradiation tests was to verify the predictions about the displacement damage in the bulk of the SDDs. In both sessions the SDD leakage currents were not measured at the accelerator facility. Measurements were carried out only after the sensor returned to INFN in Trieste.

The SDD prototype we irradiated was from the FBK-2 production. The values of the anode pitch are different on the two half detectors: the one measured has a pitch of 294 μm (the ALICE value), while the other has a pitch of 833 μm (of the same order of the LAD sensors).

From the values shown in Table 17, we calculate an expected increase of leakage current on the FBK-2 anodes of 151 pA/anode before annealing. Unfortunately, due to the unavailability of the measurement equipment, the SDD could be measured only 24 days after irradiation. The current increments, measured on groups of four anodes, are shown in Figure 53. The leakage current increased, on average, by 12 pA/anode. Considering the annealing, following [RD-19], at the storage temperature in the INFN laboratory (23 °C) the displacement damage was predicted to produce a current increase of 47.2 pA/anode, thus the measured current is only 25.4% of the expected value.

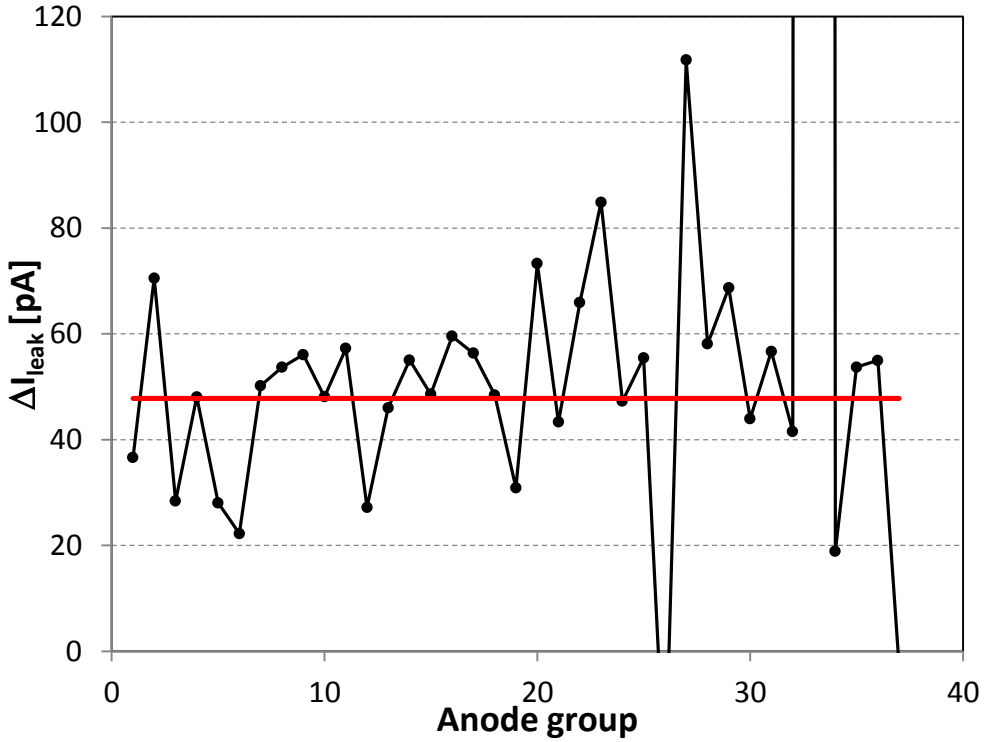

Figure 53: Increase of leakage current of groups of four anodes each, at 20 °C, measured in the XDXL-1 sensor 24 days after irradiation in the June 2012 campaign. The average increase of leakage current is 12 pA/anode.

Since the SDD was sent to INFN by express courier in a non-controlled temperature environment, we suspected that an enhanced annealing took place during the journey from Tubingen to Trieste. As an alternative hypothesis, although not realistic, damage annealing could proceed in an unexpected way. To investigate the matter we planned a new irradiation test of two SDD prototypes from different FBK runs: the same FBK-2 already irradiated in June, and an FBK-3 sensor. The new test took place in December 2012 at the same accelerator facility. In this case, to minimize the annealing before measurement the SDDs were irradiated in single steps with 838 ± 53 keV protons, and were put in a refrigerated container at -18 °C immediately afterwards. The FBK-2 detector was exposed to a proton fluence of 3.73×10^8 cm^{-2}, while the FBK-3 SDD was irradiated up to 3.62×10^8 cm^{-2}.
Measurements, at INFN, were performed repeatedly to monitor the progress of damage annealing, shown in Figure 54. The curves represent the ratio of the measured currents to the predicted ones based on the irradiation parameters in [RD-19] at 23 °C. The agreement with the annealing model is rather good, as seen by the flatness of the curves, but also in this case the measured currents are smaller than the prediction using the NIEL scaling hypothesis of the displacement damage. This is not the first evidence of lower damage in low energy proton irradiations. In [RD-20] the measured leakage current increase is about half of the predicted value at energies between 7 MeV and 10 MeV. Even if at 10 MeV our results on the SDD agree with the NIEL scaling hypothesis (as shown in Sec. 8.1.2.4 and 8.1.2.5), at energies where the orbital soft proton flux is highest the displacement damage seems to be quite small.

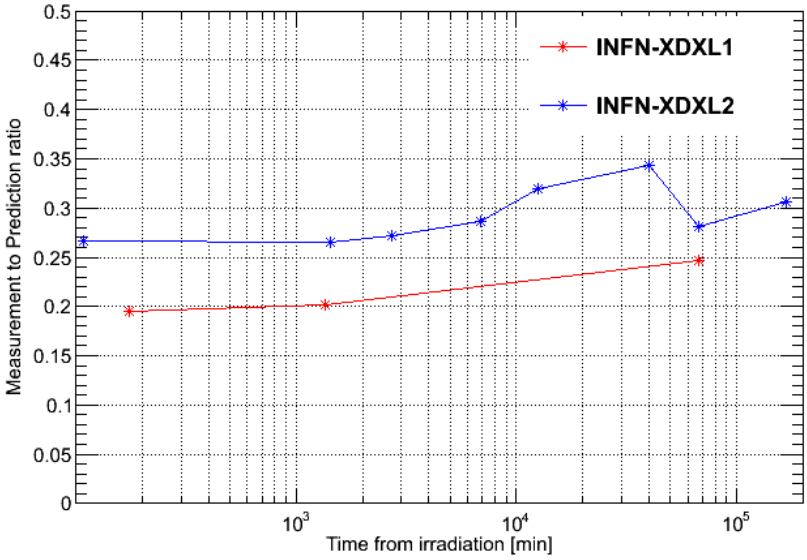

Figure 54: Damage annealing of the FBK-2 (red line, XDXL1 in the plot) and FBK-3 (blue line, XDXL2 in the plot) after the irradiation on December 2012. The curves show the ratio between the measured and the predicted NIEL leakage currents.

8.2.5 Implications for LOFT

The damage caused by the low energy protons is an important source of degradation of the SDDs performance in low altitude orbits. Our experimental results show that the increase in the sensor leakage current due to the soft protons could become of the same order of magnitude of that produced by the trapped protons at an altitude of 550 km. In the estimation of the operating conditions of the detectors (temperature) we conservatively assume the validity of the NIEL scaling hypothesis, known to overestimate the damage.

9 OPERATIVE TEMPERATURE RANGES

9.1 Variation of the leakage current with temperature

As specified in Sec. 3 above, the leakage current is the most important contribution to the overall noise of the SDDs. The leakage current, being mainly due to the thermal generation of electron-hole pairs inside the depleted silicon bulk, has the exponential temperature dependence given in Eq. (9) in Sec. 8.1.2.4 (see also [RD-5]). From Eq. (9), the leakage current approximately shows a variation of a factor of ~2 for a temperature variation of ~7 °C, and the resulting behaviour can be approximated as

$$I(T) \sim 2^{\Delta T/7℃} \qquad (12)$$

see also [RD-1].
We measured the variation of the SDD leakage current with temperature in the climatic chamber of the laboratory of INAF IAPS in Roma. For the measurement we used the discrete-electronics setup with a readout of 8 channel, as described in [RD-24] and [RD-27]. Each individual anode is read-out by an Amptek A250 charge-sensitive preamplifier, with an input SF-51 JFET. The preamplifier output is then fed to a NIM

CAEN N568B spectroscopic amplifier. Data acquisition is performed by means of a VME CAEN V785 ADC. The detector temperature was monitored by means of an AD590 temperature sensor, sensitive in the range -55 °C to +150 °C, inside the detector box, in thermal contact with the SDD. The leakage current is determined through the measure of the reset rate of a 50 fF feedback capacitor connected to the JFET input of the charge-sensitive preamplifier.
The results are shown in Figure 55 and fitted with the exponential temperature dependence given in Eq. (9) (Sec. 8.1.2.4). In our architecture, the output ramps of all preamplifiers are compared with a certain threshold, and the first comparator that fires starts the reset phase, discharging the feedback capacitor. The frequency of the reset signal can therefore be used to monitor the largest of the leakage currents at the anodes, that are however very uniform between them as shown by the detector preliminary characterizations.

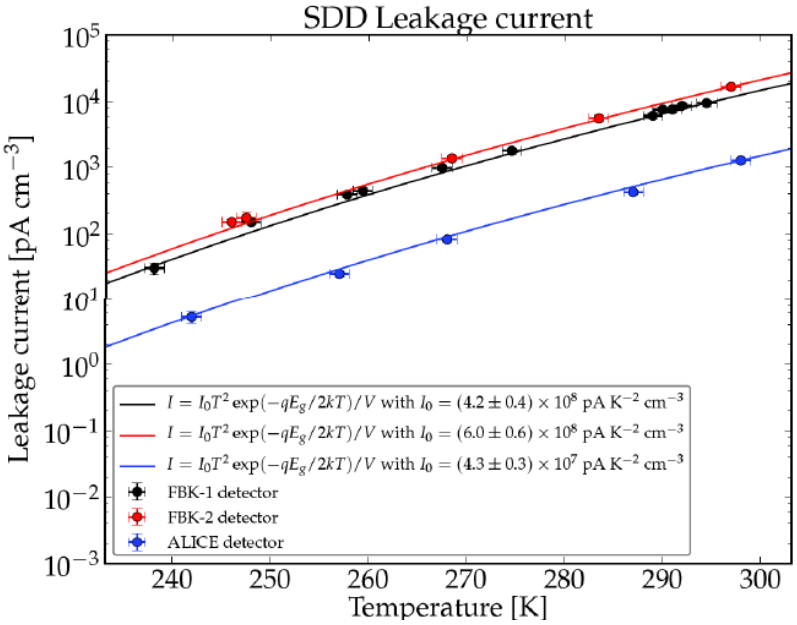

Figure 55: Variation of the bulk leakage current with temperature, measured on different prototypes (ALICE, FBK-1 and FBK-2), from [RD-1]. The FBK-1 and FBK-2 prototypes were manufactured starting from a silicon substrate with a known higher leakage current (see [RD-1] for details).

9.2 Variation of the leakage current after the irradiation

It is shown in literature that the leakage current produced by the displacement damage shows the same variation as a function of temperature as the intrinsic leakage current of a device. As an example, we show in Figure 56 the variation measured in [RD-25] and in Figure 57 the trend published in [RD-26].

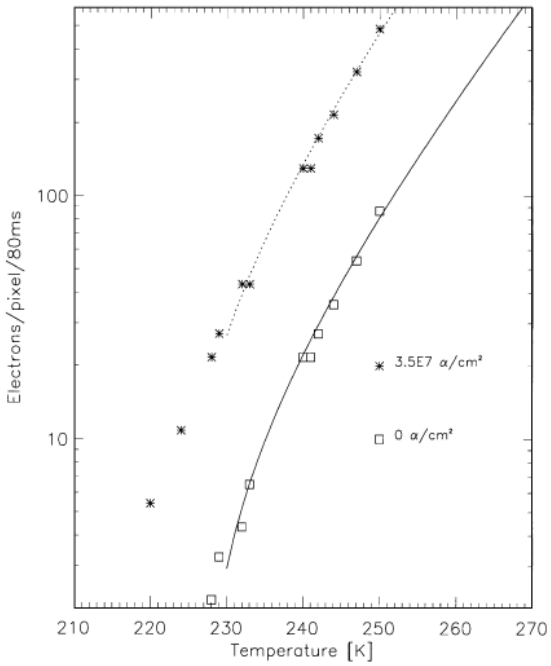

Figure 56: Variation of the leakage current with temperature after the irradiation, from [RD-25]

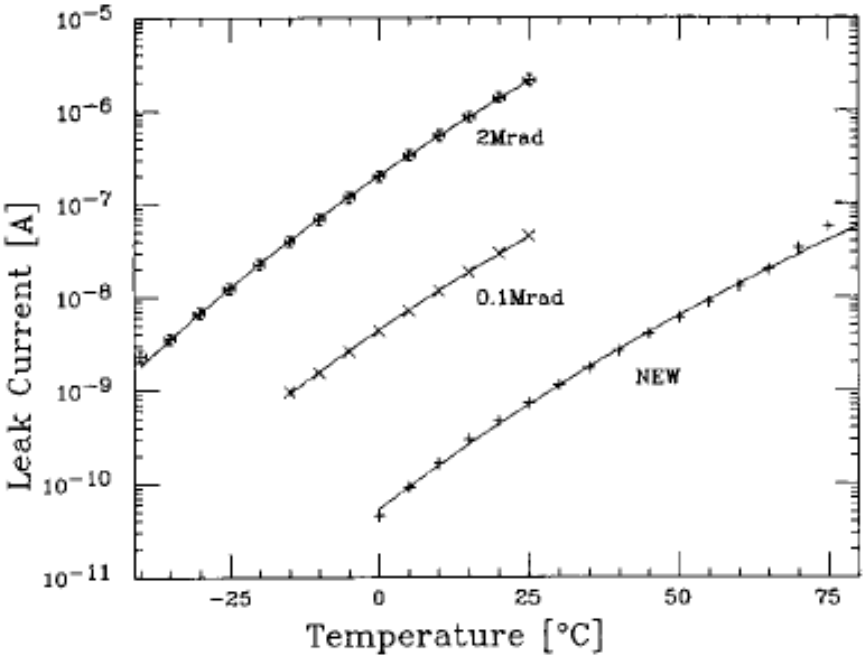

Figure 57: Variation of the leakage current with temperature after the irradiation (from [RD-26])

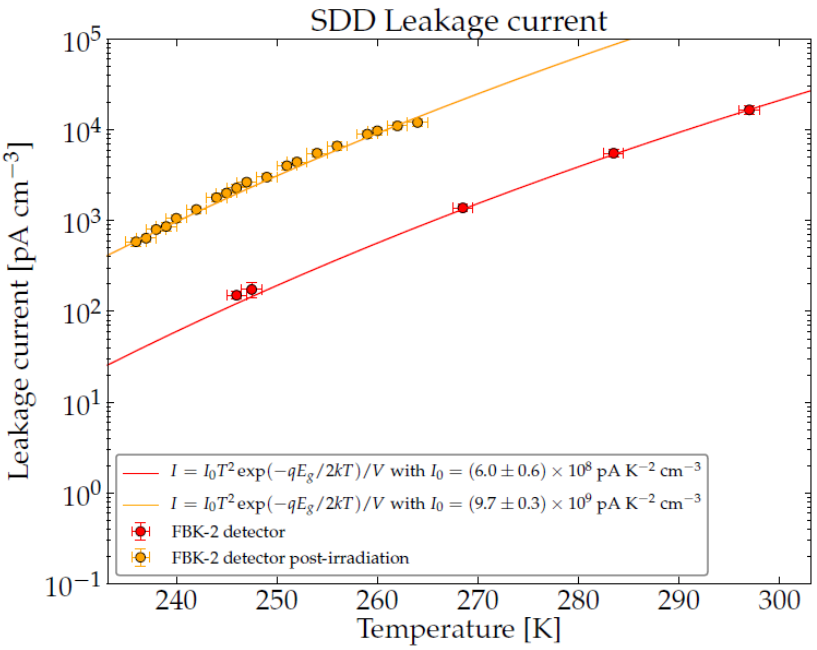

Figure 58: Measurement of the total leakage current of the FBK-2 SDD after the irradiation (orange curve) compared with the value before the irradiation (red curve).

The FBK-2 SDD irradiated at PSI PIF to study the variation of the CCE is the same detector used to measure the leakage current as a function of temperature shown in Figure 55. We show in Figure 58 the variation of the leakage current measured on this SDD as a function of temperature before and after the irradiation. It is clearly seen in Figure 58 that, after the irradiation, the leakage current follows the same trend with temperature as before the irradiation.

9.3 Operative temperature range of the LAD

Assuming the variation of current with temperature shown in Eq. (9), we plan to reduce the operative temperature of the LOFT SDDs in order to mitigate the NIEL and fulfill the requirements on the maximum value of the leakage current for the LAD (see Table 4) and WFM (see

Table 5).
We show in Table 18 the operative temperature to fulfill the requirement on the nominal spectral resolution of the LAD. The operative temperature as a function of the mission duration is shown in (3x the fluence, ESA requirement for the environment), Figure 60 (6x the fluence, design margin on the requirement) and Figure 61 (20x the fluence (additional margin for the baseline operative temperature).

Table 18: Maximum operative temperature of the LAD in order to fulfill the requirement of the nominal energy resolution: FWHM < 200 eV on one anode after 4.25 years in orbit. In the table, $T_{fluence*3}$ is obtained with 3x the fluence (ESA requirement for the environment), $T_{fluence*6}$ with 6x the fluence (design margin on the requirement) and finally $T_{fluence*20}$ with 20x the fluence (additional margin for the baseline operative temperature).

Altitude [km]	Inclination [°]	$T_{fluence*3}$ [°C]	$T_{fluence*6}$ [°C]	$T_{fluence*20}$ [°C]
550	0.0	-8*	-8*	-10*
550	2.5	-8	-8	-10
550	5.0	-22	-27	-35
600	0.0	-21	-25	-34
600	2.5	-30	-35	-43
600	5.0	-39	-44	-52

*the orbit at 550 km, 0.0° is below the validity range for SPENVIS. Conservatively, we adopt for this orbit the same temperature values as in 550 km, 2.5°.

Similarly, we show in
Table 19 the operative temperature to meet the requirement on the degrade spectral resolution for the LAD. The operative temperature as a function of the mission duration is shown in Figure 62 (3x the fluence, ESA requirement for the environment), Figure 63 (6x the fluence, design margin on the requirement) and Figure 64 (20x the fluence, additional margin for the baseline operative temperature).

Table 19: Degraded energy resolution FWHM < 400 eV on two anodes after 4.25 years in orbit. In the table, $T_{fluence*3}$ is obtained with 3x the fluence (ESA requirement for the environment), $T_{fluence*6}$ with 6x the fluence (design margin on the requirement) and finally $T_{fluence*20}$ with 20x the fluence (additional margin for the baseline operative temperature).

Altitude [km]	Inclination [°]	$T_{fluence*3}$ [°C]	$T_{fluence*6}$ [°C]	$T_{fluence*20}$ [°C]
550	0.0	+16*	+16*	+11*
550	2.5	+16	+16	+11
550	5.0	0	-6	-18
600	0.0	+1	-4	-16
600	2.5	-9	-15	-27
600	5.0	-20	-26	-37

*the orbit at 550 km, 0.0° is below the validity range for SPENVIS. Conservatively, we adopt for this orbit the same temperature values as in 550 km, 2.5°.

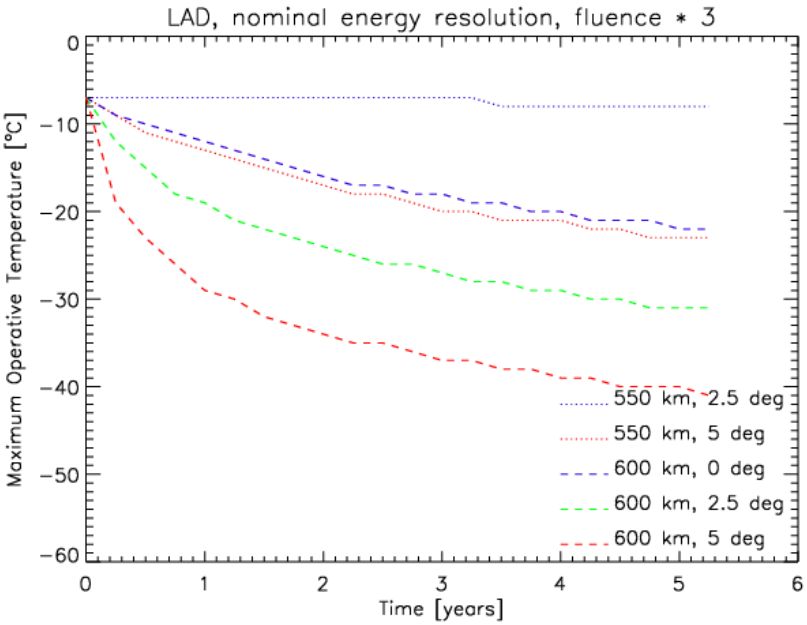

Figure 59: Maximum operative temperature of the LAD as a function of time for the nominal spectral resolution and assuming 3x the fluence (ESA requirement for the environment).

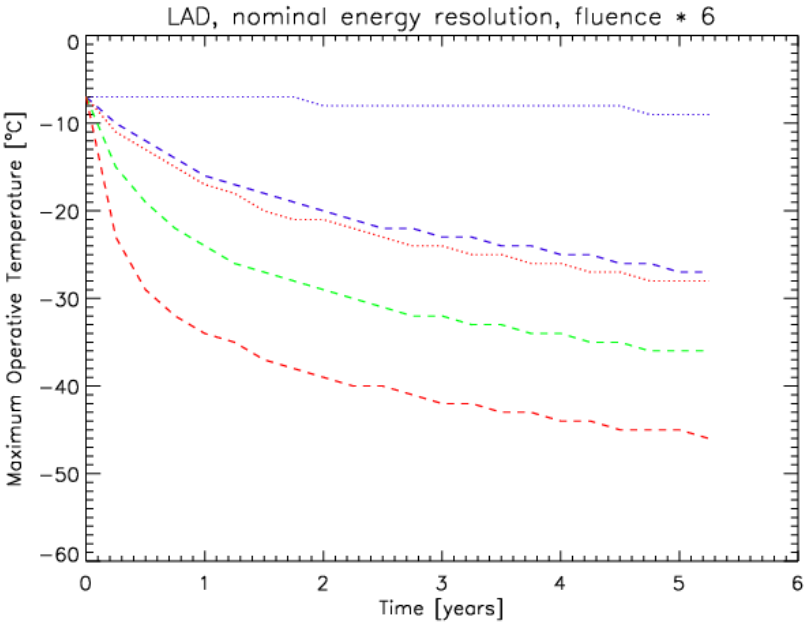

Figure 60: Maximum operative temperature of the LAD as a function of time for the nominal spectral resolution and assuming 6x the fluence (design margin on the requirement). The color and linestyle code of the orbits is the same as in Figure 59.

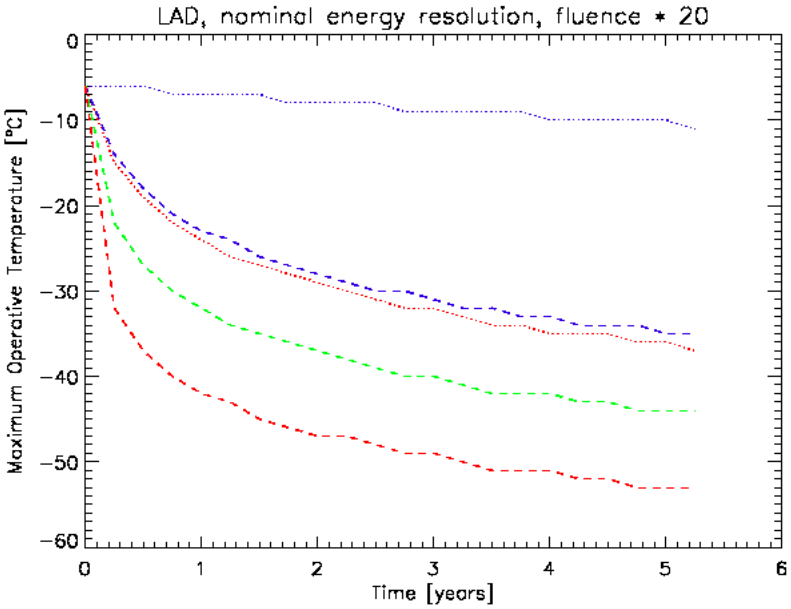

Figure 61: Maximum operative temperature of the LAD as a function of time for the nominal spectral resolution and assuming 20x the fluence (additional margin for the baseline operative temperature). The color and linestyle code of the orbits is the same as in Figure 59.

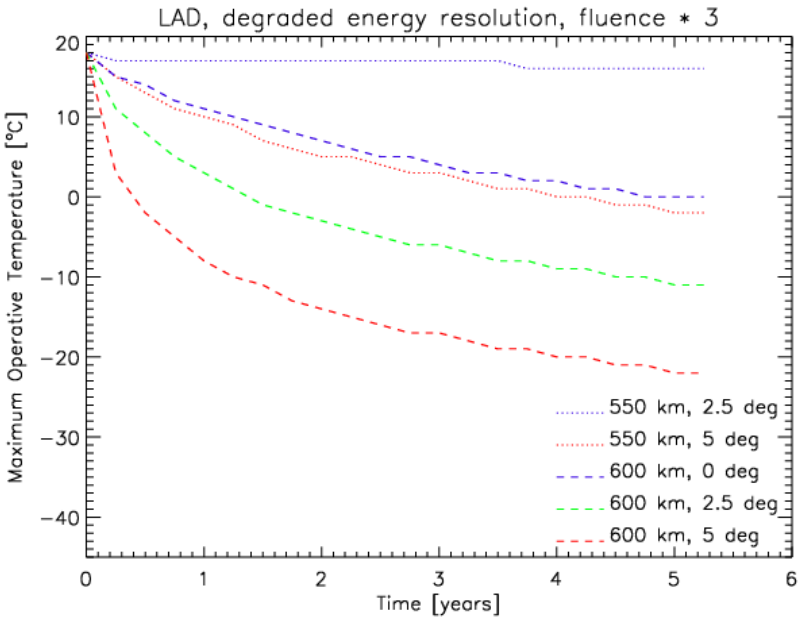

Figure 62: Maximum operative temperature of the LAD as a function of time for the degraded spectral resolution and assuming 3x the fluence (ESA requirement for the environment).

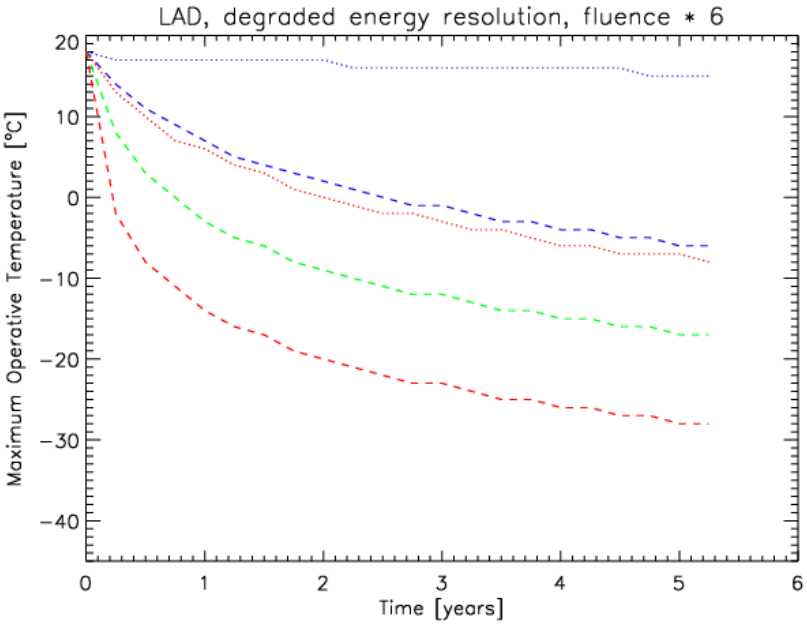

Figure 63: Maximum operative temperature of the LAD as a function of time for the degraded energy resolution and assuming 6x the fluence (design margin on the requirement). The color and linestyle code of the orbits is the same as in Figure 62.

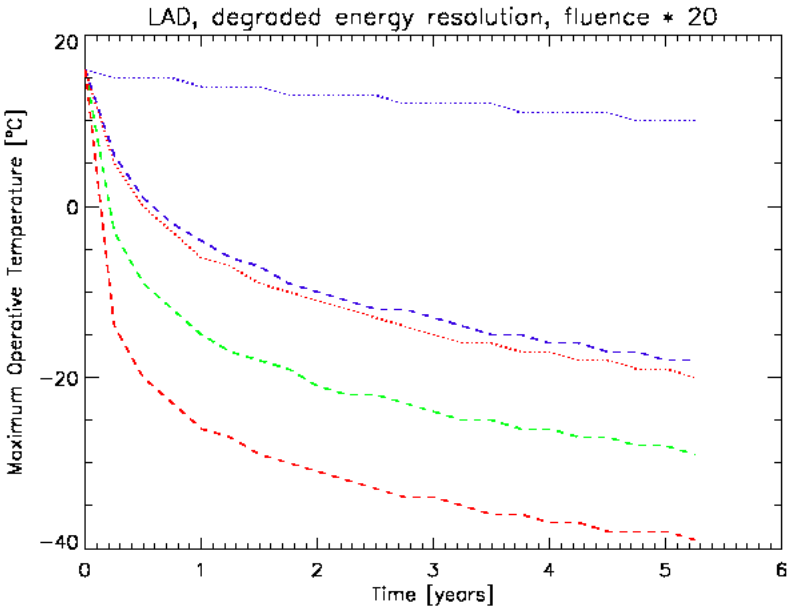

Figure 64: Maximum operative temperature of the LAD as a function of time for the degraded spectral resolution and assuming 20x the fluence (additional margin for the baseline operative temperature). The color and linestyle code of the orbits is the same as in Figure 62.

9.4 Operative temperature range of the WFM

Table 20: Operative temperature of the WFM in order to fulfill the requirement ENC < 13 e- after 4.25 years in orbit. In the table, $T_{fluence*3}$ is obtained with 3x the fluence (ESA requirement for the environment), $T_{fluence*6}$ with 6x the fluence (design margin on the requirement) and finally $T_{fluence*20}$ with 20x the fluence (additional margin for the baseline operative temperature).

Altitude [km]	Inclination [°]	$T_{fluence*3}$ [°C]	$T_{fluence*6}$ [°C]	$T_{fluence*20}$ [°C]
550	0.0	-1*	-1*	-3*
550	2.5	-1	-1	-3
550	5.0	-10	-14	-23
600	0.0	-9	-14	-22
600	2.5	-16	-22	-31
600	5.0	-28	-33	-42

*the orbit at 550 km, 0.0° is below the validity range for SPENVIS. Conservatively, we adopt for this orbit the same temperature values as in 550 km, 2.5°.

10 ANNEALING CONSIDERATIONS

The increase of the bulk leakage current of a semiconductor produced by the displacement damage is reduced in time by the annealing (see [RD-19] for more information). The annealing is studied in [RD-19] at temperatures of 21 °C or above (see e. g. Figure 65), and is more efficient at higher temperature. For example at 49 °C the residual damage after ~1 month is about one half than at 21 °C.

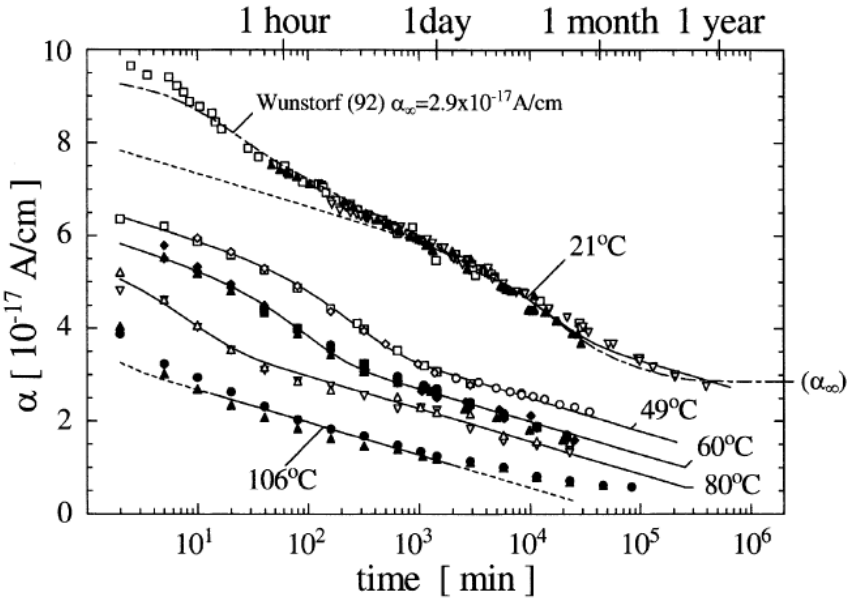

Figure 65: Variation of the current related damage rate α as a function of time for different temperatures (from [RD-19]). As a comparison, the value measured in [RD-6] at -50 °C without annealing is α = 11.1 × 10^{-17} A/cm.

10.1 Annealing at the operative temperature

Extrapolated lower limits in [RD-6] indicate that at -40 °C the velocity of annealing is about five orders of magnitude lower than at 21 °C. This means that the time required to obtain the same reduction of the displacement damage is approximately five orders of magnitude longer at -40 °C than at 21 °C.
The highest value of the operative temperature for the possible orbits studied for LOFT is -10 °C for the LAD (see Table 18) and -3 °C for the WFM (see Table 20). At -10 °C the extrapolated annealing is ~180 times slower than at 21 °C and at -3 °C it is ~51 times slower. For this reason we conservatively neglect the annealing of the displacement damage when estimating the increase of the bulk leakage current in the LOFT SDDs.

10.2 Possible annealing strategies in orbit as additional risk mitigation actions

In case the proton fluence in orbit resulted much higher than estimated with the models and the increase of the bulk leakage current could not be reduced at the operative temperatures listed in Table 18 and Table 20, an additional mitigation strategy would be needed.
A possible strategy exploits the annealing of the displacement damage, by increasing the temperature of the SDDs for a short and limited period of time. For this study we assume a value of the fluence which is one order of magnitude higher than estimated with AP8MIN including the margin of a factor of 20. For the orbit at 550 km altitude and 2.5° inclination, this value is 3×10^7 p/cm^2 in 4.25 years, that is 7.1×10^6 p/cm^2/yr. For this study we subdivide the duration of the LOFT mission into "blocks" of one year each. In each "block" the increase of leakage current is 3761 pA/cm^3.
As an example, by raising the temperature of the SDDs to 49 °C for one day per year, the increase of the leakage current during one "block" is reduced to:

without annealing	δI = 3761 pA/cm^3
after the first annealing session	δI = 1051 pA/cm^3
after the second annealing session	δI = 977 pA/cm^3
after the third annealing session	δI = 934 pA/cm^3
after the fourth annealing session	δI = 904 pA/cm^3
after the fifth annealing session	δI = 880 pA/cm^3

With the method sketched above, the operative temperature of the SDDs is shown in Table 21.

Table 21: Possible annealing strategy, assuming a fluence of 7.1×10^6 p/cm^2/yr and one day of annealing per year at a temperature of 49 °C.

Action	Time [yr]	Total Fluence [cm^{-2}]	Current increase δI [pA/cm^3]		Operative temperature [°C]		Comment
			With annealing	Without annealing	With annealing	Without annealing	
	1	7.1×10^6	3761	3761	-14	-14	After one

							year
Annealing	1	7.1×10^6	1051	3761	-10	-14	After first annealing
	2	1.4×10^7	4812	7522	-15	-18	After two years
Annealing	2	1.4×10^7	2028	7522	-12	-18	After second annealing
	3	2.1×10^7	5789	11283	-17	-21	After three years
Annealing	3	2.1×10^7	2962	11283	-13	-21	After third annealing
	4	2.8×10^7	6723	15044	-17	-23	After four years
Annealing	4	2.8×10^7	3866	15044	-14	-23	After fourth annealing
	5	3.5×10^7	7627	18805	-18	-24	After five years
Annealing	5	3.5×10^7	4746	18805	-16	-24	After fifth annealing

With this strategy, e. g. after four years the operative temperature is 9 °C higher than without any type of annealing.

11 THE VARIATION OF THE CHARGE COLLECTION EFFICIENCY

11.1 The Charge Collection Efficiency in silicon detectors

Impurities and defects in the semiconductor lattice, including the ones produced by Non Ionising Energy Losses, can act as trapping centers, which remove free carriers from the signal, thus reducing the Charge Collection Efficiency (CCE) of the detector.
For a charge carrier the probability to be trapped is proportional to the time needed for the collection. As described in [RD-28], if the thermal velocity of the carriers $v_{thermal}$ > v_{drift} (drift velocity),

$$q(t) = q(0)\, e^{-t/\tau} \tag{13}$$

where q(t) represents the drifting charge as a function of time and τ is a time constant. Consequently, for a collection time t_c,

$$CCE = \frac{q(t_c)}{q(0)} = e^{-t_c/\tau} \tag{14}$$

In the LOFT SDDs, the maximum collection time is measured for the photons impinging exactly at the half of the detector tile, at a distance of 3.5 cm from the anodes, and is $t_c \approx 6.8$ μs at 20 °C, $t_c \approx 5.2$ μs at -10 °C and $t_c \approx 4.4$ μs at -30 °C. Since the drift

length is the same for the SDDs in the LAD and WFM, the value of the collection time is the same for both instruments.
Here we verify the hypothesis, specified in [RD-28], that for the LOFT SDDs $v_{thermal} > v_{drift}$. In a semiconductor the thermal velocity of the electrons is given by

$$v_{thermal} = \sqrt{\frac{4\,k_B\,T}{3\,m_e^*}} \tag{15}$$

where T is the absolute temperature, $k_B = 1.381 \times 10^{-23}$ m^2 kg/s^2 is the Boltzmann constant, $m_e^* = 0.26 \times m_e$ in silicon and $m_e = 9.109 \times 10^{-31}$ kg is the electron mass. The thermal velocity of electrons calculated from Eq. (15) for temperatures between 240 K and 320 K is shown in Figure 66. For example, at an operative temperature of -30 °C, $v_{thermal} = 1.37 \times 10^7$ cm/s, at -10 °C $v_{thermal} = 1.43 \times 10^7$ cm/s (see Figure 66).
The drift velocity is

$$v_{drift} = \mu\,E \tag{16}$$

where E is the electric field and μ is the mobility,

$$\mu = 1400 \times \left(\frac{300\,K}{T}\right)^{2.42} \frac{cm^2}{V\,s}$$

from [RD-29]. For the LOFT SDDs, the electric field E = 360 V/cm, thus at -30° C μ = 2331 $cm^2/(V\,s)$ and $v_{drift} = 8 \times 10^5$ cm/s, while at -10 °C μ = 1923 $cm^2/(V\,s)$ and $v_{drift} = 7 \times 10^5$ cm/s. The thermal velocity of the carriers is thus more than one order of magnitude higher than the drift velocity and we can safely apply Eq. (13) and Eq. (14).

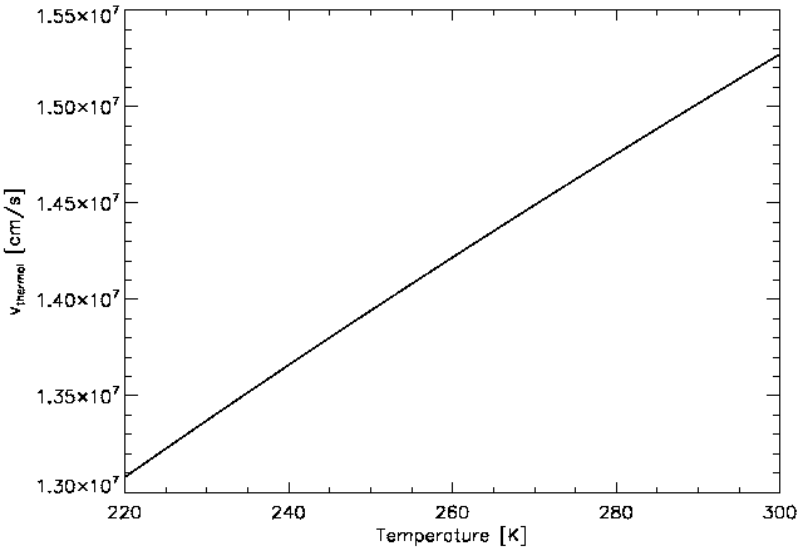

Figure 66: Thermal velocity of electrons in silicon calculated from Eq. (15).

After the irradiation of the detector with a fluence Φ, the time constant τ in Eq. (13) and Eq. (14) is such that [RD-30]

$$\frac{1}{\tau} \sim \beta\,\Phi \tag{17}$$

and is dominated by the contribution from the radiation damage. The constant β is measured for neutrons, protons and pions in [RD-30]. The authors of [RD-30] remark that the value of β depends on the type of particle used in the irradiation, consequently the NIEL hypothesis cannot be used when calculating the CCE. Different values of β are measured in [RD-30] for holes and electrons and for an irradiation with protons, neutrons and pions. Considering the LOFT representative case of electrons as charge carriers and the displacement damage produced by protons, the measured value in [RD-30] is $\beta = 5.6 \times 10^{-16}$ cm^2/ns for a temperature T_0 of -10° C. In [RD-30] it is also shown that β follows a power-law behaviour as a function of temperature,

$$\beta(T) = \beta(T_0) \times \left(\frac{T}{T_0}\right)^{\alpha} \quad (18)$$

where α = -0.86 for electrons as charge carriers (the case of the LOFT SDDs) and $\beta = 5.6 \times 10^{-16}$ cm^2/ns at T_0 = 263 K (-10° C). Following Eq. (18), at a temperature of -30° C, $\beta = 6.0 \times 10^{-16}$ cm^2/ns and at -10 °C $\beta = 5.6 \times 10^{-16}$ cm^2/ns.
As indicated in [RD-30] and [RD-31], the annealing reduces of only ~35 % the value of β for electrons. Since, from Eq. (14) and Eq. (17),

$$1 - CCE \simeq \beta \, \Phi \, t_c \quad (19)$$

reduction of the β constant implies a mitigation of the trapping and thus an increase of the CCE. The annealing of the β constant has a different behaviour in time than the annealing of the current increase produced by the displacement damage, as shown in Figure 67 from [RD-31]. In particular, the time constant τ_A follows the Arrhenius relation

$$\tau_A = \tau_0 \exp(E/k_B T) \quad (20)$$

where, for electrons as charge carriers, $\tau_0 = 3.88 \times 10^{-14}$ min and E = 1.06 eV [RD-31]. As usual, k_B is the Boltzmann constant and T is the temperature. The resulting time constant is ~2.7 years at 0 °C and ~14.8 years at -10°C. For this reason we can safely neglect the annealing of the trapping probability for the LOFT SDDs.

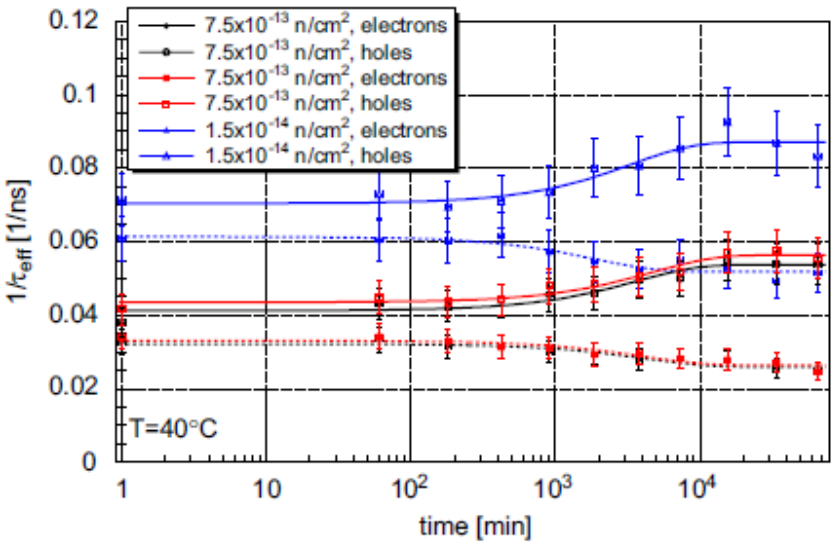

Figure 67: Annealing of trapping probability at +40 °C from [RD-31].

11.2 Expected variation of the CCE for the LOFT SDDs in orbit

The values of the variation of the CCE at End of Life for the orbits studied for LOFT are shown for the LAD in Table 22 and for the WFM in Table 23. In the estimation we apply to the fluence the margin of a factor of 20 used to calculate the operative temperatures of the LAD and WFM (see Sec. 4.5).

Table 22: Value of the CCE of the LAD SDDs at End of Life (4.25 years) for the orbits studied for LOFT. Φ_{AP8MIN} is the nominal fluence, $T_{fluence*20}$, τ and 1-CCE are computed assuming the margin of a factor of 20 on the fluence.

Altitude [km]	Inclination [°]	Φ_{AP8MIN} [cm^{-2}]	$T_{fluence*20}$ [°C]	τ at $T_{fluence*20}$ [ms]	1-CCE at $T_{fluence*20}$ [%]
550	0.0	1.5×10^5	-10*	136.6	0.004
550	2.5	1.5×10^5	-10	136.6	0.004
550	5.0	8.1×10^6	-35	2.3	0.2
600	0.0	6.8×10^6	-34	2.8	0.1
600	2.5	2.4×10^7	-43	0.8	0.5
600	5.0	8.9×10^7	-52	0.2	1.7

Table 23: Value of the CCE of the WFM SDDs at End of Life (4.25 years) for the orbits studied for LOFT. Φ_{AP8MIN} is the nominal fluence, $T_{fluence*20}$, τ and 1-CCE are computed assuming the margin of a factor of 20 on the fluence.

Altitude [km]	Inclination [°]	Φ_{AP8MIN} [cm^{-2}]	$T_{fluence*20}$ [°C]	τ @ $T_{fluence*20}$ [ms]	1-CCE @ $T_{fluence*20}$ [%]
550	0.0	$1.5 \times 10^{5*}$	-3*	139.7	0.004
550	2.5	1.5×10^5	-3	139.7	0.004
550	5.0	5.4×10^6	-23	3.6	0.1
600	0.0	5.1×10^6	-22	3.9	0.1
600	2.5	1.5×10^7	-31	1.3	0.3
600	5.0	6.6×10^7	-42	0.3	1.3

11.3 Experimental measurements of the variation of the CCE

In this section we summarise the results of the experimental verification of the variation of the CCE after the irradiation with a proton beam. More details about this campaign are reported in [RD-32].

11.3.1 Characteristics of the SDD under test

The detector under test is a SDD of the FBK-2 production, with a geometric area of 5.52 cm × 7.25 cm. The SDD is divided into two electrically independent halves: the LAD half, with anode pitch of 833 μm and the WFM half, with anode pitch of 294 μm. The drift length is 3.5 cm and is representative of the LOFT SDDs.
A picture of the device under test is shown in Figure 68. The SDD is mounted on a dedicated Printed Circuit Board (PCB) with discrete components. Only eight anodes in the LAD half are connected to the Front-End Electronics (FEE) made of JFETs, highlighted by the yellow circle on the right in Figure 68.

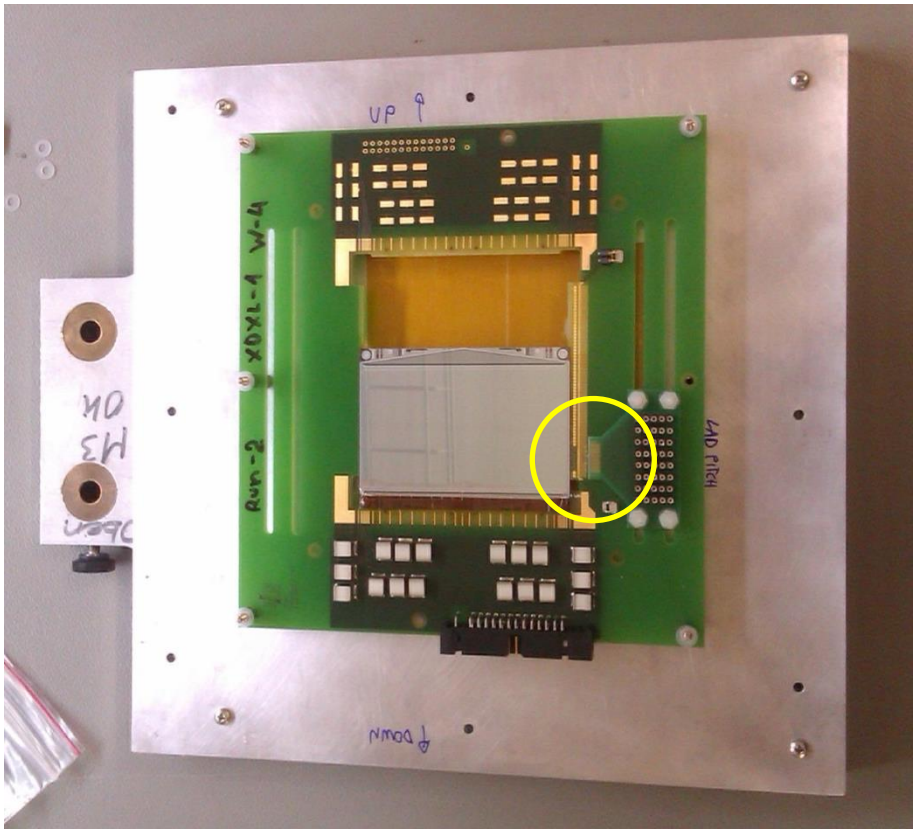

Figure 68: Photo of the PCB with the SDD and the electronics. The yellow circle highlights the anodes connected to the JFETs as FEE.

11.3.2 Method of measurement

The cloud of electrons produced during the interaction of X-rays in the SDDs is continuously drifted toward the anodes and collected there. The variation of the CCE translates into a displacement of the peak position of the lines in the spectrum toward smaller energy values. The amount of the displacement of the peak position equals the variation of the CCE, listed in Table 22 and Table 23.
The measurement of the variation of the CCE of the LOFT SDDs is performed by comparing the detected peak position of the Kα line from a collimated ^{55}Fe source at three different locations along the drifting channel: near the anodes, at 15 mm distance and 30 mm distance. The measurement in the three positions removes possible systematic effects, such as small variations of the gain and offset of the FEE, that may affect the measure of the absolute value of the peak position in the spectrum of the ^{55}Fe source.
By repeating before and after the irradiation the characterisation described above, we measure the variation of the CCE. Since for the selected proton fluence the NIEL will produce a small decrease of the CCE but a relevant increase of the bulk leakage current, and thus of the FWHM of the ^{55}Fe lines, the characterization will be performed at a temperature of about -38 °C in the thermal chamber. In fact, the variation of the CCE is almost insensitive of temperature while the leakage current, which increases the FWHM, heavily depends on a temperature variation as shown in Eq. (9) and Eq. (12). For this reason, by working at low temperature, we will mitigate the increase of the

FWHM while leaving the variation of the CCE almost unaffected, thus increasing the sensitivity of the measurement.
Given the difficulty of obtaining an absolute position of the source at a level of fractions of mm with the set-up available inside the thermal chamber, we decide to use the relative distance instead. We compare the spectra acquired in three different positions along the drift channel: the first one is near the anodes (at a distance of ~3 mm from them), the second one at 15 mm and the third position is at a distance of ~30 mm from the first one. The source is positioned using a micrometric translation stage. With this method, we can keep fixed the relative distance between the three positions of the source, thus "relaxing" the constraints on the absolute location.
We use a source of ^{55}Fe for the characterization, with activity of ~1.2 mCi. The ^{55}Fe emits two fluorescence X-ray lines, the Mn Kα at 5.9 keV and the Mn Kβ at 6.5 keV. We verified that, by collimating the source with a slit (1 mm × 10 mm) and a diaphragm (of 400 μm aperture), the surface of the beam on the detector is 1.5 mm × 0.75 mm, i. e. still on the same anode of the LAD half, and the counting rate is ~6 cts/s. More details on the simulations in order to assess the experimental set-up are reported in [RD-32].
During the drift toward the anodes, the size of the electron cloud, created after the interaction of an X-ray photon, increases. Following [RD-24] and [RD-27], the expected size of the charge cloud for a drift length of 3.5 cm is ~1 mm. Since the anode pitch of the SDD under test is 833 μm, the charge will be spread on 1 – 3 anodes. In order to ensure a complete collection of the charge, we decide to sum the signals of the triggering anode and of the two neighbours on the left and right. The same method is applied when the ^{55}Fe source is near the anodes and when it is at about the end of the drift channel.
The SDD under test is connected to a FEE based on discrete JFETs. Eight anodes can be read-out using this FEE and the test equipment allows the selection of one triggering channel. We select on the triggering channel the events whose amplitude is higher than a threshold specified by the user (200 ADC channels, corresponding to ~3.5 keV). As specified above we sum the amplitude of the signals on the triggering channel and on the two neighbours, on the left and right. The remaining five channels are used to estimate the Common Mode Noise, that is subtracted from the signal. The pedestals of the ADC are also subtracted, independently estimated on each read-out channel with a specific measurement using the same Test Equipment.

11.3.3 Experimental set-up

The characterisation of the SDD before and after the irradiation is performed at the laboratory of INAF IAPS Roma using a thermal chamber. In order to mitigate the expected increase of the bulk leakage current due to NIEL during the irradiation, ~2.4 nA/anode considering the annealing at few days after the irradiation, we perform the characterisation at a temperature around -38 °C. The detector temperature is measured using an AD590 thermometer, placed inside the detector box. A picture of the experimental set-up inside the thermal chamber is shown in Figure 69.
For the measurements we used the X-ray fluorescence line of Mn Kα at 5.9 keV. The source of ^{55}Fe is moved along the drift channel using a micrometric translation stage, with a position accuracy of 0.01 mm. The energy resolution of the SDD under test is enough to partially separate the two lines, that are simultaneously fitted to measure the peak position.

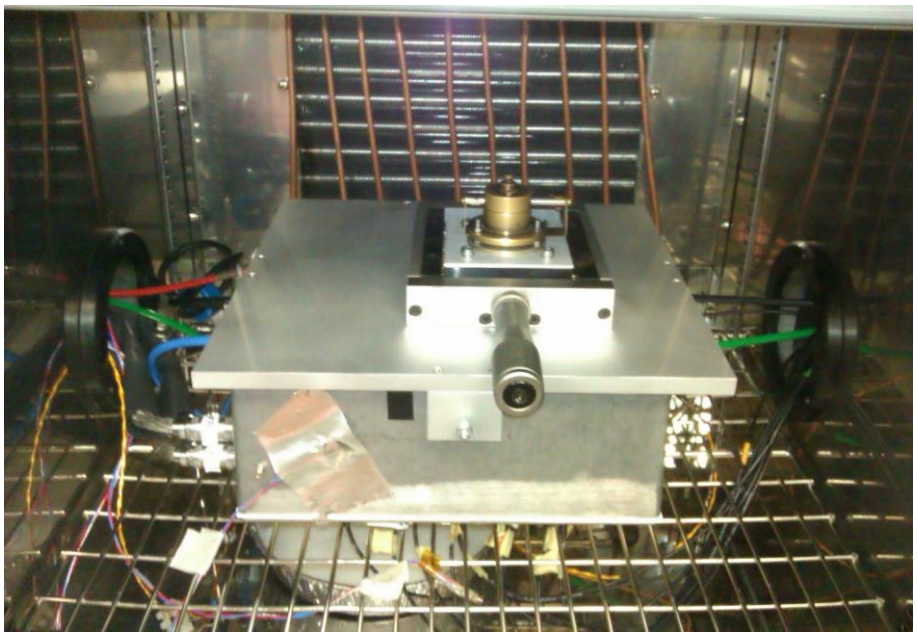

Figure 69: Picture of the detector box inside the thermal chamber. The micrometric translation stage is on top of the detector box.

11.3.4 Characterisation before the irradiation

We characterised the SDD before the irradiation using the method and set-up described in Sec. 11.3.2 above. In Figure 70 we show a superposition of the spectra near the anodes (black line) and at the end of the drift channel (green line) before the irradiation.
By moving the source of 30 mm we find that the position of the peak in the spectrum, reconstructed with the fit in Sec. 11.3.3 above, changes of ~0.2 ADC channels. This value can be considered as the minimum variation of the peak position that can be appreciated with the adopted measurement method.

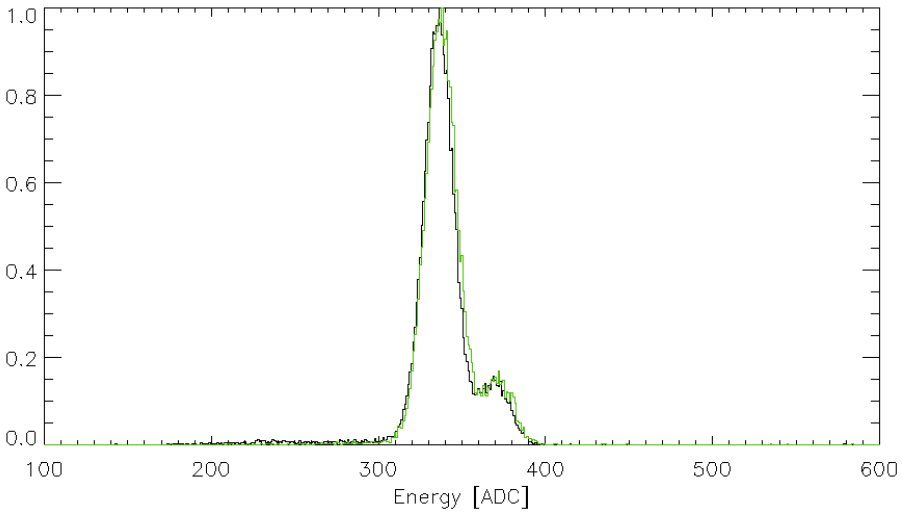

Figure 70: Superposition of the spectra of the ^{55}Fe source placed at x = 31.0 mm (near the anodes, black line) and at x = 1.0 mm (at the end of the drift channel, green line)

before the irradiation. Both spectra are acquired at a temperature of -36 °C. The histograms are normalised to the maximum counts per bin.

11.3.5 Irradiation at PSI

The proton beam during the irradiation has an energy of 11.2 MeV and a FWHM of ~6 MeV. The calibration of the beam is described in Sec. 8.1.2.3. In particular, the uniformity of the beam in the horizontal direction (parallel to the drift direction of the SDD) is shown in Figure 40, in the vertical direction (parallel to the direction of the anodes) is shown in Figure 41.
The map of the reconstructed beam intensity is shown in Figure 71. The position of the PCB containing the SDD with respect to the beam during the irradiation is shown in Figure 72. The average fraction of the beam intensity on the anodes connected to the FEE is 88.8 %. More details about the irradiation at PSI are reported in [RD-32].
During the irradiation, the PCB with the SDD under test is mounted on an aluminum support structure, attached to the sample holder of the PIF. The JFETs FEE and the other electronic devices on the PCB are shielded from protons with an aluminum layer of ~3 mm thickness. All protons in the beam are completely stopped by this layer.

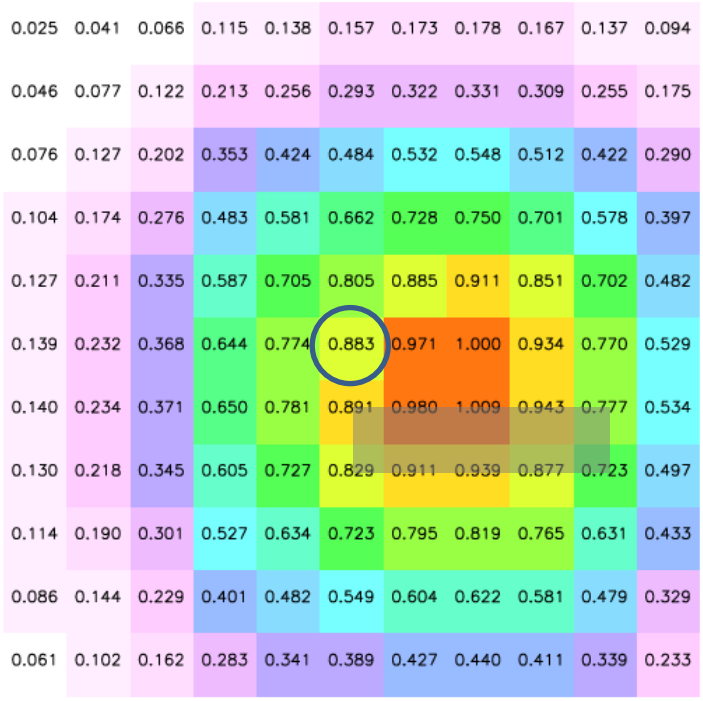

Figure 71: Map of the reconstructed beam intensity, at 1 cm step. The center of the beam is indicated by the blue circle. The horizontal x axis is in the direction of the charge drift. The vertical y axis in the direction of the readout anodes. The grey box indicates the region of the anodes connected to the FEE (3.5 cm × 1.0 cm, see [RD-32] for more details). The average fraction of the beam on the anodes is 88.8 %.

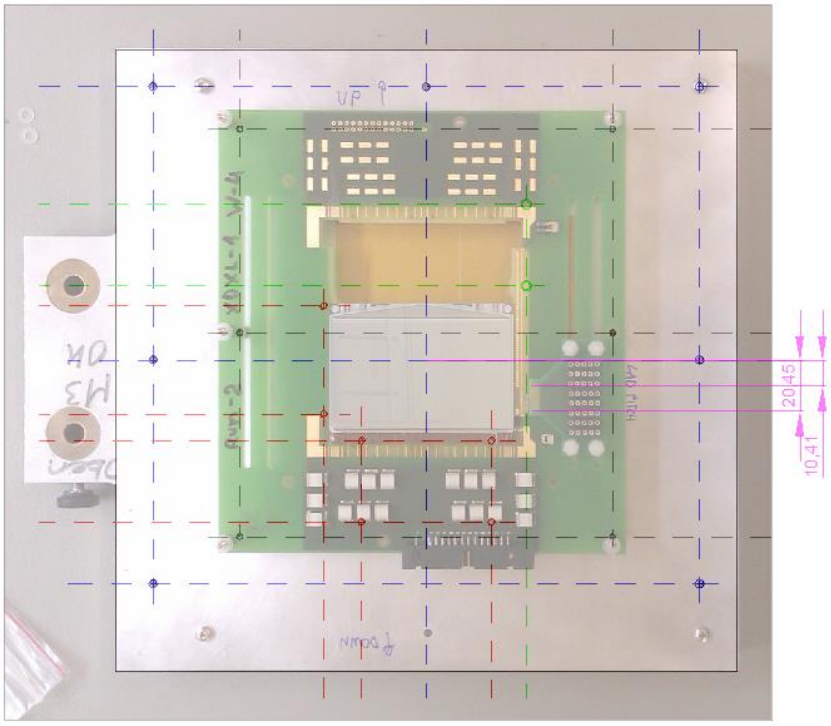

Figure 72: Position of the PCB with the SDD with respect to the beam during the irradiation. The anodes connected to the FEE are located at a distance between 2.05 cm and 1.04 cm from the geometric center of the beam. The average fraction of the beam on the anodes is 88.8 %.

11.3.6 Characterisation after the irradiation

After the irradiation at PSI, we repeated the characterisation of the SDD described in Sec. 11.3.4 above. The superposition of the spectra measured after the irradiation at the end of the drift channel and near the anodes is shown in Figure 73. The measurement before the irradiation is shown in Figure 70 for comparison.

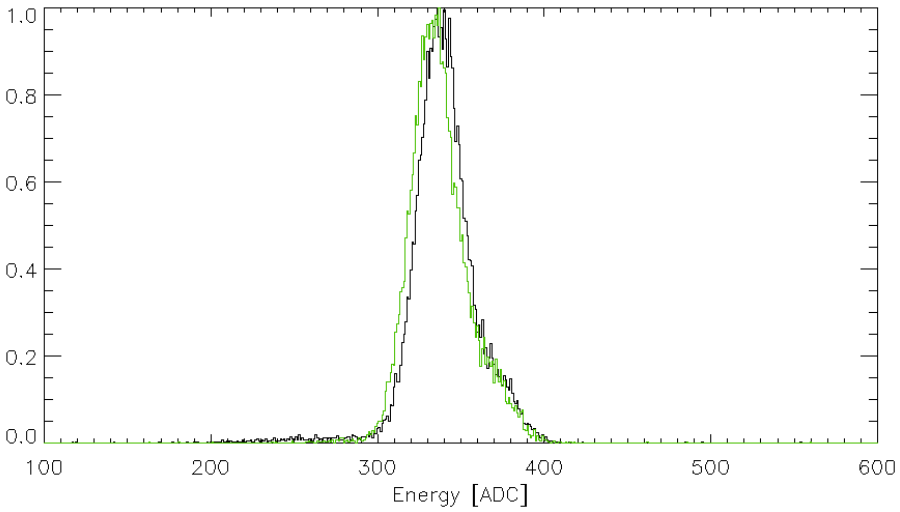

Figure 73: Superposition of the spectra of the ^{55}Fe source placed at x = 31.0 mm (near the anodes, black line, at a temperature of -38 °C) and at x = 1.0 mm (at the end of the drift channel, green line, at a temperature of -37 °C) after the irradiation. The histograms are normalised to the maximum counts per bin.

11.3.7 Variation of the CCE

We show in Figure 74 the position of the peak of the Mn Kα line reconstructed from the fit of the spectra acquired near the anodes, at the end of the drift channel and at mid-distance, before (black line) and after (red line) the irradiation. As shown in the figure, the measured variation of the CCE is (0.65 ± 0.15) % at a distance of 30 mm from the reference position near the anodes.

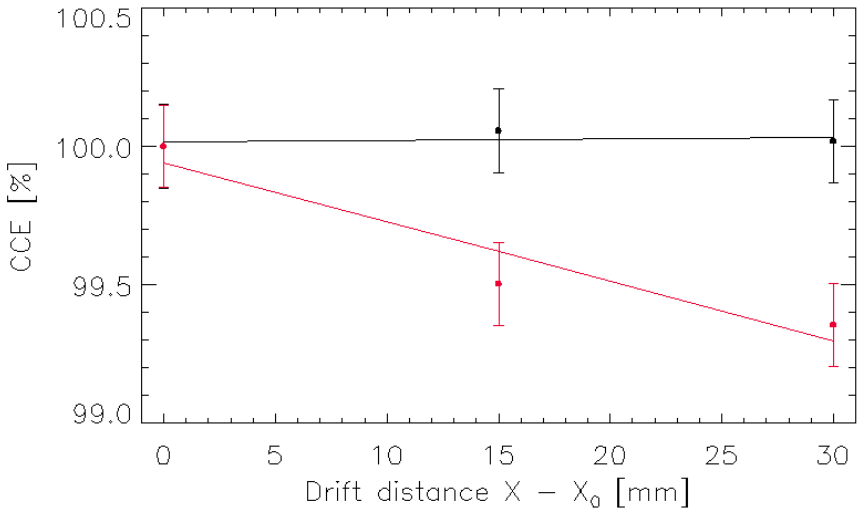

Figure 74: Position of the reconstructed peak of the Mn Kα line as a function of distance from the anodes before (black line) and after (red line) the irradiation.

The average fluence on the anodes of the LAD half connected to the FEE is 7.9 × 10^8 p/cm^2, considering that the average fraction of the beam intensity on the anodes is 88.8 % (see the map in Figure 71). The analytical estimation of the CCE reduction due to the irradiation can be carried out, in the measurement conditions, following [RD-30]: we obtain a CCE of 99.2%, i. e. a reduction of 0.8% that is compatible with the measurements. The variation of the CCE takes into account the fraction of the beam on the anodes connected to the FEE

In conclusion, after the irradiation at PSI we measured a variation of the CCE of (0.65 ± 0.15) % of the FBK-2 SDD (see Figure 74). This value is in good agreement with the expected variation of 0.8 %.

12 THE EFFECT OF DEBRIS AND MICRO-METEOROIDS FOR LOFT

12.1 Models for micrometeoroids and orbital debris

Spacecrafts in orbit around the Earth experience the impact of hypervelocity particles, i. e. micrometeoroids and orbital debris (MMODs). Models to separately estimate the

expected flux of debris and micrometeoroids are referred to in [RD-33]. As reported in [RD-33], the meteoroid and debris fluxes are usually specified as a time-averaged flux against a single sided, randomly tumbling surface, i. e. equivalent to an acceptance angle of 2π sr. Flux is defined as number of intercepted objects per unit time and area. The relevant area for this flux is the actual outer surface area of a spacecraft element. Since the LOFT spacecraft will be pointed and oriented following the Observation Plan, we assume an isotropic distribution of MMODs in our analysis.

12.1.1 The model of the expected flux of debris

In [RD-33] the flux of debris is estimated using the ESA Master 2005 model [RD-34]. For the analysis of the impacts from debris we assume the particle density (2.8 g/cm^3) and velocity (13 km/s) specified in [RD-33], **but the worst case of normal incidence**, while [RD-33] takes into account impacts at an angle of 45°.

12.1.2 The models of the expected flux of micrometeoroids

In [RD-33] the flux of micrometeoroids is estimated using the model by Gruen et al. [RD-35]. For the analysis of the impacts from micrometeoroids we assume the nominal values given in [RD-33]: particles with density of 2.5 g/cm^3 and impacts at normal incidence at a velocity of 20 km/s.

12.1.3 Table of the expected flux of MMODs for LOFT

The expected isotropic integral flux of debris and micrometeoroids from [RD-33] is listed in

Table 24 and shown in Figure 75. As a worst case, the penetration depth in Figure 75 is estimated for micrometeoroids, assuming a density of 2.5 g/cm^3 and a velocity of 20 km/s as specified in [RD-33].

Table 24: Cumulative number of impacts, N, to a randomly oriented plate for a range of minimum particle sizes. The results are for an orbit at 600 km altitude and 0° – 5° inclination. The debris fluxes were obtained by the MASTER 2005 model [RD-34] for an epoch of May 1st, 2005. The meteoroid fluxes were obtained by the model in [RD-35] assuming a density of 2.5 g/cm^3 to convert masses to diameters.

Diameter [cm]	Fluence [m^{-2} yr^{-1}]		
	Debris	Meteoroids	Total
0.0001	6.78×10^2	1.43×10^3	2.11×10^3
0.0002	3.75×10^2	6.72×10^2	1.05×10^3
0.0004	3.10×10^2	3.12×10^2	6.22×10^2
0.0007	2.27×10^2	1.82×10^2	4.09×10^2
0.001	1.68×10^2	1.25×10^2	2.93×10^2
0.002	8.46×10^1	5.30×10^1	1.38×10^2
0.004	3.62×10^1	1.58×10^1	5.20×10^1
0.007	1.68×10^1	4.53	2.13×10^1
0.01	7.65	1.68	9.33
0.02	8.87×10^{-1}	2.03×10^{-1}	1.09
0.04	1.16×10^{-2}	1.88×10^{-2}	3.04×10^{-2}

0.07	1.22×10^{-3}	2.70×10^{-3}	3.92×10^{-3}
0.1	3.55×10^{-4}	6.14×10^{-4}	9.69×10^{-4}
0.2	1.03×10^{-4}	4.23×10^{-5}	1.45×10^{-4}
0.4	2.69×10^{-5}	2.78×10^{-6}	2.97×10^{-5}
0.7	1.26×10^{-5}	3.20×10^{-7}	1.29×10^{-5}
1	7.22×10^{-6}	7.10×10^{-8}	7.29×10^{-6}
2	2.31×10^{-6}	4.47×10^{-9}	2.31×10^{-6}
4	1.05×10^{-6}	2.80×10^{-10}	1.05×10^{-6}
7	1.87×10^{-7}	3.00×10^{-11}	1.87×10^{-7}

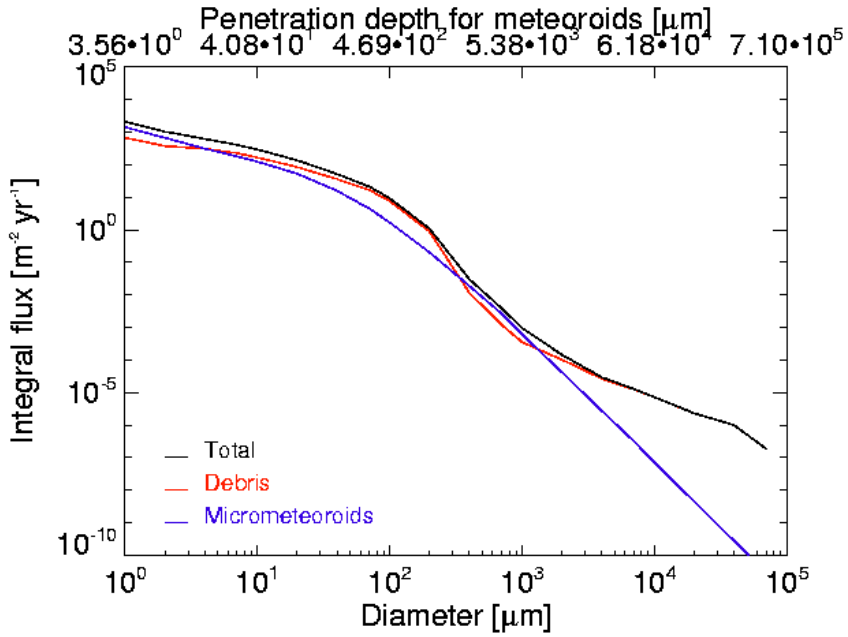

Figure 75: Expected integral flux of debris (red) and micrometeoroids (blue) at the LOFT orbit from [RD-33]. The black line is the sum of the two components. As a worst case, the penetration depth is estimated for micrometeoroids, assuming a density of 2.5 g/cm^3 and a velocity of 20 km/s as specified in [RD-33].

As shown in Figure 75, the largest number of particles have a diameter between ~1 µm and ~100 µm, while the flux rapidly drops for a size above this latter value. The penetration depth in Figure 75 is estimated with the Cour-Palais formula for brittle materials [RD-36] assuming the worst case of micrometeoroids, with a density of 2.5 g/cm^3 and a velocity of 20 km/s.

12.2 Relevant formulas for the analysis of MMODs

12.2.1 Formula to estimate the crater depth

In order to estimate the depth P of the craters on the SDDs, we employ the formula by Cour-Palais for brittle materials (see e. g. [RD-36]):

$$P = 0.53\, d^{1.06}\, \rho_{particle}^{0.5}\, v_{particle}^{2/3} \qquad (21)$$

where d is the particle diameter (in cm), $\rho_{particle}$ and $v_{particle}$ are the particle density (in g/cm^3) and velocity (in km/s), respectively.

12.2.2 Formulas to estimate the threshold thickness for penetration

Various types of Ballistic Limit Equations (BLEs) are discussed in [RD-37] and define impact conditions (i.e., particle size, particle density, impact velocity, and impact angle) that result in threshold failure of specific spacecraft shields, components, or subsystems. A combination of hypervelocity impact (HVI) test results and analyses are used to determine the BLEs. Many BLEs are semi-empirical, combining data from impact tests as well as the results of analytical models or numerical simulations [RD-37].
As specified in [RD-37], two types of BLEs are typically defined for a particular spacecraft shield or component:

(1) Design equations. These are used to determine the dimensions of a shield (e.g., thicknesses/areal densities, spacing, etc.) for a "design" impact condition (projectile diameter, density, impact velocity, and angle).
(2) Performance equations. These equations relate particle size on threshold failure of a shield or component to impact and target parameters.

Since the composition and thickness of the shielding materials for the LOFT instrumentation (e. g. MLI, thermo-optical filter) are dictated by the performances mainly in terms of thermal-optical insulation and transparency to X-rays, we use the proper performance equations to evaluate the capabilities of these shielding layers to stop MMODs. For this purpose, we estimate the minimum particle diameter (d_{crit}) that can penetrate a given shield.

12.2.2.1 Single wall

The minimum particle diameter d_{crit} that can penetrate a single layer of material is estimated in [RD-37] as

$$d_{crit} = \left[\frac{t_{shield}}{k_{damage}} \frac{BHN^{0.25} \left(\rho_{shield}/\rho_{particle}\right)^{0.5}}{5.24 \left(v_{particle}/c_{shield}\right)^{2/3}} \right]^{18/19} \quad (22)$$

where

t_{shield} = thickness of the shielding layer [cm]
k_{damage} = damage parameter (assumed 1.8 for perforation of the shield)
BHN_{shield} = Brinell Hardness Number of the shielding layer
ρ_{shield} = density of the shielding layer [g/cm^3]
$\rho_{particle}$ = density of the particle [g/cm^3]
$v_{particle}$ = velocity of the particle (assumed as orthogonal to the shield) [km/s]
c_{shield} = velocity of sound of the shield [km/s]

This formula has been used to calculate the minimum diameter of MMODs that can pass through the MLI of the WFM and the thermo-optical filter of the LAD. As a worst case, we assume a damage parameter of 1.8, corresponding to the perforation of the shield, that is the maximum possible damage, and impacts orthogonal to the surface.

12.2.2.2 Whipple Wall

By including the beryllium layer below the MLI in the LOFT WFM, we obtain a Whipple Wall, with a higher capability to stop the hypervelocity particles. As reported in [RD-37], a Whipple Wall consists of a thin sacrificial bumper and a rear wall, with some interior spacing. For the WFM, the MLI acts as the sacrificial bumper and the beryllium layer as the rear wall.
In case of a Whipple Wall, for an orthogonal component of the particle velocity $v_{particle}$ > 7 km/s, the minimum diameter d_{crit} of particles that can penetrate the Whipple Wall is given by [RD-37]

$$d_{crit} = 3.918\, t_{Wall}^{2/3}\, \rho_{particle}^{-1/3}\, \rho_{bumper}^{-1/9} \left(v_{particle} \cos\theta\right)^{-2/3}\, distance^{1/3}\, (\sigma_{Wall}/70)^{1/3} \quad (23)$$

where

t_{Wall} = thickness of the rear wall (beryllium layer) [cm]
$\rho_{particle}$ = density of the particle [g/cm^3]
ρ_{bumper} = density of the bumper (MLI) [g/cm^3]
$v_{particle}$ = velocity of the particle (assumed as orthogonal to the shield) [km/s]
distance = distance between the bumper and the rear wall [cm]
σ_{wall} = yield stress of the rear wall (beryllium layer) [ksi]

12.2.3 Formula to estimate the diameter of craters from impacts

From [RD-38], the ratio of the crater diameter D and the particle diameter d is given by

$$\frac{D}{d} = 1 + 1.5 \left(\frac{f}{d}\right) v^{0.3} \left[\frac{1}{1+\left(\frac{f}{d}\right)^2 v^{-n}}\right] \quad (24)$$

where f is the thickness of the layer where the impact happens and v is velocity (in km/s). The exponent n is given by

$$n = 1.02 - 4\exp(-0.9\, v^{0.9}) - 0.003\,(20 - v) \quad (25)$$

This formula is empirically derived from the data of iron projectiles on an aluminum layer. We can assume this formula as an upper limit to estimate the diameter of the craters on the LAD thermo-optical filter given the particle diameter and velocity.

12.3 Expected rate of impacts for LOFT

12.3.1 Expected rate of MMODs on the LAD SDDs

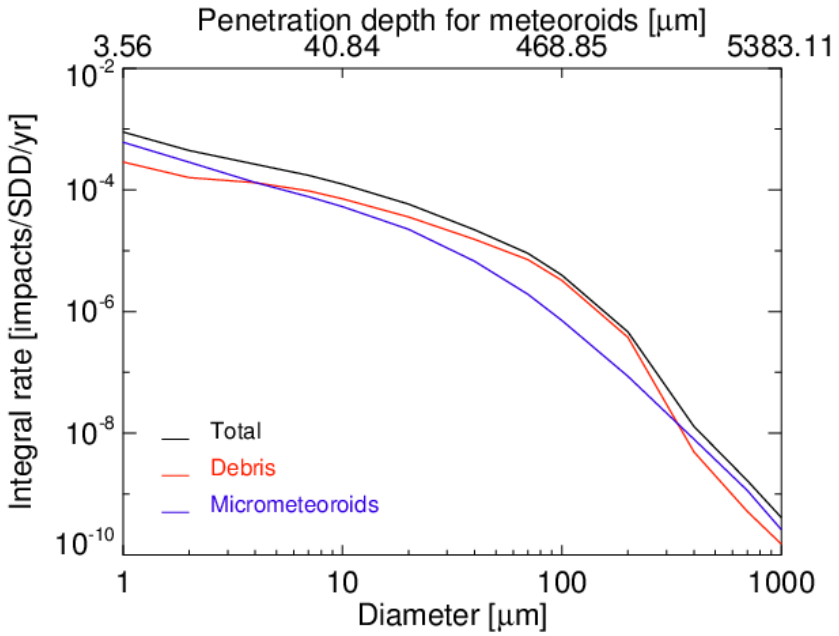

Figure 76: Expected integral rate of debris (red) and micrometeoroids (blue) on the LAD SDDs from [RD-33]. The black line is the sum of the two components. As a worst case, the penetration depth is estimated for micrometeoroids, assuming a density of 2.5 g/cm^3 and a velocity of 20 km/s as specified in [RD-33].

A set of micro channel plates (MCPs), manufactured by Photonis SAS with materials and technology representative of the LAD collimator, have been exposed to the space environment for 756 days on the Russian docking module (Pirs) of the International Space Station in order to evaluate the long-term effects of the environment on the thermal properties of the devices [RD-39]. The MCPs bore an aluminum film of 60 nm thickness, similar to the one selected for LOFT (80 nm). After the exposure, the MCPs have been inspected at the Scanning Electron Microscope (SEM) to measure the distribution of the hole size on the aluminum film. No evidence was found for mechanical damage to the MCP, whose wall thickness was about one-tenth that envisaged for the LAD [RD-39].
As a further verification of the above in-orbit result, we estimated from Eq. (22) that the critical diameter of the MMODs able to perforate the LAD collimator is ~700 μm. The expected rate for such particles is ~7 × 10^{-2} particles/yr for the whole LAD (corresponding to 0.3 impacts on the LAD over the mission lifetime).
Consequently, the particles able to reach the LAD SDDs are only the ones that pass through the open channels of the collimator, with a FoV of ~3 × 10^{-4} sr. The expected rate of impacts on the LAD SDDs is thus shown in Table 25 and Figure 76, computed assuming for the LAD 2016 SDDs and a geometric surface of 17.66 m^2.

Table 25: Expected rate of MMODs on the LAD SDDs. The total integral flux and total rate are the sum of debris and micrometeoroids. The penetration depth is estimated with the the Cour-Palais formula for brittle materials [RD-36] assuming the **worst case** of micrometeoroids, with a density of 2.5 g/cm^3 and a velocity of 20 km/s.

Diameter [μm]	Total integral flux [particle/m^2/yr]	Total rate [impacts/SDD/yr]	Penetration depth of micrometeoroids [μm]
1	2108	9.0×10^{-4}	3.6
2	1047	4.4×10^{-4}	7.4
4	622	2.6×10^{-4}	15.4
7	409	1.7×10^{-4}	28.0
10	293	1.2×10^{-4}	40.8
20	138	5.8×10^{-5}	85.1
40	52	2.2×10^{-5}	177.5
70	21	9.1×10^{-6}	321.2
100	9.3	4.0×10^{-4}	468.8
200	1.1	4.6×10^{-7}	977.5
400	3.0×10^{-2}	1.3×10^{-8}	2038.1
700	3.9×10^{-3}	1.7×10^{-9}	3688.4
1000	9.7×10^{-4}	4.1×10^{-10}	5383.1

12.3.2 Expected rate of MMODs on the WFM MLI

Similarly to the LAD, the expected rate of impacts on the MLI of a WFM camera is calculated assuming the differential flux of MMODs computed from the data in Table 24, a geometric surface of 26 cm × 26 cm for the coded mask of a camera, and an acceptance angle of 2π sr. We list the expected rates in Table 26.

The equations to estimate the critical diameter, i. e. the minimum diameter of hypervelocity particles able to pass through a shielding material, are discussed in Sec. 12.2.2. For the WFM MLI, the critical diameter is ~0.7 μm for debris and ~0.6 μm for micrometeoroids, as shown by the red line in Figure 78. From this estimation we derive that even the smallest particles listed in Table 26 can pass through the WFM MLI.

Assuming to estimate the diameter of the punctures on the MLI the formula in Sec. 12.2.3 (from [RD-38]), the total area left open by the punctures is 6.1×10^{-6} cm^2/camera/yr (see Table 26). **It is worth remarking here that the light tightness of the SDDs in the WFM is guaranteed by the beryllium layer above the detection plane, which has a much higher resistance than the MLI to the impacts from MMODs.**

Table 26: Expected rate of impacts of MMODs on the WFM MLI. The differential flux of MMODs is computed from the integral flux in

Table 24. We assume for each camera a geometric surface of 26 cm × 26 cm and an acceptance angle of 2π sr. The puncture surface is calculated assuming the formula in [RD-38]

Diameter [μm]	Differential flux [particle/m^2/yr]	Total rate on the WFM MLI [impacts/yr/camera]	Total puncture surface on MLI [cm^2/camera/yr]
1.5	1.1×10^3	71.7	1.5×10^{-5}

3	4.2×10^{2}	28.7	1.0×10^{-5}
5.5	2.1×10^{2}	14.4	9.5×10^{-6}
8.5	1.2×10^{2}	7.8	9.1×10^{-6}
15	1.6×10^{2}	10.5	2.9×10^{-5}
30	86	5.8	5.2×10^{-5}
55	31	2.1	5.6×10^{-5}
85	11.7	0.8	5.0×10^{-5}
150	8.2	0.6	1.0×10^{-4}
300	1.07	7.2×10^{-2}	5.2×10^{-5}
550	2.6×10^{-2}	1.8×10^{-3}	4.3×10^{-5}
850	2.9×10^{-3}	2.0×10^{-4}	1.1×10^{-6}
1500	8.2×10^{-4}	5.6×10^{-5}	9.9×10^{-7}

12.3.3 Expected rate of MMODs on the WFM SDDs without shielding

While the narrow FoV of the LAD collimator efficiently protects the SDDs from the impact of MMODs, a higher number of impacts is expected in the detection plane of the WFM due to the large FoV. In Table 27 and Figure 77, we show the expected rate of impacts on the WFM SDDs. For this calculation we assume per each camera a FoV of 2.5 sr, a mask surface of 26 cm × 26 cm with an open fraction of 25 % and four SDDs in the detection plane. Since we show in Sec. 12.3.2 above that even the smallest particles in Table 27 can pass through the MLI, in this estimation we do not take into account any shielding for the WFM apart the mask open fraction of 25 %.

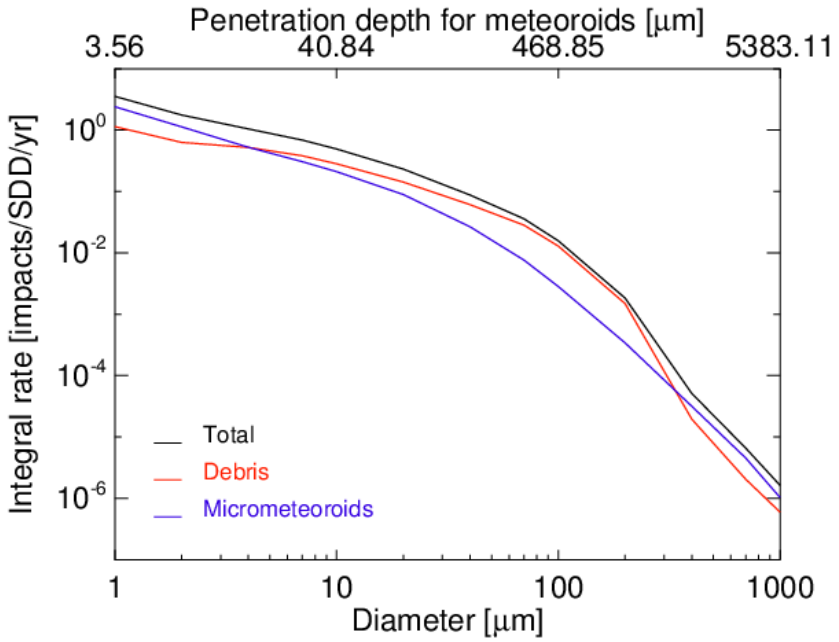

Figure 77: Expected integral rate of debris (red) and micrometeoroids (blue) on the WFM SDDs without shielding (from [RD-33]). The black line is the sum of the two components. As a worst case, the penetration depth is estimated for micrometeoroids, assuming a density of 2.5 g/cm^3 and a velocity of 20 km/s as specified in [RD-33].

Table 27: Expected rate of MMODs on the WFM SDDs **without shielding**. The total integral flux and total rate are the sum of debris and micrometeoroids. The penetration depth is estimated with the the Cour-Palais formula for brittle materials [RD-36] assuming the **worst case** of micrometeoroids, with a density of 2.5 g/cm^3 and a velocity of 20 km/s.

Diameter [μm]	Total integral flux [particle/m^2/yr]	Total rate [impacts/SDD/yr]	Penetration depth of micrometeoroids [μm]
1	2108	3.5	3.6
2	1047	1.8	7.4
4	622	1.0	15.4
7	409	0.7	28.0
10	293	0.5	40.8
20	138	0.2	85.1
40	52	8.7×10^{-2}	177.5
70	21	3.5×10^{-2}	321.2
100	9.3	1.6×10^{-2}	468.8
200	1.1	1.8×10^{-3}	977.5
400	3.0×10^{-2}	5.1×10^{-5}	2038.1
700	3.9×10^{-3}	6.6×10^{-6}	3688.4
1000	9.7×10^{-4}	1.6×10^{-6}	5383.1

12.3.4 The combined shielding for the WFM: Kapton and beryllium

As shown in Table 27, each SDD of the WFM is expected to receive few impacts per year from debris and micrometeoroids. Since most of these impacts will produce craters with a depth higher than the thickness of the passive layers on top of the SDD, and thus able to reach the silicon bulk, we studied a shielding system for the WFM.
The MLI above the coded mask is composed of 7.6 μm of Kapton ([RD-2]). We calculated the critical diameter, i. e. the minimum diameter of particles that can pass through the layer, using the Eq. (22) for a single layer of material [RD-37] assuming a normal incidence. As indicated in [RD-33], we assume for the debris a density of 2.8 g/cm^3 and a velocity of 13 km/s **with normal incidence as a worst case**, and for the micrometeoroids a density of 2.5 g/cm^3 and a velocity of 20 km/s.
As shown in Figure 78, the MLI can just stop debris of diameter < ~0.7 μm, with an expected rate of 1.5 impacts/SDD/yr, and micrometeoroids with diameter < ~0.6 μm, with an expected rate of 4.4 impacts/SDD/yr. In case only the MLI is used to shield the SDDs of the WFM, the total expected rate of impacts is thus 5.9 impacts/SDD/yr. In this analysis we do not take into account the fragmentation of the particles crossing the MLI.
In order to reduce the expected number of impacts of MMODs on the WFM SDDs, we included an additional beryllium shielding layer, of 25 μm thickness. As shown in Figure 78, the protection offered by a single layer of 25 μm of beryllium is equivalent to a single layer of ~190 μm of Kapton. But 190 μm of Kapton are almost opaque to X-rays at 2 keV, while 25 μm of beryllium have a transparency of ~70 % at the same energy.

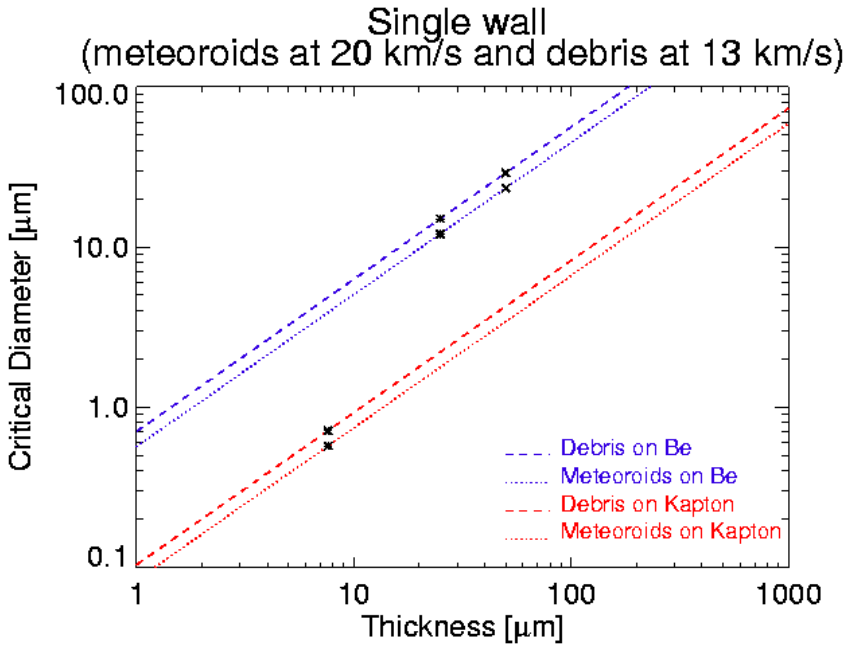

Figure 78: Minimum diameter of particles able to pass through a single layer of Kapton (red) or beryllium (blue).

The combination of a more resistant layer (the rear wall) at a certain distance from a thinner one (the bumper) significantly improves the shielding capability if compared to the two layers singularly assumed, and produces the so-called Whipple Wall [RD-38]. For the LOFT WFM, the bumper is represented by the MLI and the rear wall by the beryllium layer. The critical diameter for the Whipple Wall composed of the MLI (7.6 μm of Kapton) and the beryllium layer (assumed with 25 μm thickness), is shown in Figure 79 for two values of the distance between the two layers: 0.5 mm in case the beryllium is directly below the coded mask and 19.5 cm in case it is above the detection plane. More details on the formula used to estimate the critical diameter of a Whipple Wall are given in Sec. 12.2.2.2 and [RD-38].
If the distance between MLI and beryllium is 0.5 mm, the critical diameter is ~26 μm for debris (with an expected rate of 0.1 impacts/SDD/yr) and ~20 μm for micrometeoroids (with an expected rate of 0.09 impacts/SDD/yr). For a distance of 19.5 cm, the critical diameter increases up to ~191 μm for debris (with an expected rate of 1.7×10^{-3} impacts/SDD/yr) and ~149 μm for micrometeoroids (with an expected rate of 8.4×10^{-4} impacts/SDD/yr). In this analysis we do not take into account the fragmentation of the particles crossing the Whipple Wall.

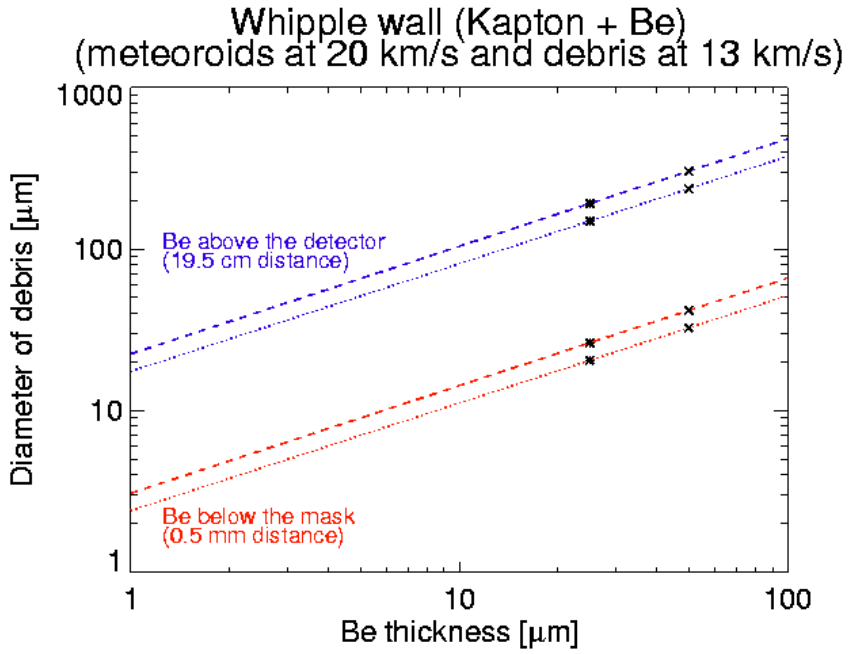

Figure 79: Minimum diameter of particles able to pass through a given thickness of a combined shielding (MLI and beryllium) placed above the detection plane (blue line, at 19.5 cm distance) or below the coded mask (red line, at 0.5 mm distance).

12.3.5 Expected rate on the WFM with shielding

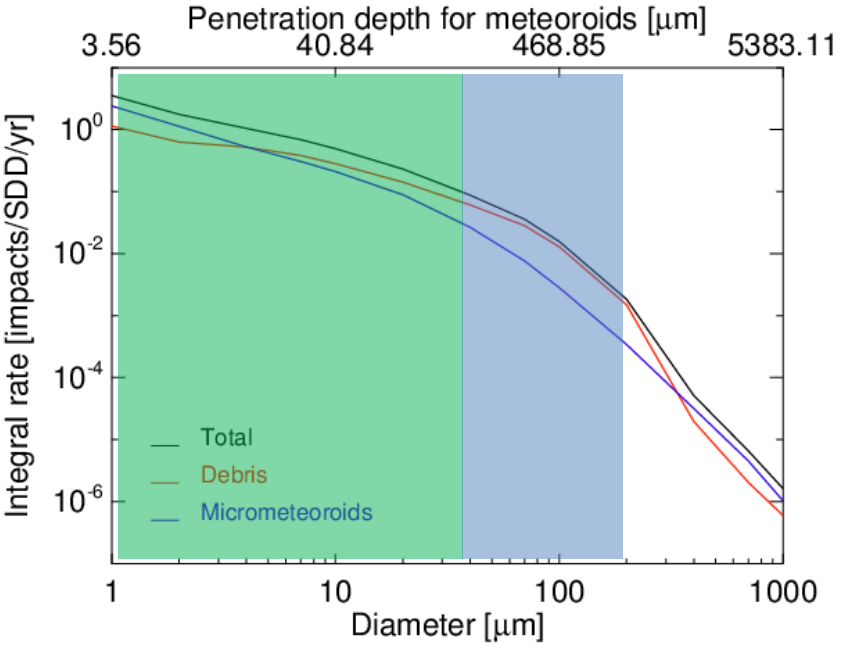

Figure 80: Expected integral rate of debris (red solid line) and micrometeoroids (blue solid line) on the WFM SDDs with the combined shielding. The black solid line indicates the total integral flux (debris and micrometeoroids). As a worst case, the penetration depth is estimated for micrometeoroids, assuming a density of 2.5 g/cm^3 and a velocity of 20 km/s as specified in [RD-33]. The region in green indicates the parameters of the particles that are stopped if the beryllium layer is above the detection plane or below the coded mask. The region in blue indicates the parameters

of the particles that are stopped only if the beryllium layer is above the detection plane but are able to pass through if the beryllium is below the coded mask.

The expected integral rate of MMODs on the WFM SDDs assuming the Whipple Wall composed of the MLI and a beryllium layer of 25 μm thickness is listed in Table 28 and shown in Figure 80. In the table, rows in green indicate the parameters of the particles that are stopped if the beryllium layer is above the detection plane or below the coded mask. Rows in blue indicate the parameters of the particles that are stopped if the beryllium layer is above the detection plane but that are able to pass through if the beryllium is below the coded mask. Rows in red indicate the parameters of the particles that pass through the Whipple Wall in both cases (beryllium below the coded mask and above the detection plane). In this analysis we do not take into account the fragmentation of the particles crossing the shielding layers.

Table 28: Expected rate of MMODs on the WFM SDDs with the Whipple Wall composed of Kapton and beryllium (25 μm thickness). The total integral flux and total rate are the sum of debris and micrometeoroids. The penetration depth is estimated with the the Cour-Palais formula for brittle materials [RD-36] assuming the **worst case** of micrometeoroids, with a density of 2.5 g/cm^3 and a velocity of 20 km/s. Rows in green indicate the parameters of the particles that are stopped if the beryllium layer is above the detection plane or below the coded mask. Rows in blue indicate the parameters of the particles that are stopped only if the beryllium layer is above the detection plane but are able to pass through if the beryllium is below the coded mask. Rows in red indicate the parameters of the particles that pass through the Whipple Wall in both cases (beryllium below the coded mask and above the detection plane). In this analysis we do not take into account the fragmentation of the particles crossing the shielding.

Diameter [μm]	Total integral flux [particle/m^2/yr]	Total rate [impacts/SDD/yr]	Penetration depth of micrometeoroids [μm]
1	2108	3.5	3.6
2	1047	1.8	7.4
4	622	1.0	15.4
7	409	0.7	28.0
10	293	0.5	40.8
20	138	0.2	85.1
40	52	8.7×10^{-2}	177.5
70	21	3.5×10^{-2}	321.2
100	9.3	1.6×10^{-2}	468.8
200	1.1	1.8×10^{-3}	977.5
400	3.0×10^{-2}	5.1×10^{-5}	2038.1
700	3.9×10^{-3}	6.6×10^{-6}	3688.4
1000	9.7×10^{-4}	1.6×10^{-6}	5383.1

12.4 Measurement of the effects of impacts from debris

In order to study the increase of leakage current of a SDD after the impact of a hypervelocity particle, we performed two campaigns at the Cosmic Dust Acceleration Facility of the the Max-Planck Institute fuer Kenrphysik (MPIK) in Heidelberg (Germany). During the first campaign (on July 2012) we "bombarded" a SDD with

particles of Olivine (a magnesium iron silicate with a density of 3.3 g/cm^3) and various combinations of size and velocity. Because of the limited sensitivity of the instrumentation that we employed to measure the leakage current of the SDD, we did not obtain conclusive results (see [RD-40]).
On May 2013 we performed a second campaign at the same facility using iron particles (7.9 g/cm^3) and a much more sensitive instrumentation to measure the leakage current. In this section we only report about the second measurement campaign.

12.4.1 Aim of the test

The campaign was performed in order to study the effects produced by the impact of hypervelocity particles on the LOFT detectors. During the campaign we measured the increase of the leakage current by "bombarding" with hypervelocity iron particles two different types of detectors: 4 sets of diodes and a SDD of the FBK-3 production. All the detectors have been produced with the same technology, but they differ in the passivation layer (the metallization of the diodes is almost completely open while the SDD drift region is completely passivated) and in the bulk material (the diodes are Floating Zone Silicon while the SDD is NTD Silicon). Note that only the variation on the thickness of the passivation may have an effect on the damage created by the impacts of dust particles since the device bulks have differing protection "shield" (300 nm thinner in the case of the diodes). For the detectors under test the thickness of the passive materials above the bulk is ~1.0 μm for the SDD and ~0.7 μm for the diodes. In the SDD under test the thickness of the passive layers is ~0.2 μm smaller than usual.
We started the tests by shooting particles of different size and velocity on the diodes. Being simple structures, the diodes are the most useful devices when one wants to understand the results of an experiment. With this test we built a reference frame to analyse the leakage current increase in the SDD. Then the test was repeated on the SDD itself aiming at both the determination of the threshold value of the particle parameters (size and velocity) to give a measurable damage on the detector and the assessment of the damage effects produced on the SDD by the most energetic particles available at the accelerator.

12.4.2 Experimental set-up

The Cosmic Dust Acceleration Facility of MPIK is a modified Van de Graaff generator, able to reach a potential of 2 MV, and can be operated in single-shot or in continuous mode. A dedicated detector in the beam line is used to measure the size and velocity of the particles hitting the device under test. We selected the single shot mode during the campaign, in order to associate the effect of the damage created by an impact, the variation of the leakage current of the test device, with the parameters of the specific particle shot. To measure the leakage current we use two Keithley 2657 Source Measure Units (SMUs), controlled by a computer via an Ethernet connection.
Two experimental chambers are available at the facility to test devices of very different sizes: a small chamber capable of hosting devices of few cm^2, and a large one where ~0.25 m^2 are available to mount bigger systems.
The first chamber was used to shot particles at diode setups (see e. g. Figure 81). These are an array of four 4 mm^2 diodes, each one surrounded by a guard ring that defines sharply the diode volume. The diodes where biased at 20 V by means of a laboratory power supply unit (condition equivalent to the bias of the SDD cathodes with respect to the bulk). The four diodes in a set in Figure 81 are connected together and the leakage current is measured using one SMU. The other SMU is used to

measure the current of the guard rings, connected together. During the test, the leakage current of the diodes sets ranges between few pA to hundreds of pA. The SMU can measure currents in this range with a resolution of 1 fA.
An AD590 thermometer was mounted close to the diodes to monitor possible temperature variations, which we verified to be negligible within the time frame of each test.

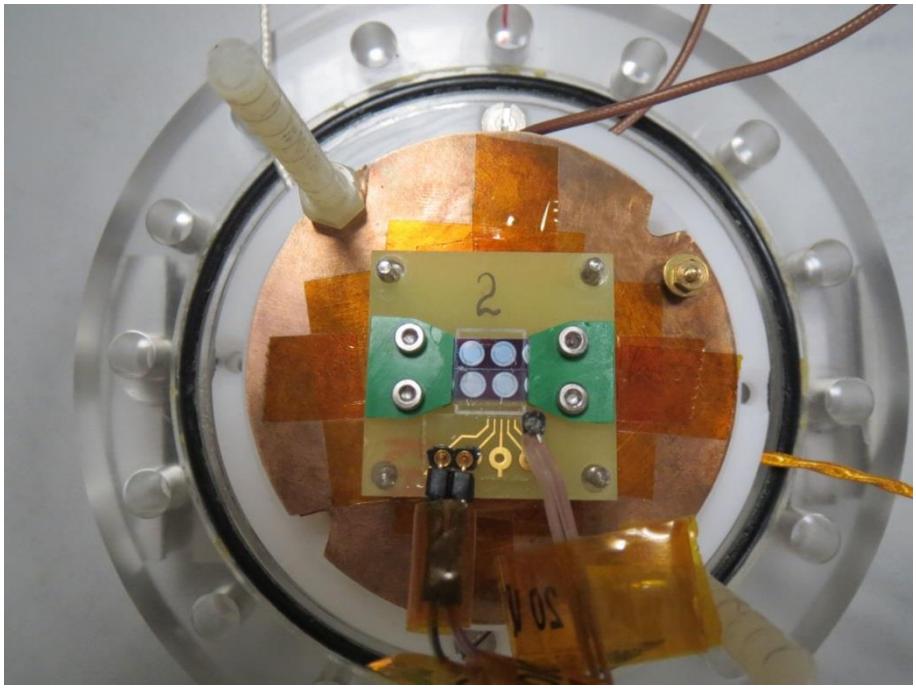

Figure 81: Picture of a set of diodes mounted on the flange of the small experimental chamber at the Cosmic Dust Accelerator Facility.

The large experimental chamber was used to shot particles to the SDD (see Figure 82). The mechanical system inside the chamber allows to move the detector along the horizontal and vertical axis, and to tilt it with respect to the direction of the incident particles.
During the "irradiation", the SDD was biased at the nominal voltage of -1300 V using a high voltage power supply (HVPSU). All the anodes in each detector half, LAD or WFM, are bonded together and the leakage current is provided in output. In this way we minimize the number of instruments required for the test while being still able to shot particles at the whole detector surface. A SMU is connected to the anodes of the LAD half, the other one to the WFM half. The currents of the two halves are simultaneously and independently measured.
The current monitor output of the HVPSU was used to measure the integrated voltage divider current, and an AD590 sensor monitored the temperature of the SDD, as shown in Figure 89. While the leakage current of the LAD half was small, a known hot-spot on the WFM half produced a large leakage that did not allow a sufficient sensitivity to measure the effects of the particle impacts on the detector. For this reason in the test we concentrated only on the LAD half of the SDD.

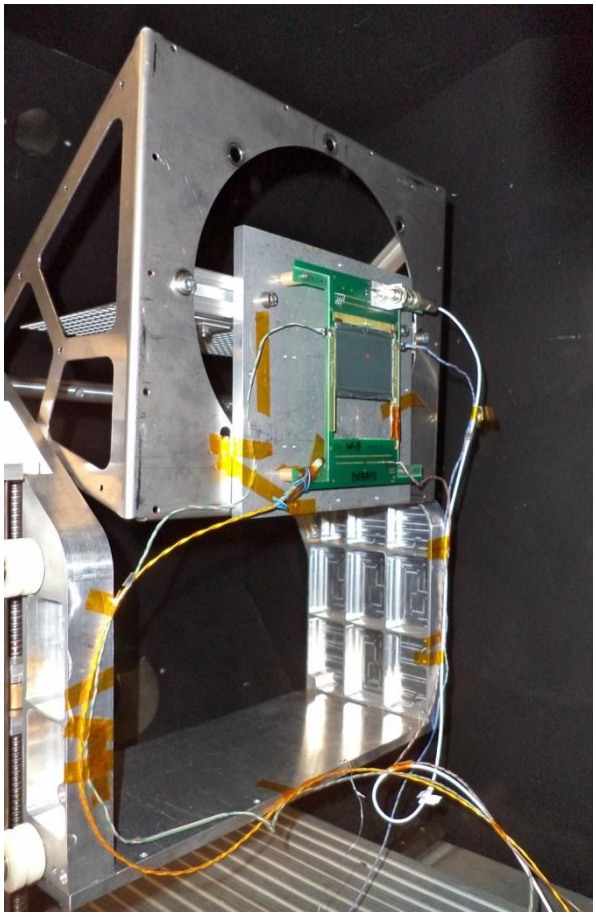

Figure 82: Picture of the SDD inside the large experimental chamber of the Cosmic Dust Accelerator Facility. The red dot on the SDD indicates the center of the spot (~1 cm^2 surface) where the particles are "shot".

Figure 83 shows the distributions of the size and velocity of the particles shot at the diode setups (top panel a), and at the SDD (bottom panel b). We "bombarded" each diode array with particles with a narrow range of size and velocity values. With this method on each diode array we produced craters with a narrow distribution of the depth (see the top-left panel (a) in Figure 85). We selected particles with similar combination of size and velocity when "bombarding" the SDD, as shown in the bottom panel of Figure 83, thus producing craters with a narrow distribution of the depth (see also the top-left panel (a) of Figure 87).

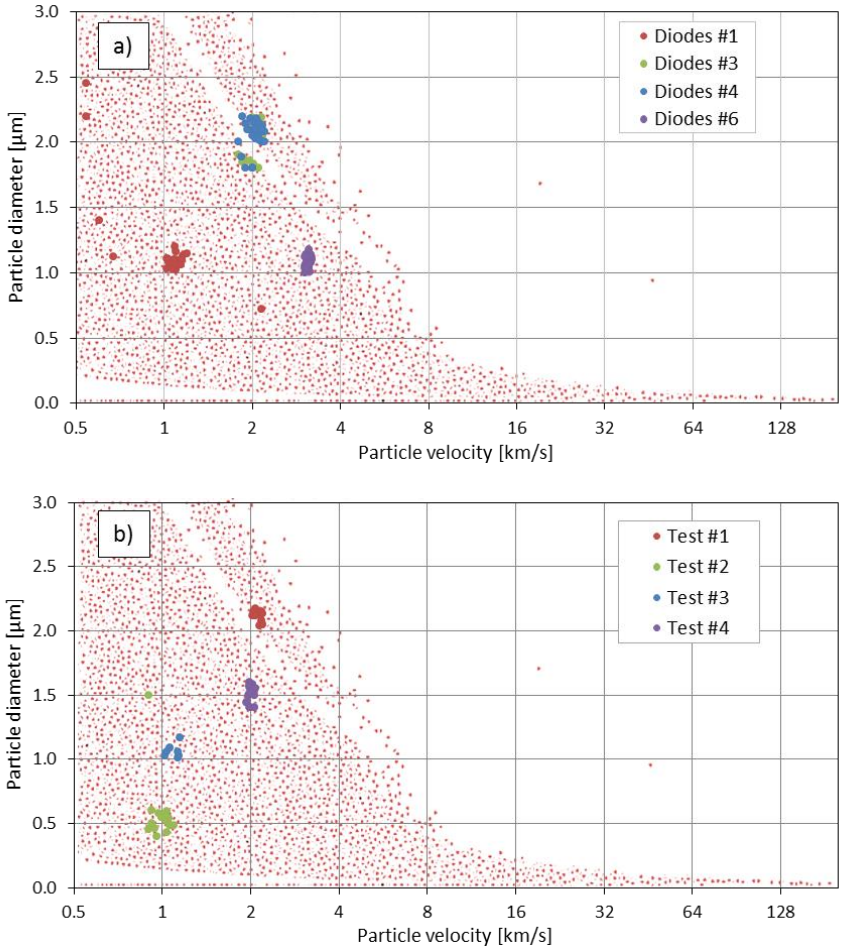

Figure 83: Distribution of the parameters (diameter and velocity) of the particles shot to the diodes (a) and to the SDD (b) superimposed to the distribution of the parameters available at the facility with iron particles.

It is important to note that, due to the layout of the diodes, only a fraction of the particles shot at the test structure effectively hit the diodes. The remaining impacts were located on the guard rings or on the not sensitive space outside the guard rings themselves (see e. g. Figure 81). Since the depleted volume of the guard rings is not well defined, it is not possible to guarantee that the total effect of the impacts on this region can be seen in the measurements of its leakage current. For this reason, although we measured the current of the guard rings, we have not used this information for the analysis of the test results.
On the contrary, since the beam spot on the SDD has a typical surface of ~1 cm^2 and was placed well inside the sensitive area of the detector, the complete effect of every particle shot to the SDD is present in the measurement of the leakage current.
Figure 84 shows images at the optical microscope of the craters created by the impact of the most energetic particles shot at the diodes (left panel) and the SDD (right panel), whose estimated penetration depth was ~3 µm. As shown in the figure, the typical size of these craters is ~10 µm.

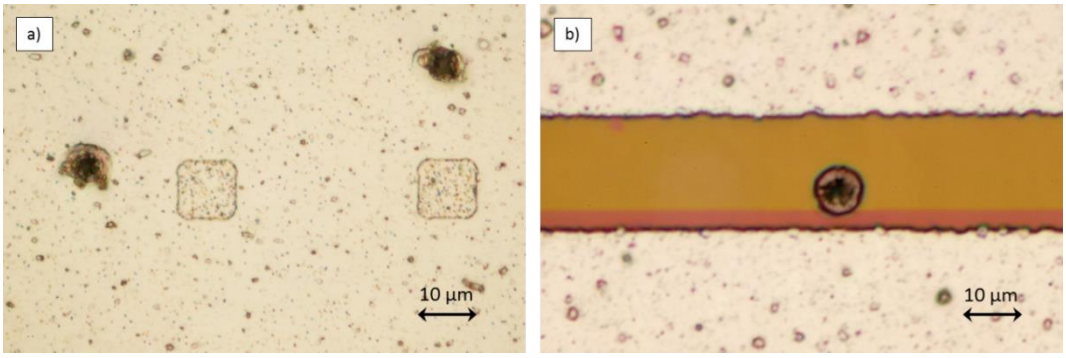

Figure 84: Optical microscope images of the craters produced by the highest penetrating particles shot to the diodes (a) and to the SDD (b).

12.4.3 Results

12.4.3.1 Test on the arrays of diodes

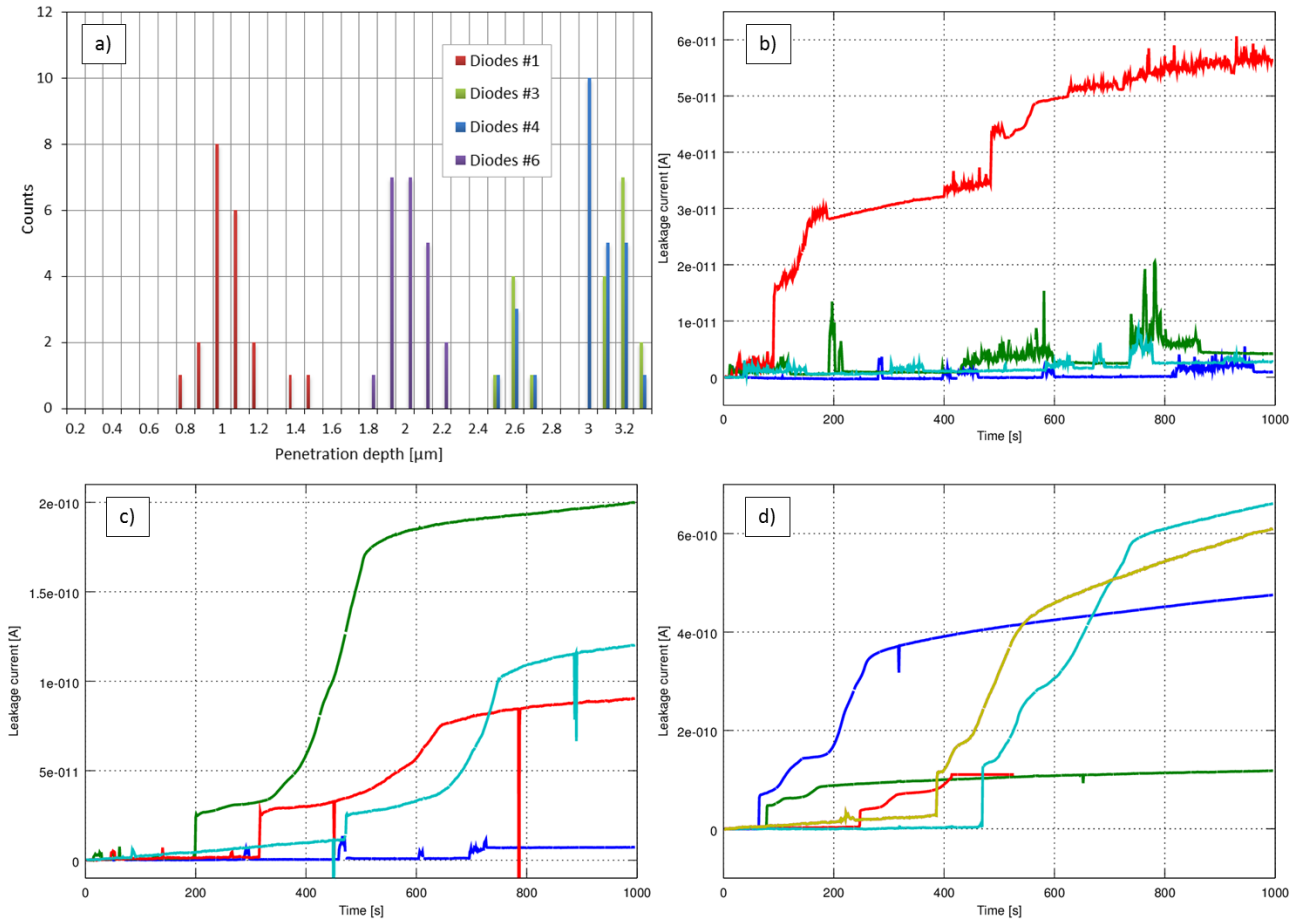

Figure 85: Summary of the measurements taken with the diodes setups during the test. Panel a) reports the distribution of the particles penetration depth calculated with the Cour-Palais formula for the parameters of all the particles shot to the diodes, as monitored by the accelerator instrumentation. Panels b), c) and d) show some current leakage plots for setup #1, #6 and #4 respectively.

Figure 85 shows a summary of the measurements taken with the diode setups when shooting particles with estimated penetration depths ranging between ~0.8 and ~3.3 μm, whose distribution is reported on panel a).
Panels b), c) and d) of Figure 85 show how the leakage current increased for some of the diode hits measured during the tests. In panel b) it is also possible to see, as a variation with high frequency but limited amplitude, the spurious effect of X-ray photons generated by the accelerator that were not damped during the test and detected by the diodes. From these plots it is evident that the damage created on the silicon devices is a very complex mechanism that evolves in a time frame ranging from several tens of seconds to even several hours (as will be shown later). Because of the limited statistics of the measurements, due to the large amount of time required to let the leakage current stabilize, a rigorous analysis of the results is not possible, but some general remarks can be put forward:

1. At the impact time, when the crater forms, a sharp increase of the leakage current occurs, as shown by the sudden "steps" in panels b) c) and d) of Figure 85. For all the investigated particle parameters the step on the leakage current is in the range between few pA to few tens of pA.
2. Considering the leakage current, in accordance with the thickness of the diode protective layers, particles parameters that give an estimated penetration depth of ~1 μm seem to be around the threshold of sizable damage creation. This fact tends to confirm the validity of the Cour-Palais formula, but a look at Figure 85 shows that probably the accuracy of the formula is within a factor of 2.
3. The impact energy is not instantaneously dissipated, but some of it is accumulated as stress of the crystal. This stress is relaxed during a long time period by means of fault propagation on the crystal, which produces further leakage current increase ranging from few pA up to 1 – 2 nA.
4. The volume affected by the damage caused by the impact is a location of high electric fields due to the discontinuities of the lattice. The leakage current increase is then due to impact ionization generated by the charge carriers (electrons and holes) traversing this high field region. This fact can be verified by a measurement of the variation with temperature and bias voltage of the leakage current resulting from the impact of debris during the campaign. Figure 86 clearly shows that, after the test, the generation rate is higher than the thermal leakage generation before the test ("no damage", blue curve) due to impact multiplication, which decreases as the temperature increases because the carriers accelerated by the high electric field have a higher probability of losing energy to the crystal by means of scattering with phonons. Also, the higher is the bias, and the higher is the multiplication factor. This is coherent with the discussion of the variation of the multiplication factor as a function of the bias voltage and temperature reported e. g. in [RD-41].

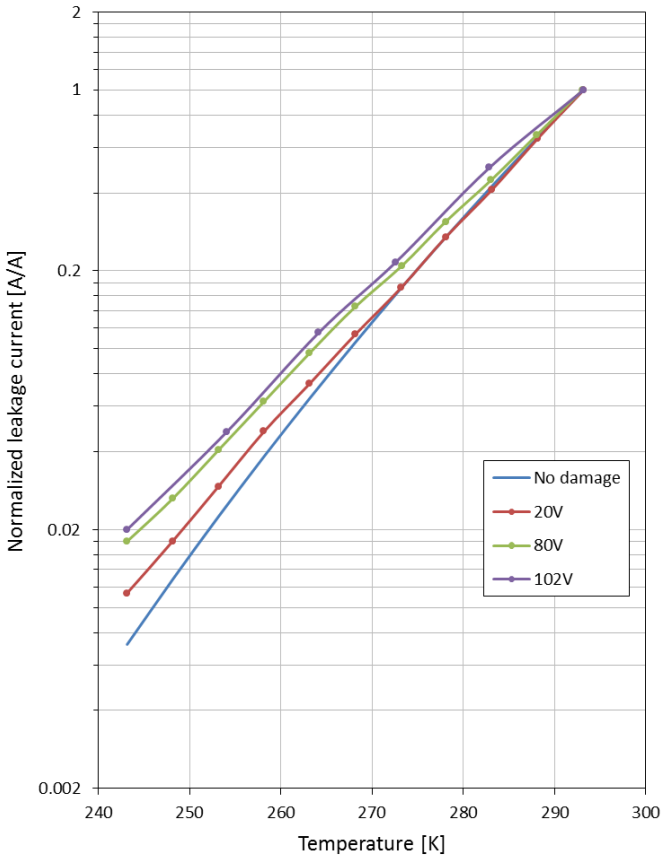

Figure 86: Temperature dependence of the leakage current of the Diodes #4 setup for different bias conditions after the test. The comparison with the "no damage" curve (before the test) shows that the leakage current increase is due to impact ionization in the high-field regions close to the damage sites.

12.4.3.2 Test on the SDD

The impact test was repeated on the SDD with an extended range of penetration depths, from ~0.4 μm to ~3 μm. A summary of the results is presented in Figure 87.
In the case of the SDD the threshold on the penetration depth to produce a measurable increase of the leakage current is between ~1 μm and ~1.3 μm. Here the variety of leakage current "shapes" is even broader, including cases where after a very large step the leakage current decreases to a smaller value and cases where the stress relaxation seems to proceed by discrete events clearly separated in time. It is interesting to note that the largest increases of the leakage current were generated by particles with medium depth penetration (~2 μm): this is probably due to the location of the impact, since along the drift direction there are places where the electric fields are intrinsically higher than the average value (e.g. at the junction of the cathodes). Nevertheless, the results are in very good agreement with those of the diodes.
Figure 88 shows the evolution of the SDD leakage current during the whole test session that lasted ~25 hours, until the stabilization of the leakage current is reached. It is evident that the leakage current was consistently increasing due to the various damages created by the particle impacts even after shooting the last particle around 5 hours from the beginning of the test.

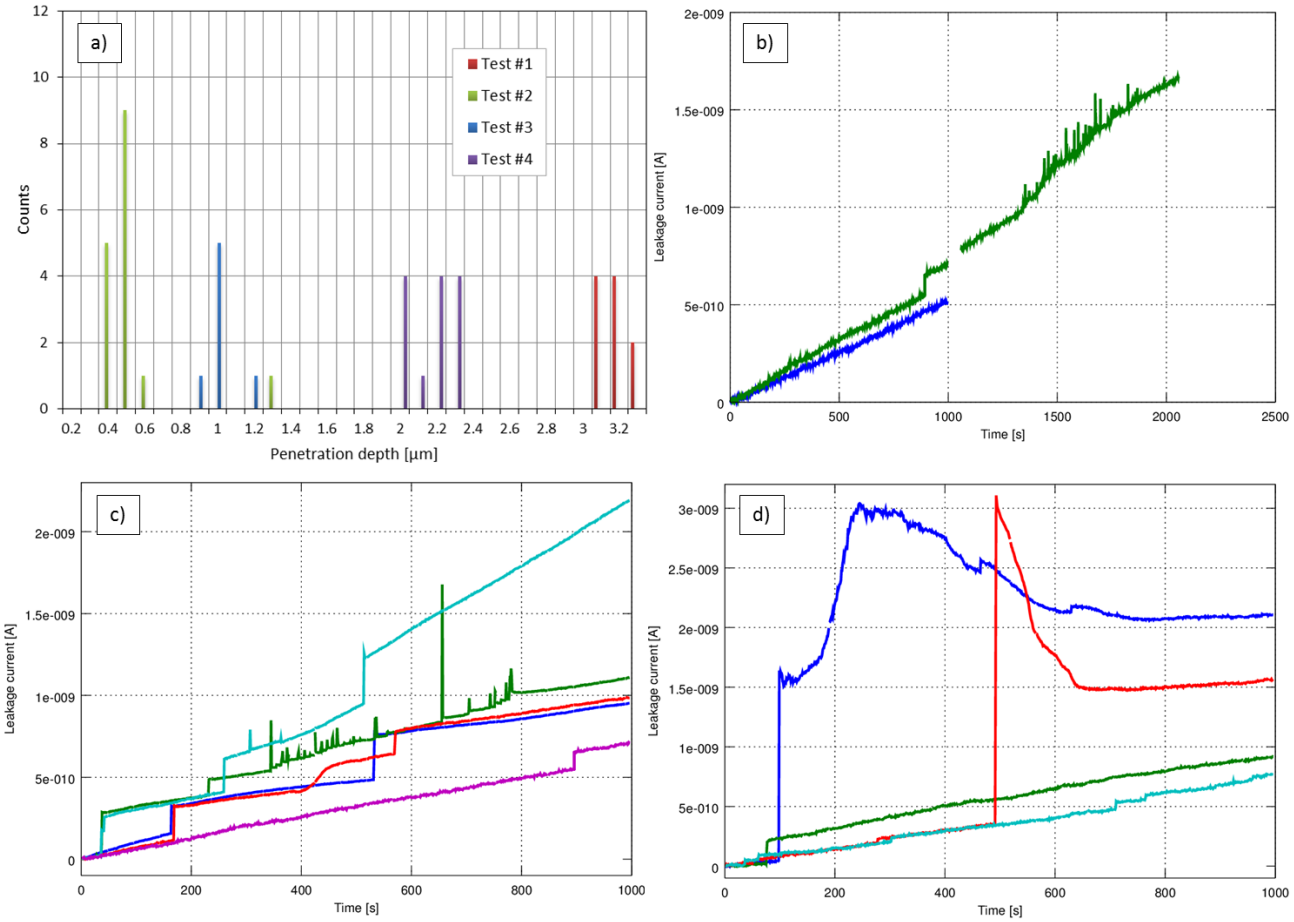

Figure 87: Summary of the measurements taken with the SDD during the test. Panel a) reports the distribution of the particles penetration depth calculated with the Cour-Palais formula. Panel b) shows the shapes of the total leakage current variations during Test #2 (green) and Test #3 (blue). Panel c) and d) show all the leakage current plots respectively for Test #1 and Test #4.

After 46 impacts of particles with different combination of size and velocity, of which 24 were above the sizable damage threshold, the total increase of leakage current was ~43 nA. The temperature at the end of the measurement is higher than at the beginning (see Figure 89). By correcting for the variation of temperature, we obtain an increase of ~31 nA, equivalent on average to ~1.3 nA/impact at 30 °C.
During the test the current of the integrated voltage divider remained constant within the sensitivity of the measurement, but of course an increase of the same amount of the leakage current was produced by the holes generated by the impact ionization phenomenon: this increase is three orders of magnitude lower than the integrated voltage divider current.

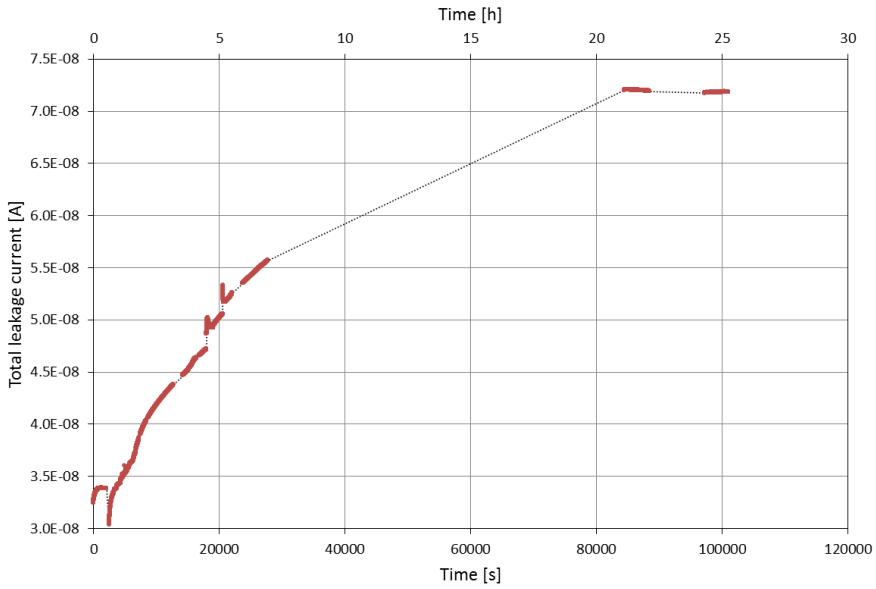

Figure 88: Plot of the LAD total leakage current during the whole test session, showing that the stabilization is reached several hours after the end of particle "shooting". The total measured increase of leakage current is ~43 nA after 46 impacts (of which 24 have a penetration depth above the threshold of ~1 μm).

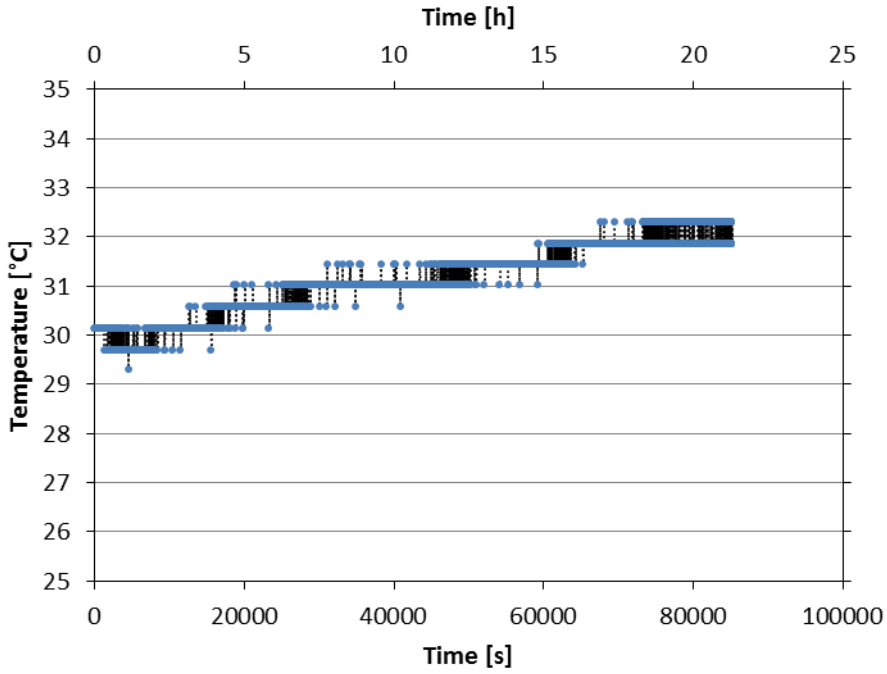

Figure 89: Measurement of the SDD temperature during the test session.

12.4.4 Implications for the LOFT SDDs in orbit

The expected rate of MMODs able to reach the SDDs of the LAD (see Table 25) and WFM (see Table 28) is extremely small, due to the micro-capillary plate collimator for the LAD and the Kapton-beryllium Whipple Wall shielding for the WFM. In addition, the most probable impacts are those with particles that have a penetration depth of the order of 3 – 4 μm. **The particle parameters used for the tests at the Cosmic Dust Acceleration Facility are clearly a good match to the LOFT expected environment in orbit**.

The tests demonstrated that the average leakage current increase due to an impact of these MMODs on a SDD has a value of ~1.3 nA/impact at ~30 °C, and that the leakage current still scales exponentially with the absolute temperature, even though with a lower degree. Such impacts produce a crater with diameter of the order of 10 μm (see Figure 84). As a consequence, impacts on the SDDs of LOFT in orbit will certainly cause the electronics channels connected to the anodes reading the volume involved by the impact (a maximum of 2 for the LAD and 9 for the WFM) to not comply anymore with the noise specifications, but the remaining sensitive surface of the detector and acquisition chain will not be affected.

The effect on the drift cathode bias potentials is completely negligible, more so at lower temperatures since the integrated voltage divider current will increase with a decrease of the detector operative temperature (the hole mobility has a temperature dependence of $T^{-2.2}$). Consequently any possible increase of the holes current produced by the impact of MMODs will be negligible if compared with the much higher current of the integrated voltage divider and will not affect the bias potentials of the drift cathodes.

The SDD can tolerate the damage produced by even larger MMODs without major problems. The most sensitive region from this point of view is the guard region, where the cathode implants are narrower and the electric field is higher. However, such regions are shielded by the collimator in the LAD and by the beryllium shield in the WFM.

13 SUMMARY AND CONCLUSIONS

13.1 Requirements for the LAD and WFM

The scientific requirements on the energy resolution of the LAD and on the reconstruction of the photon position of the WFM are translated into corresponding requirements on the electronic noise of the SDDs, in the form of σ_{ENC}: for the LAD σ_{ENC} < 17.0 e- RMS and for the WFM σ_{ENC} < 13.0 e- RMS. The required operating temperature as a function of the orbit was derived.

13.2 Models for the LOFT particle environment and applied margins

- The orbits planned for LOFT are equatorial LEO with an altitude between 550 km and 600 km and an inclination < 5°. Both the industrial studies selected as a baseline an orbit with 550 km altitude and 0° inclination.
- The radiation environment relevant for the LOFT SDDs is composed of trapped protons (concentrated in the South Atlantic Anomaly) and soft protons (see [RD-14]). All the other components (i. e. cosmic rays, protons and ions from Solar flares) can be neglected thanks to the equatorial LEO.
- In order to select the model to describe the trapped protons for LOFT, we compare the predictions of AP8MIN (in minimum solar conditions) and AP9 with in-orbit data of the BeppoSAX Particle Monitor (PM), with a threshold of ~20 MeV for protons. The data are collected at an inclination of ~3.9° and an altitude between 596 km and 547 km, representative of the orbits for LOFT. In our analysis we compare the maps of the SAA (counting rate and extensions) and the duration of the passages through the SAA from the PM data with the predictions of AP8MIN and AP9 at the same altitude and inclination. We find that the SAA from AP9 is severely overestimated with respect to the PM data, while the one in AP8MIN is slightly underestimated.
- In literature (see [RD-16] and [RD-17]) an accuracy within a factor of ~3 is found for AP8 from the comparison with the Space Shuttle data, although at an inclination of 28.5°, higher than LOFT.
- An independent verification of AP8MIN and AP9 against the data of the Proba-1 satellite by an ESA team [RD-12] finds that AP8MIN reliably describe the environment by applying a 3x factor on the fluence.

As conclusion, a 5x AP8MIN fluence was adopted to model the trapped protons. The instrument design was done assuming an additional 4x margin on the proton fluence. The LAD and WFM design margin is therefore 3.3x larger than required by ESA in [RD-12].

13.3 Radiation damage on the LAD and WFM

- The leakage current of the SDDs of LOFT in orbit increases because of the displacement damage produced by charged and neutral particles.
- The increase of leakage current from the proton fluence is computed using the formulas in [RD-6] and adopting the NIEL scaling hypothesis: the displacement damage is linearly proportional to the incident fluence and to a hardness factor, depending on the type and energy of the incident particles.
- For trapped protons, the equivalent fluence at an energy of 10 MeV is estimated at the various orbits using the SPENVIS tool, considering the shielding materials of the LAD and WFM. The hardness factor for protons of 10 MeV energy on

detectors of 450 μm thickness is calculated in [RD-6]. For soft protons, we derive the fluence from [RD-14] and we calculate the effective hardness factor for the shielding and geometry of the LAD and WFM.

- Similarly to the displacement damage, the TID is estimated for trapped protons using SPENVIS and is calculated for soft protons considering the shielding and geometry of the LAD and WFM.

13.4 Experimental measurement of the NIEL from protons

- In order to verify the predictions of [RD-6] for the displacement damage of the SDDs with the NIEL scaling hypothesis, we irradiated various models of detectors. At the PIF of the PSI accelerator we irradiated at energies consistent with trapped protons three SDDs of different productions: ALICE, FBK-2 and FBK-3. At the Rosenau accelerator of the University of Tuebingen we irradiated with soft protons an FBK-2 and an FBK-3 SDD.
- The anode leakage current of all the SDDs has been measured before the irradiation at the probe station of INFN Trieste.
- The anode leakage current of the ALICE SDD has been measured with the probe station ~66 days after the irradiation. The value at the end of the irradiation has been extrapolated from the time dependence of the total anodic current determined from I-V measurements. This method has a limited sensitivity and averages the contribution of all the anodes. With this method the agreement between the measured increase of leakage current and the predicted value is within 37 %.
- The leakage current of the FBK-2 SDD has been measured after the irradiation with an indirect method during the measurement of the CCE. In this case we obtain an agreement within the experimental uncertainty (~10 %) with the expectations.
- The anode leakage current of the FBK-3 SDD has been measured after the irradiation with the probe station and the agreement with the prediction is within 12 %. For this SDD we also measured the annealing of the displacement damage and we found that the trend in time is consistent with the literature [RD-19].
- During the irradiation, the FBK-3 SDD also received a TID representative of the expected value for LOFT in orbit (including the margin of factor of 20). Since the measured increment of the leakage current can be explained with the displacement damage (within 12 %), this means that the increment for this dose level is negligible.
- We performed two irradiation campaigns with soft protons on the SDDs in order to measure the displacement damage and TID produced by this component. We found that the displacement damage produce a smaller damage than expected, with an increase in leakage current ranging between 25 % and 33 % of the predicted value. We also found that the increase of the leakage current of a diode produced by the TID is only ~ 60% larger than the pre-irradiation value, even after a TID equivalent to more than 10 times the expected dose for the WFM (considering the effective exposure from the LOFT mock up observing plan).

In conclusion, we verified that the displacement damage of the SDDs is adequately described by the formula in [RD-6] with the NIEL scaling hypothesis and the

annealing of the damage follows the model in [RD-19]. We also verified that the contribution of the TID to the leakage current is negligible.

13.5 Temperature reduction as a mitigation strategy for the NIEL

- We measured the leakage current of the FBK-2 SDD as a function of temperature after a proton irradiation and verified that it follows the same variation with temperature as the intrinsic leakage current. This confirms similar results from the literature.
- We therefore adopt the reduction of the operating temperature of the SDDs of the LAD and WFM as a mitigation strategy for the displacement damage (accounting for the 20x margin on the proton fluence provided by AP8MIN).

13.6 The expected variation of the CCE and the experimental verification

- Thanks to the very short collection time of the charge cloud, ~5 μs at the operative temperature, the expected variation of the CCE for LOFT in orbit is 0.004 % (including the 20x margin on the proton fluence).
- We irradiated with protons of 11.2 MeV a FBK SDD prototype to measure the variation of CCE: from the peak position of a 5.9 keV line we measured a variation of (0.65 ± 0.15) % after the irradiation, in agreement with a predicted value of 0.8 % for the adopted fluence.

13.7 Expected impacts of MMODs on the LAD and WFM

- In orbit data show that a representative sample of the LAD collimator did not reported any damage from MMODs after 756 days in orbit on the International Space Station. This is confirmed by the analytical estimation of the rate of potentially perforating (large-size) MMODs (0.3 over the mission lifetime over the whole LAD surface).
- The MMODs which pass through the open channels of the collimator, possibly reaching the SDDs of the LAD, have an expected rate of impacts of the order of 10^{-3} impacts/SDD/year, corresponding to about 10 impacts over the LAD lifetime. Experimental tests in a debris accelerator show that such impacts only result in an increased current on the impacted channel, which can be isolated without impacting on the operation of the rest of the Module and not even the same detector (that is, an expected loss EoL of 10 channels out of 4.5×10^5).
- The WFM has a wider field of view than the LAD and the thin MLI (7.6 μm of Kapton) can stop only a very small fraction of MMODs in orbit. The introduction of a 25 μm thick beryllium shield above the detection plane reduces the expected rate of impacts down to ~10^{-3} impacts/SDD/year. Further optimization studies will be carried out in Phase B1.

13.8 Experimental measurement of the effect of the impacts from MMODs

- At the Cosmic Dust Accelerator facility of the MPIK in we "bombarded" 4 sets of diodes and a SDD (of the FBK-3 production) using iron particles with various combinations of size and velocity. The thickness of the passive layers above the silicon bulk is ~0.9 μm for the diodes and ~1.2 μm for the SDD.
- We started by measuring the increase of leakage current after an impact on the diodes, then we repeated the measurement on the SDD. We found that the

particles with a penetration depth above a threshold of 1 – 1.3 μm produce an increase of the leakage current. This value is in good agreement with the thickness of the materials above the silicon bulk of the devices under test.

- The impact of a hypervelocity particle on the diodes or on the SDD produce a sudden jump of the leakage current, which may be followed by a slower increase. We monitored the leakage current of the SDD for ~20 hours after the end of the "irradiation" and we found that the leakage current reaches a stable value. At the stabilisation the measured increase of leakage current produced by 24 impacts is ~31 nA (corrected for the variation of temperature). This corresponds to an average increase of ~1.3 nA/impact at 30 °C.
- The most penetrating particles shot in the test produce craters with a typical diameter of ~10 μm. As a consequence, impacts on the SDDs of LOFT in orbit will certainly cause the electronics channels connected to the anodes reading the volume involved by the impact (a maximum of 2 for the LAD and 9 for the WFM) to exceed the noise specifications, but the remaining sensitive surface of the detector and acquisition chain will not be affected.